FALLING FILM EVAPORATION ON A SINGLE TUBE AND ON A TUBE BUNDLE

THÈSE N^{O} 2987 (2004)

PRÉSENTÉE À LA FACULTÉ SCIENCES ET TECHNIQUES DE L'INGÉNIEUR

Institut des sciences de l'énergie

SECTION DE GÉNIE MÉCANIQUE

ÉCOLE POLYTECHNIQUE FÉDÉRALE DE LAUSANNE

POUR L'OBTENTION DU GRADE DE DOCTEUR ÈS SCIENCES TECHNIQUES

PAR

Jean-François ROQUES

ingénieur mécanicien diplômé EPF
et de nationalité française

acceptée sur proposition du jury:

Prof. J. Thome, directeur de thèse
Prof. F. Avellan, rapporteur
Prof. A. Cavallini, rapporteur
Prof. O. Zürcher, rapporteur

Lausanne, EPFL
2004

Abstract

This study is a contribution for the improvement of horizontal falling film heat exchangers. This type of evaporator has the potential to be widely used in the petrochemical industry, for the sea water desalination, or in the large refrigeration systems.

An experimental test facility has been constructed in order to study the evaporation of the liquid refrigerant R-134a flowing on a vertical array of horizontal copper tubes with a length of 0.55 meter and a diameter of $19.1mm$. Special care has been taken to achieve uniform liquid distribution along the top tube. Four types of tubes were tested including a plain tube, two tubes with mechanically enhanced boiling surfaces (Turbo-BII HP and Gewa-B) and a porous coated tube (High-Flux). Tube arrays with three different tube pitches were tested. Measurements were performed at three different nominal heat flux levels over a wide range of liquid overfeed. For comparison, heat transfer coefficients in pool boiling conditions were measured.

The experimental parameters are the following: the liquid film Reynolds numbers from 0 to 3000, heat fluxes between 20 and $60kW/m^2$ and tube pitches from 22.3 and $25.5mm$. The heat transfer coefficients have been measured locally at the mid point of each of the ten tubes. The study shows that there are two types of fundamental behavior characterized by a particular film Reynolds number:

- Over a threshold value of this Reynolds number, the nucleate boiling in the film governs the heat transfer and this heat transfer coefficient is independent of the Reynolds number.
- Below this threshold value, the heat transfer coefficients drop drastically due to the formation of local dry patches.

The heat transfer coefficient during falling film evaporation was found to be approximately 1.3 times larger than the heat transfer coefficient during pool boiling and this multiplier was found to be dependant on the heat flux and tube spacing but not the flow mode.

Finally, the understanding of the physical phenomena governing the falling film evaporation of liquid refrigerants has been improved. Further-

more, a method for predicting the film Reynolds number at the onset of dry patch formation has been developed and a heat transfer correlation for boiling in falling films proposed. These represent significant improvements for the design of falling film evaporators.

Résumé

Cette étude est une contribution à l'amélioration des échangeurs de chaleur à film tombant. Ce type d'évaporateur peut potentiellement être largement employé dans l'industrie pétrochimique, pour la désalinisation de l'eau de mer ou dans les grands systèmes de climatisation.

Un stand d'essai expérimental a été réalisé afin d'étudier l'évaporation de R-134a liquide s'écoulant verticalement sur un alignement de 10 tubes horizontaux en cuivre d'une longueur de $0.55m$ et de diamètre $19.1mm$. Un soin particulier a été apporté à la maîtrise de l'uniformité de la distribution de liquide au niveau du tube supérieur. Les tubes testés sont: un tube lisse de référence, deux tubes à surface mécaniquement améliorée (Turbo-BII HP et Gewa-B) et un tube à revêtement poreux (High-Flux). Les mesures ont été realisées pour trois espacements entre les tubes, trois flux de chaleur nominaux et une large gamme de débit de réfrigérant s'écoulant sur les tubes. Les coefficients de transfert de chaleur en ébullition en vase ont été mesurés afin d'établir une référence.

Les paramètres expérimentaux sont le nombre de Reynolds du film liquide qui est compris entre 0 et 3000, la densité de flux de chaleur locale qui varie entre 20 et $60kW/m^2$ et la distance séparant les axes des tubes qui est comprise entre 22.3 et $25.5mm$. Les coefficients de transfert de chaleur ont été mesurés localement au milieu des tubes pour chacun des dix tubes. L'étude montre qu'il existe deux types de fonctionnements fondamentaux caractérisés par un nombre de Reynolds de film particulier:

- Au-dessus de ce nombre de Reynolds seuil, l'ébullition nucléée dans le film gouverne le transfert de chaleur; ce coefficient d'échange de chaleur local devient alors indépendant du nombre de Reynolds.

- En deçà, l'apparition de zones asséchées entraîne une forte chute du coefficient d'échange local.

Le coefficient de transfert de chaleur par évaporation de film est approximativement 1.3 fois plus important que le coefficient de transfert de chaleur en ébullition en vase et ce coefficient multiplicateur est fonction du flux de chaleur et de l'espacement entre les tubes mais pas des modes découlement du liquide.

A l'issue de ce travail, la compréhension des phénomènes impliqués dans l'évaporation des fluides réfrigérants en film tombant a été améiore. Une méthode pour prédire la limite d'apparition des zones sèches a été développée et une correlation pour le transfert de chaleur lors de l'évaporation en film tombant proposée. Elles constituent une amélioration significative pour la conception des évaporateurs à film tombant.

Acknowledgments

Firstly, I would like to thank Professor John Richard Thome for his complete confidence and the opportunity he gave me to achieve this work in his laboratory. He was all the time available for fruitful research discussions and his guidance and encouragement during this period were a benefit contribution to this study. He found time to read and make the English corrections of this report. Finally, I really appreciate the person for his comprehension and his sense of humor.

I would like to thank all the members of the Research Club who financially supported this work: Axima Refrigeration AG, Dunham-Bush Inc., Wolverine Tube Inc., Wieland-Werke AG and UOP Inc. Special thank to the last three companies who provided the tube samples to be tested. The Swiss Federal Institute of Technology (EPFL) was also a member of this Research Club.

I thank Professor François Avellan of the Laboratory of Hydraulic Machines, Swiss Federal Institute of Technology, Professor Alberto Cavallini, University of Padoua and Professor Olivier Zürcher, University of Applied Science of Fribourg for being the examiners of this thesis.

I would like to thank also all my colleagues of the Heat and Mass Transfer Laboratory with which the scientific discussions were often very interesting and constructive and especially the two mechanicians of the laboratory Laurent Chevalley and Freddy Thomas who brought to reality the experimental test facility needed for this research.

I would like to express my gratitude to Daniel Gstoëhl who made with me, the design and the conception of the test facility . He was first my collaborator and became rapidly my friend.

Finally, I would like to thank my wife Anne-Cécile for supporting me during this period and for being comprehensive in the time involved in this work.

Contents

List of Figures

List of Tables

Nomenclature

Symbol	Description	SI units
Normal letters		
A	area	$[m^2]$
c_p	specific heat at constant pressure	$[J/kgK]$
D	diameter of the tubes	$[m]$
d_o	bubble departure diameter	$[m]$
f	friction factor	$[-]$
g	acceleration due to gravity (9.81)	$[m^2/s]$
h	vaporization latent heat	$[J/kg]$
K_{ff}	falling film coefficient factor	[-]
$\dot{m}$	mass flow rate	$[kg/s]$
M	molecular weight	$[kg/kmol]$
P	pressure	$[kPa]$
q	local heat flux	$[W/m^2]$
R	thermal resistance	$[K/W]$
$\Re$	universal gas constant	$[Nm/kmolK]$
Ra	mean surface roughness (std a)	$[\mu m]$
Rp	mean surface roughness (std p)	$[\mu m]$
r_{nuc}	radius of vapor nucleus	$[m]$
r_w	thermal resistance	$[m^2K/W]$
s	intertube spacing (surface to surface)	$[m]$
T	temperature	$[K]$
tp	tube pitch	$[m]$
U	overall heat transfer coefficient	$[W/m^2K]$

Symbol	Description	SI units
Greek letters		
α	heat transfer coefficient	$[W/m^2K]$
β	contact angle liquid/material	$[deg]$
δ	falling film thickness	$[m]$
λ	thermal conductivity	$[W/mK]$
λ_d	Taylor instability wavelength	$[m]$
Γ	liquid flow rate on one side of the tube per unit length	$[kg/ms]$
2Γ	total liquid flow rate on the tube per unit length	$[kg/ms]$
μ	dynamic viscosity [Pa.s]	$[kg/ms]$
ν	kinematic viscosity (μ/ρ)	$[m^2/s]$
ρ	density	$[kg/m^3]$
σ	surface tension	$[N/m]$

Subscripts

cop	copper
$crit$	critical conditions
$dryout$	film breakdown
h	hydraulic (diameter)
f	friction factor
gni	Gnielinsky
i	inner part
$left$	left side
L	saturated liquid
LV	value at V - value at L
$middle$	middle value
$mean$	mean value
o	outer part
pb	nucleate pool boiling (α)
$plateau$	constant part
r	root (diameter)
$right$	right side
ref	refrigerant
sat	saturation conditions
$threshold$	onset of dryout
V	saturated vapor
wat	water
w	wall
ref	reference

Dimensionless numbers

C_i	multiplicative coefficient (Gnielinski correlation)
Ga	Modified Gallileo number ($\rho\sigma^3/\mu^4 g$)
K_{ff}	falling film coefficient (α_o/α_{pb})
Nu	Nusselt number
Pr	Prandtl number ($\mu c_p/\lambda$)
p_r	reduced pressure (P/P_{crit})
Re_L	liquid film Reynolds number ($4\Gamma/\mu_{ref}$)
Re_{wat}	water Reynolds number ($\rho_{wat}\overline{V}D_h/\mu_{wat}$)

Chapter 1

Introduction

Falling film evaporation is a phenomenon that takes place when a liquid is flowing in a film on a heated surface. Heat from the surface is transferred to the liquid and vapor is created. Depending on the conditions, this vapor is created at the liquid-surface interface (nucleate and convective boiling) or at the liquid-vapor interface (evaporation). These two effects could be also combined.

Compared to other types of evaporation processes, falling film evaporation presents several advantages: the amount of liquid is reduced compared to a flooded pool as it is flowing in a thin film on the surface, heat transfer is high and the temperature difference to achieve evaporation is thus reduced. Finally the pressure drop during the falling film evaporation process is limited: it is only necessary to pump the recirculated liquid from the bottom to the top of the evaporator (static heat corresponding to the height of the bundle). For these reasons, the falling film evaporation process has wide applications in various industrial fields and has been used for years. In food processing the benefit of the small temperature difference is employed, where it allows drying of heat sensible food like milk. In the refrigeration industry, the small temperature difference means a gain in the efficiency of the installations while the small amount of liquid necessary allows a reduction of the refrigerant charge by a factor 2 to 4 compared to classical evaporators.

Concerning falling film evaporation on horizontal tubes, some predictive methods are available but essentially for water and their utilization with other types of fluids, especially refrigerants leads to rough approximations. Moeykens et al. [MOEY94] presented some results of falling film evaporation (called by him spray evaporation) with R-134a but no predictive method was proposed. For these reasons, accurate predictive methods for falling film evaporation are necessary for design purposes.

The objectives of this study are to develop a significant experimental falling film heat transfer database and then a predictive method for falling film evaporators. For this purpose, a new test facility has been designed and

built. Measurements of local falling film heat transfer coefficients, including visualization of the liquid flowing in-between the tubes, were performed and a predictive method has been developed. In particular here, local falling film heat transfer data have been obtained rather than tube length averaged data as other previous studies.

The study starts with a state of the art review of the existing works in relation with the present one. Three main subjects are treated: falling film evaporation, nucleate pool boiling and film breakdown. The test facility specifically built for this project is then described with a detailed presentation of the instrumentation. The following chapter is dedicated to the Wilson plot technique utilized to determine the water side heat transfer coefficient in the copper tested tubes. The results of the measurements are then presented in three different sections: falling film evaporation, nucleate pool boiling and film breakdown. In the last chapter, the methods for predicting falling film evaporation heat transfer coefficients and onset of dryout are developed.

Chapter 2

State of the area of falling film evaporation

2.1 Evaporation

2.1.1 Pool boiling

Evaporation in pool boiling conditions is widely used and several correlations are available. With the tested heat flux range of the present study, it is likely that boiling occurs in the falling film. For comparison purposes, a review of interesting related works on this subject are presented. Relations from these works will be used as comparisons to the present results where appropriate later in this thesis. Table 2.1 lists these studies.

Danger et al. [DANGER01] presented results for pool boiling with R-134a on plain and enhanced tube surfaces. For their plain tube at $4bar$, they found the following relationship: $\alpha \sim q_o^{0.825}$. They also measured the tube surface superheat around the tube and found that for intermediate heat fluxes (5 to $20kW/m^2$), the superheat presents a minimum at the bottom of the tube which means a higher heat transfer coefficient. They supposed that this was due to gravity that is pushing the bubbles toward the surface at this position. The liquid superheated layer over the surface is so mixed and the heat transfer enhanced. For their enhanced surfaces (purely radially rectangular grooves and similar grooves with reentrant cavities) they found that the openings improved the heat transfer especially at low heat flux ($q_o \leqslant 5kW/m^2$). For higher heat fluxes (up to $50kW/m^2$), they found similar performances for both the plain and their enhanced tubes.

Smirnov [SMIR00] made heat transfer measurements in pool boiling conditions on multi-layered porous coated flat surfaces (both stainless steel layers and copper alloy layers). Within boiling conditions, he distinguished two different regions in term of heat flux. A first "boiling" regime for relatively low heat fluxes where the heat transfer coefficient was quite high and varied

Authors	Tube	D $[mm]$	Fluid	q'' $[kW/m^2]$	T $[K]$	Results
Tatara[TATA00]	B	19.05	R-134a	8 to 40	278	graphs
Barthau[BART00]	A	15	R-134a	1 to 100	282 to 356	equation
Danger[DANGER01]	A	25.4	R-134a	1 to 100	263, 282	equation
Smirnov[SMIR00]	D	flat	R-113	5 to 100	320	graphics
Thome[THOM03]	A, B	19.05	R-134a	15 to 40	278	equation
Hsieh[HSIE94]	A	27	R-134a	5 to 50	278	equation
Webb[WEBB92]	A, E	19.1	R-134a	8 to 60	278	equation
McNeil[MCNE02]	A, D	19	Pentane	5 to 50	309	equation
Memory[MEMO95a]	A, D, E	15.9	R-114	1 to 100	275	graphics
Kramer[KRAM97]	A, C	22.2	H2O, Ethanol	15 to 65	351 to 373	graphics

Table 2.1: Recent pool boiling studies at conditions close to the current study ones, A: Plain, B: Turbo-BII HP, C: Gewa-B, D: High-Flux, E: Turbo-B.

with $q_o^{-0.11 \text{ to } -0.25}$ and a second "pool boiling" regime where the behavior was more similar to pool boiling on a plain surface. This transition heat flux was $q_o = 25kW/m^2$ for R-113. Above this threshold, a pool boiling relation for the porous surface from his graphic is $\alpha = 0.479q_o^{0.789}$ which is valid from 25 to 100 kW/m^2. The author remarked that the heat transfer coefficient was only a function of the first porous layer and was not a function of the thermal conductivity of this layer. He mentioned also that the liquid supply method had no influence on heat transfer, the porous layer had just to be fully filled with liquid. He developed a mathematical model based on the porosity and the pore diameter.

Thome and Robinson [THOM03] performed a study on bundle boiling and they also made single-tube pool boiling tests. From those measurements with R-134a on $19.05mm$ O.D. copper tubes, they found for their plain tube: $\alpha_o = 10.56q_o^{0.66}$ with heat fluxes from 14 to $26kW/m^2$ at $277.6K$ ($4.5°C$). It is notable as the value of the exponent (0.66) is practically the same as in the Cooper pool boiling correlation (0.67). For the Turbo-BII HP tube, they found: $\alpha_o = 30.94q_o^{-0.042}$ with a heat flux from 16 to $40kW/m^2$ at $277.7K$ ($4.6°C$). The slope of α_o versus q is slightly negative similar to the results of Danger et al. noted above [DANGER01].

Barthau and Hahne [BART00] studied nucleate pool boiling on an horizontal $15mm$ O.D. plain copper tube. The surface of the tube was emery ground to a roughness Ra of $0.4\mu m$. They used R-134a with a pressure range from 400 to 2800 kPa. For a pressure of $400kPa$, close to that of

the the present study, they found the following relation for the pool boiling heat transfer coefficient: $\alpha_o = 2.55 q_o^{0.75}$. This relation is based on measured heat fluxes from 0.4 to $100 kW/m^2$. At this pressure and heat flux of $20 kW/m^2$, their measured heat transfer coefficient is 10% lower than the one recommended in the Wärmeatlas.

Tatara and Payar [TATA00] made pool boiling experiments with a horizontal $19.05 mm$ Turbo-BII HP tube. The refrigerant was R-134a and the test temperature was $278 K$. The heat flux was varied from 8 to $40 KW/m^2$. From the graphics of this study, it is possible to find the following relation: $\alpha_o = 13600 q_o^{0.069}$. This relation has been calculated with their data only from 16 to $40 KW/m^2$ where the relation between heat transfer coefficient and heat flux is linear in a log-log graph and presents a small slope, and this range is also comparable to the one of the current study. To explain the flatness of the curve, they suggested that the liquid cannot replenish the boiling cavities quickly enough. They globally found that the performance of the Turbo-BII HP is between 50% to 90% higher than the original Turbo-B tube.

Hsieh and Hsu [HSIE94] presented an interesting study of nucleate boiling on plain and rib-roughened tube geometries with several refrigerants, including R-134a. They tested a plain $27 mm$ O.D. copper tube at heat fluxes from 5 to $50 kW/m^2$. From their data with R-134a at $277.5 K$, it is possible to extract the following relation for the heat transfer coefficient $\alpha_o = 1.272 q_o^{0.784}$. The alignment of the data in a log-log graph is very good.

Webb and Pais [WEBB92] measured nucleate boiling heat transfer on plain, integral-fin and enhanced tube geometries. The goal was to determine the relative performances of two substitute refrigerants. R-123 and R-134a replace R-11 and R-12 because they contain less chlorine, which is active in the stratospheric ozone layer depletion. The result is that the change affects the performance within $\pm 10\%$. Correlations for R-134a boiling on a plain and a Turbo-B tube (both $19.1 mm$ O.D.) are given. At a temperature of $277.5 K$ and heat fluxes from 8 to $60 kW/m^2$ the relations between heat flux and heat transfer coefficient are: $\alpha_o = 10.23 q_o^{0.596}$ for the plain tube and $\alpha_o = 304.4 q_o^{0.389}$ for the Turbo-B tube. It is important to specify that this last relation is for the original Turbo-B tube and not for Turbo-BII HP (tested in the present work). Even though, it is worthwhile to make a comparison because they are from the same family of tubes.

Memory et al. [MEMO95a] made an interesting study of nucleate pool boiling of R-114 and R-114-oil mixture on smooth and enhanced surfaces with a single tube and with a tube bundle. Particularly, they tested a plain, a Turbo-B and a High-Flux $15.9 mm$ O.D. tubes. They presented their results in terms of an enhancement factor relative to the plain tube performance α/α_{plain} based on the outer diameter. For the Turbo-B tube, they found an enhancement factor of 6.2, 3.9 and 2.9 for heat fluxes q_o of respectively 24, 40 and $64 kW/m^2$. For the High-Flux, the enhancement factor were 7.4, 5.1

and 3.6 for heat fluxes of respectively 29, 49 and $78kW/m^2$. The values of the heat fluxes are unusual because they have been recalculated to follow the convention of the present work. The authors presented also curves of their measured heat transfer coefficients versus heat flux. The curves for the Turbo-B tube decreases slightly in the heat flux range of 10 to $100kW/m^2$ while the one for the High-Flux tube increases slightly in the same heat flux range. The large variation of the enhancement factor is mainly due to the classical plain tube thermal performance increase as a function of heat flux. For low heat flux ($q_o < 10kW/m^2$), the authors found a high enhancement factor for the Turbo-B and the High-Flux tubes. They suggested that there was still a significant number of active nucleation sites for these tubes at these low heat flux.

McNeil et al. [MCNE02] recently presented results for bundle boiling. The refrigerant was pentane boiling on plain and High-Flux ($19mm$ O.D.) tubes. The tubes were made of 90Cu:10Ni alloy and the porous layer on the enhanced tube was $0.08mm$ thick. To compare to bundle results, they also tested single tubes. With heat fluxes from 5 to $50kW$, they found the following relations: $\alpha_o = 5.16q_o^{0.573}$ for the plain tube and $\alpha_o = 651.72q_o^{0.256}$ for High Flux tube. The refrigerant is different compare to the current study but their results allow a direct comparison between plain and porous coated tube . The enhancement factors are, with their equations, 8.5 at $5kW/m^2$ and 4.1 at $50kW/m^2$.

Kramer et al. [KRAM97] published the results on cross flow and pool boiling of water, ethanol and water-ethanol mixtures on a horizontal $22.2mm$ O.D. Gewa-B tube. They present their results in terms of an enhancement factor (compared to the plain tube). In pool boiling conditions and at a heat flux of $19kW/m^2$, this enhancement factor was 9 for water, 6-8 for the mixtures and 11 for pure ethanol. When the heat flux was raised to $62kW/m^2$, this enhancement factor decreases to 5 for water, mixtures and pure ethanol. Test have also been performed with a vertical velocity of the single phase flow around the tube. No real change was observed with a liquid velocity up to $0.1m/s$. The authors think that the boiling phenomenon takes place mainly inside the sub-surface of the Gewa-B tube into which the external single phase cross flow cannot penetrate.

Below, some classical nucleate pool boiling correlations are presented. They are valid only for plain tubes with a given roughness but are usually derived from large set of data: numerous liquids and pressures.

Stephan and Abdelsalam [STEP80] compiled a large boiling database to find correlations for the heat transfer coefficient. After selecting the key parameters for boiling, they combined them together in several dimensionless numbers. They then made two statistical regressions with the data, resulting in four boiling correlations (for water, hydrocarbons, cryogenics and refrigerant). For the refrigerants, the relation has the following form

$$\frac{\alpha_o d_o}{\lambda_L} = 207 \left(\frac{q_o d_o}{\lambda_L T_{sat}} \right)^{0.745} \left(\frac{\rho_L}{\rho_V} \right)^{0.581} Pr_L^{0.533} Rp^{0.133} \tag{2.1}$$

where Pr is the Prandtl number and Rp is the mean surface roughness in μm.

$$Pr = \frac{\mu_L}{c_{p,L} \lambda_L} \tag{2.2}$$

and d_o is the bubble departure diameter obtained from

$$d_o = 0.0146\beta \left(\frac{2\sigma}{g\left(\rho_L - \rho_V\right)} \right)^{0.5} \tag{2.3}$$

with β the contact angle of the liquid/material combination assigned by them to have a fixed value of 35°. Rp has been set to $1\mu m$ for the regression but the authors mention that if the roughness is known, it is worth to make the correction. Equation 2.1 gives the following relation for R-134a boiling on our plain copper tube with a measured mean roughness $Rp = 2\mu m$ and at $278K$ $(5°C)$

$$\alpha_o = 1.989 q_o^{0.745} \tag{2.4}$$

For the particular case of R-134a boiling on a plain tube, Webb and Pais [WEBB92] and Chiou and Lu [CHIO97] mention that the Stephan Abdelsalam's correlation underpredicts their data by 25%.

Cooper [COOPER84] compared physical property based correlations to reduced pressure type correlations, and observed that the physical properties (such as viscosity, thermal conductivity, surface tension ...) could also be expressed in terms of the reduced pressure, p_r. Consequently, he concluded that a reduced pressure form of pool boiling correlation was the most sensible approach and he proposed the following method

$$\alpha_o = 55 p_r^{0.12 - 0.4343 \ln Rp} \left(-0.4343 \ln p_r\right)^{-0.55} M^{-0.5} q_o^{0.67} \tag{2.5}$$

Where M is the molecular weight of the liquid ($102 kg/Kmol$ for R-134a) He recommends a multiplying factor of 1.7 for horizontal copper cylinder. Equation 2.5 gives the following expression for R-134a boiling on our plain copper tube with a measured mean roughness $Rp = 2\mu m$ at $278K$ $(5°C)$ and with including the multiplicative factor of 1.7

$$\alpha_o = 13.94 q_o^{0.67} \tag{2.6}$$

Gorenflo [GOREN93] proposed another type of reduced pressure correlation by introducing a fluid specific heat transfer coefficient. The method uses a reference heat transfer coefficient, α_{ref}, measured for each fluid at fixed reference conditions $p_{r,ref} = 0.1$, $Ra_{ref} = 0.4\mu m$ and $q_{ref} = 20 kW/m^2$. The value of this reference heat transfer coefficient α_{ref} for R-134a is:

$4500 W/m^2K$. The nucleate boiling heat transfer coefficient α_o at other conditions of pressure, heat flux and roughness is then calculated from

$$\alpha_o = \alpha_{ref} F_{PF} \left(q_o/q_{ref}\right)^{nf} \left(Ra/Ra_{ref}\right)^{0.133} \tag{2.7}$$

where the pressure correction factor F_{PF} is

$$F_{PF} = 1.2 p_r^{0.27} + 2.5 p_r + \frac{p_r}{1 - p_r} \tag{2.8}$$

and the heat flux exponent nf is also a function of the reduced pressure

$$nf = 0.9 - 0.3 p_r^{0.3} \tag{2.9}$$

Compared to other general correlations, the exponent of the heat flux factor is a function of the reduced pressure, and the exponent on the roughness influence is similar to that the Stephan Abdelsalam correlation equation 2.1. Equation 2.7 correlation can be reduced to the conditions of the current study: R-134a boiling on plain copper tube with a measured mean roughness Ra=$0.8 \mu m$ at $278K$ ($5°C$).

$$\alpha_o = 2.55 q_o^{0.76} \tag{2.10}$$

It is mentioned in [GOREN93] that the reference value α_{ref} of $4500 W/m^2K$ for R-134a is based on a small experimental database. This reference heat transfer coefficient has been measured in [BART00] resulting in a value of $4170 W/m^2K$. In another work, Gorenflo et al. [GOREN00] have measured the heat transfer coefficient for boiling conditions on a $15mm$ O.D. plain tube. The roughness of the tube was Ra=$0.25 \mu m$. Applying the same roughness correction as in equation 2.7, it is possible to calculate from the measurements a reference heat transfer coefficient. The result is: $\alpha_{ref} = 3890 W/m^2K$. From this, it is clear that the value of 4500 is too high. Using 4180 (mean between the three references) as α_{ref}, the above equation becomes

$$\alpha_o = 2.37 q_o^{0.76} \tag{2.11}$$

This equation will be considered as Gorenflo's correlation applied to our test conditions.

2.1.2 Falling film evaporation

In this part, the interesting works about falling film evaporation are presented, the available prediction methods will be used as comparison.

Thome [THOM99] made a very detailed state of the art review on falling film evaporation. Most of the publications (until 1998) on the subject are presented and all the important parameters influencing heat transfer are discussed.

Moeykens with different coworkers made series very interesting studies on the falling film evaporation. They named this spray evaporation because they mainly used nozzles to feed the tube at the top. They studied plain and enhanced geometries in single tube and bundle configurations. The refrigerants used were R-134a (mainly), R-123 and R-22. They also investigated the influences of the nozzle type and the oil effects. Details on their publications are given below:

Moeykens and Pate [MOEY94] described their new spray evaporation test facility and reported experimental results for R-134a at $275K$ ($2°C$) for falling film evaporation. They tested $12.7mm$ and $19.1mm$ diameter copper plain tubes. They were able to make accurate measurements confirmed by comparing natural convection coefficients they measured in a liquid pool to the Churchill and Chu correlation, and by comparing their pool boiling data to the Stephan Abdelsalam correlation [STEP80] and data taken by Webb and Pais [WEBB92]. As a liquid distributor they used, over a total length of $406mm$, five wide angle nozzles. To find the effective amount of liquid impinging the tube surface $2 \times \Gamma_{eff}$, they multiplied the total flow rate by a collector test fraction of 19.3% for the $19.1mm$ tube and 14.3% for the $12.7mm$ tube. Two types of nozzles were used: a low pressure drop ($0.02MPa$) and a high pressure drop ($0.86MPa$). They found the following trends:

- The smaller tube gave 5-10% better performance than the larger one.
- The boiling performance was affected by refrigerant supply rate only when dryout became involved since their heat flux range was in the nucleate boiling mode.
- The high pressure nozzle yielded better heat transfer coefficient because of its impinging jet effect on the top tube row while the low pressure nozzle gave a wider angle of liquid spray.

Figure 2.1 illustrates the drop of the falling film heat transfer coefficients as the heat flux increases for the $19.1mm$ tube. This drop is more pronounced for the lower liquid overfeed. In the middle heat flux range from 18 to $25kW/m^2$, the falling film performance is slightly higher than the pool boiling one. The drop of the performance is thought to come from film breakdown (section 2.2). Their data thus suggest two film breakdown thresholds: $q_o \approx 26kW/m^2$ for $\Gamma = 0.013kg/ms$ and $q_o \approx 35kW/m^2$ for $\Gamma = 0.018kg/ms$.

Moeykens et al. [MOEY95a] extended their study on R-134a falling film evaporation to single enhanced tubes. As they utilized nozzles, they multiplied the total flow rate by a collector test fraction of 19.3% to find the effective amount of liquid impinging the tube surface. The tests were conducted at a constant liquid overfeed: $\Gamma = 0.0013kg/ms$ and heat flux

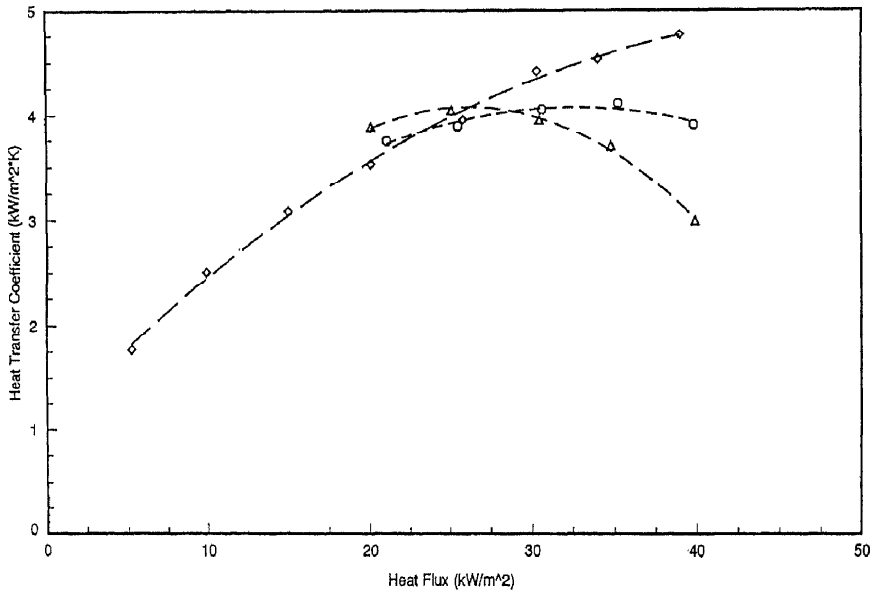

Figure 2.1: Moeykens et al. [MOEY94] falling film coefficients for R-134a on a single plain tube.($\circ\ \Gamma_{eff} = 0.018kg/ms$, $\triangle\ \Gamma_{eff} = 0.013kg/ms$, $\diamond$ flooded evaporator).

based on the nominal diameter of the tubes ($19.1mm$) ranged from 5 to $40kW/m^2$. The refrigerant was at $275K$ ($2°C$). Figure 2.2 shows a comparison of the enhanced tubes geometry tubes to the plain tube. The best falling film geometries were the enhanced condensing tube geometries, which were more effective in promoting thin film evaporation similar to what they were designed to do for falling film condensation. The condensing tube W-SC presents a weak dependance on the wall heat flux. The primary mode of heat transfer in this case is thin film evaporation, which is independent of heat flux. The authors observed nucleate boiling only near the bottom of the tubes, where the liquid layer was thickest but think that both evaporation and boiling occurred simultaneously. The boiling was limited by the low overfeed and the reduction in performance at high heat fluxes resulted thus from partial dryout on the tubes. The low finned tubes (not shown in figure 2.2) gave performances in the range of about 6000-7500W/m^2K. The best falling film tube (Turbo-Cii) gave from 9-30% lower performance in the falling film mode than comparable Turbo-B pool boiling data. As this condensing tube is the best one in falling film conditions (better than Turbo-B), the Turbo-B is better in pool boiling than in falling film conditions.

Moeykens et al. [MOEY95b] next extended these tests to a small tube

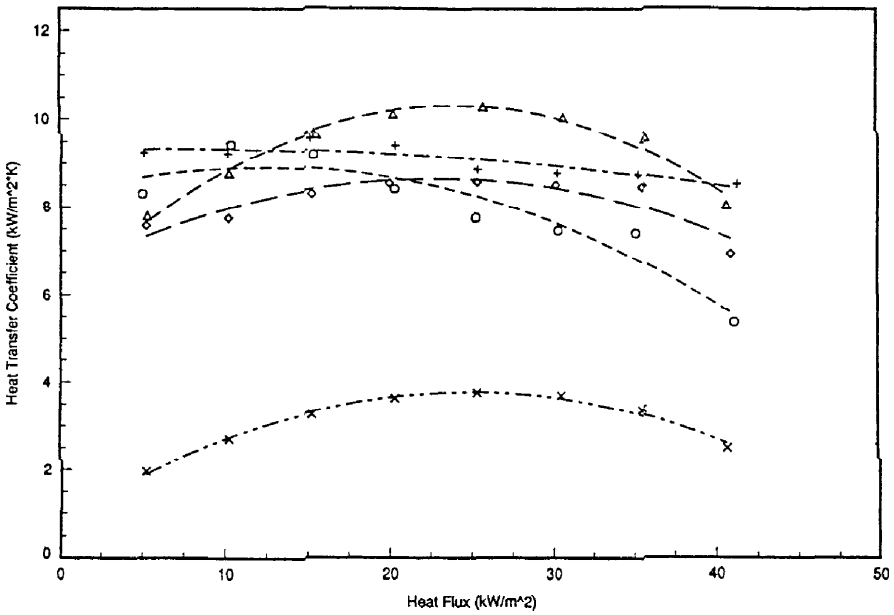

Figure 2.2: Moeykens et al. [MOEY95a] falling film coefficients for R-134a on single enhanced tubes ($\circ$ Turbo-B, $\triangle$ Turbo-Cii, $\diamond$ Wieland-SE, $+$ Wieland-SC, $\times$ Plain).

bundle comprised of 20 tubes, in triangular tube layouts. The vertical tube pitch was $19.1mm$ while the horizontal tube pitch was $22.2mm$. The refrigerant was pure R-134a at a saturation temperature of $275K$ ($2°C$). The heat flux range was 20 to $40kW/m^2$ and the bundle overfeed ratios varied from 1.4 to 7.9 (ratio between refrigerant flow rate supplied to the tubes to the refrigerant flow rate that evaporates). The same types of tubes with the exception of the 26 fpi (1024fpm) low finned tube, were tested as above and Wilson plots were used to accurately measure coefficients on individual tubes in the center vertical tube row. For a heat flux of $40kW/m^2$, the authors found that a variation in the bundle overfeed ratio from 1.4 to 3.8 had a weak effect (less than about 13%) on the shell side heat transfer coefficient. This influence was more pronounced at lower heat fluxes with less or no boiling visible, the heat transfer coefficient was higher at low flow rates. They also verified that $2K$ of subcooling had no effect on the bundle heat transfer coefficient. With Turbo-B tubes, the bundle heat transfer coefficient was found to be 3.5 times higher than with the plain tubes and as in the previous study, the Turbo-Cii gave by far the best performance. A row performance analysis was also performed with the Turbo-B tubes; it

was found that the heat transfer coefficient decreased from the top to the bottom (like for the other tubes), except at low heat fluxes, where the performance of the last tube was higher than the third one. Concerning pool boiling comparison, the best tube in falling film evaporation – Turbo-Cii – nearly doubled the performance of the Turbo-B in pool boiling.

The effect of nozzle height and orifice size were investigated by Moeykens and Pate [MOEY95c] for spray evaporation on a 40 fpi (1575 fpm) low finned tube bundle (the same as above). Five different nozzles were tested with orifice diameters ranging from 4.0 to $5.6mm$ that gave circular spray patterns, with the nozzles located at heights above the bundle from 41.3 to $66.7mm$, all for $0.172bar$ low pressure drop type nozzles. Their falling film coefficients at the optimal film-feed rate were measured to be higher than those for pool boiling on the same tube bundle. The advantages of square nozzle spray patterns compared to circular spray patterns diminished with increasing overlap of the sprays from adjacent nozzles. The 40 fpi tubes were noted to be prone to local dryout because the low fins inhibited the longitudinal spreading of the liquid along the tubes. With a bundle overfeed ratio of 7.3, the performance of the fourth row was still 40% lower than the one of the top tube. Examining the row by row performance, it was found that the triangular-pitch arrangement of the tubes induces a "saw-teeth-effect": despite a general performance decrease from the first row to the fourth row, the third row performed better than the second one. Row 1 received the fully developed spray from the nozzle and row 3 lies directly below row 1 while row 2 received liquid refrigerant primarily from dripoff from row 1 because of the gap between the tubes in row 1. The decrease of the bundle load reduces this difference between the tube row performances.

Moeykens and Pate [MOEY96a] extended their earlier tests to cover R-134a with oil for staggered tube bundles for four types of tubes: plain, 40 fpi (1575 fpm) low fin, Gewa-SC and Turbo-B. Oil effects were investigated using a 340 SUS polyol-ester oil, testing 1.0 and 2.5 wt.% oil mass fractions in the liquid feed onto the top of the tubes. The tube bundles had the same geometry as their prior low finned tube bundle. R-22 with a 300 SUS alkyl benzene oil was also tested on plain tube and Turbo-B tube bundles. Both refrigerants were used for spray distribution measurements on the bundles. The oils promoted foaming, which was quoted as enhancing heat transfer by retarding the formation of dry patches on the bundles. For example, increase in heat transfer performance by nearly 100% was noted for the Turbo-B bundle at a heat flux of $23kW/m^2$ and the finned tube bundle at a heat flux of $40kW/m^2$ with the 2.5% oil concentration in comparison with the pure R-134a results (at $\Gamma = 0.064kg/ms$). It was also observed that the amount of foam being generated on the tube bundle was greater at high heat fluxes. The test showed a dependence on both the bundle film feed flow rate (α increased with feed flow rate for the present test conditions) and oil concentration. Since oil would normally decrease boiling performance, most

likely the increase they found was due to the oil's effect in the sprayer, not an enhancing effect of the oil as they concluded.

Finally Moeykens et al. [MOEY96b] extended their falling film tests to R-123/oil mixtures for staggered and inline tube bundles for staggered and inline bundles with plain, Turbo-Cii and Turbo-B tubes at a saturation temperature of $275K$ ($2°C$). A 303 SUS naphthenic mineral oil was used but curiously only caused foaming on the plain tubes. The Turbo-B tube provided better performance than the Turbo-Cii and its falling film performance was about 2 to 2.6 times that of its pool boiling performance. Concerning the liquid film supply rates, the authors mentioned a lower limit to avoid dryout on the tubes. For their test conditions (q=20 to $40kW/m^2$), this limit on the bottom tube was $\Gamma = 0.04kg/ms$. For lower flow rate, they observed a bundle performance decrease. The Turbo-B tube was found to perform better (6 to 17%) in a rectangular pitch arrangement than in a triangular pitch arrangement.

Zeng et al. [ZENG94] investigated film flow distribution on plain, 40 fpi (1575 fpm) low fin and longitudinally grooved (O.D. $19.05mm$) tubes with water and without heat transfer. The distributer system was comprised of conical spray nozzles spaced to obtain an overlap zone between the sprays. For the first tube arrangement: 3 rows$\times$1 columns, it was found that the longitudinal non uniformity due to the overlap in the distribution is maximum for the top tube and decrease from row to row for the plain and the longitudinally grooved tubes. For the 40 fpi low fin tube, the fins were found to promote the non-uniformity and the liquid distribution peaks were higher for the bottom tube. Tests were also performed to compare the liquid distribution with a 9 tube bundle with a rectangular pitch to one with a triangular pitch. With the triangular pitch, each tube at the top received differing amounts of liquid because there are tubes in the storm blocking the spray to the second row. This arrangement was thought by the authors to increase the heat transfer in the case of film evaporation (thin film) but presents more risk of dryout. With the rectangular tube pitch, the tubes received the liquid more uniformly (flowing from the bottom of the tube above).

Zeng et al. [ZENG95] have continued their preceeding study with falling film evaporation of ammonia on a single stainless steel plain tube($19.05mm$ O.D.). The effects of heat flux, saturation temperature, spray flow rate and nozzle height were investigated. Both standard angle and wide angle nozzles were tested. The experiments were run using a modified Wilson plot approach that yielded tube-side coefficients within 5% of those of the Gnielinski [GNIE76] correlation, and thus the falling film heat transfer coefficients for ammonia were accurately obtained. They found that the heat transfer coefficients increased with heat flux and their coefficients for falling film evaporation were higher than the pool boiling ones (measured or from the Stephan Abdelsalam correlation [STEP80]) especially at high

heat fluxes. In between, at intermediate heat fluxes, the curve of falling film heat transfer coefficient presents a change in slope. The heat flux at which this took place was a function of the saturation temperatures. It occured at higher heat fluxes with lower saturation temperatures. Figure 2.3 depicts their test results at four saturation temperatures from $250K$ (-$23°C$) to $283K$ ($10°C$), all at nearly the same liquid feed rate. The Parken et al. correlation [PARK90], based on data with water, predicted only the high saturation temperature data at medium and high heat fluxes well despite the similarity of physical properties between water and ammonia. The influence of the liquid flow rate was also investigated: at low saturation temperature (up to $272K$, -$1°C$), it was found that the heat transfer coefficient does not vary significantly with the liquid flow rate. The authors concluded in there to be a non-boiling turbulent film in accordance with other studies. At higher temperatures, the heat transfer coefficient increased with flow rate. Boiling in the film was supposed in these conditions.

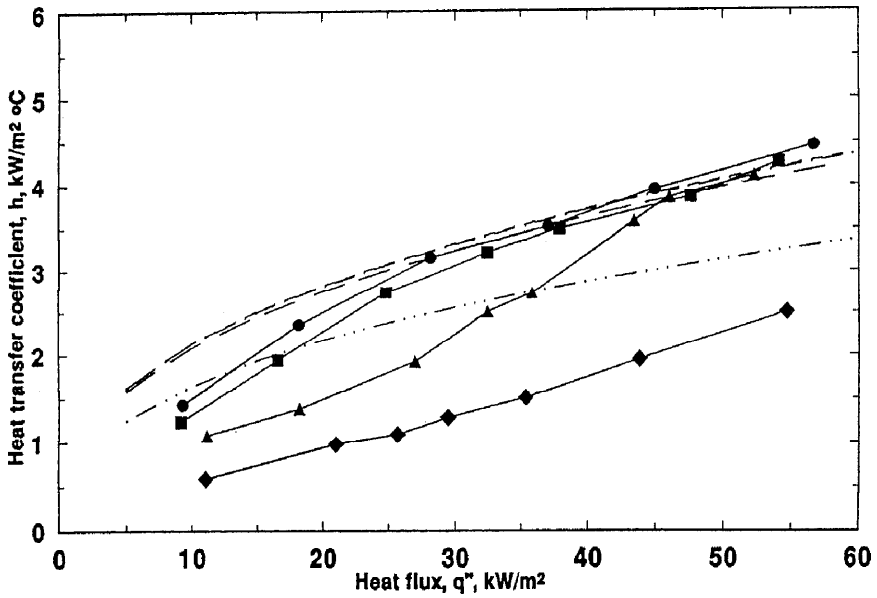

Figure 2.3: Zeng et al. [ZENG95] falling film coefficients for ammonia on single plain tube (• $283K$ and $\Gamma = 0.018kg/ms$, ■ $272K$ and $\Gamma = 0.0179kg/ms$, ▲ $261K$ and $\Gamma = 0.0189kg/ms$, ♦ $250K$ and $\Gamma = 0.0193kg/ms$; dashed lines are predictions of the Parken et al. correlation [PARK90]).

Zeng et al. [ZENG97] extended their single tube spray evaporation tests to a 3×3 square layout with a 1.25 pitch ratio tube bundle ($19.1mm$ stainless steel tubes). Ammonia was used between $250K$ (-$23°C$) and $283K$ ($10°C$)

and the heat flux range was from 3 to $35 kW/m^2$. Generally, heat transfer coefficients for the test bundle in falling film conditions were found to be higher than in pool conditions (up to 48% at high heat flux). The performance of the top rows was also higher due to the impact of the droplet from the nozzles. Similarly to the single tube tests, the heat transfer coefficients were increasing with heat flux. The authors described three general situations, observed with wide angle nozzles, about the impact of the film flow rate: 1: At low saturation temperature where more superheating is necessary for boiling, Γ has a weak influence on the heat transfer coefficient. 2: At high saturation temperatures nucleate boiling become active and the heat transfer coefficient of the boiling film increases with Γ. 3: At high heat fluxes (any saturation temperature), nucleate boiling becomes predominant and heat transfer is insensible to the film flow rate. The effects of the nozzle height and angle were small on the bundle performance. Figure 2.4 shows their results at a temperature of $272K$ (-1°C) for a liquid flow rate $\Gamma = 0.24 kg/ms$ with wide angle nozzle located $50.8mm$ above the top tubes. They measured the bundle boiling performance (dashed line) and compared it with the single tube boiling correlation of Stephan Abdelsalam [STEP80] shown by the solid line. The bundle in the flooded evaporator mode performs only slightly better than predicted for a single tube while in falling film mode, the performance is better by a factor of 1.5 to 2 times. The authors proposed a correlation for their square (3×3) tube layout incorporating both film evaporation and nucleate boiling effects for predicting the mean bundle heat transfer coefficient as

$$Nu_L = 0.0495 Re_L^{-0.00399} Pr_L^{0.209} p_r^{0.261} \Phi^{0.722} \tag{2.12}$$

Compare to the falling film heat transfer correlation from Chun and Seban [CHUN71], the reduced pressure p_r and a heat flux term Φ have been added to take into account the nucleate boiling effects. The Nusselt number and the non-dimensional heat flux are defined as:

$$Nu_L = \frac{\alpha_o}{\lambda_L} \left(\frac{\nu_L^2}{g} \right)^{1/3} \tag{2.13}$$

$$\Phi = \frac{q_o D}{(T_{crit} - T_{sat})\, \lambda_L} \tag{2.14}$$

This empirical method predicted their limited tube bundle data to within about ±20% for their range of saturation temperatures. They also correlated their results from their previous work on a single tube [ZENG95] and found the following relation

$$Nu_L = 0.0518 Re_L^{-0.0039} Pr_L^{0.278} p_r^{0.385} \Phi^{0.753} \tag{2.15}$$

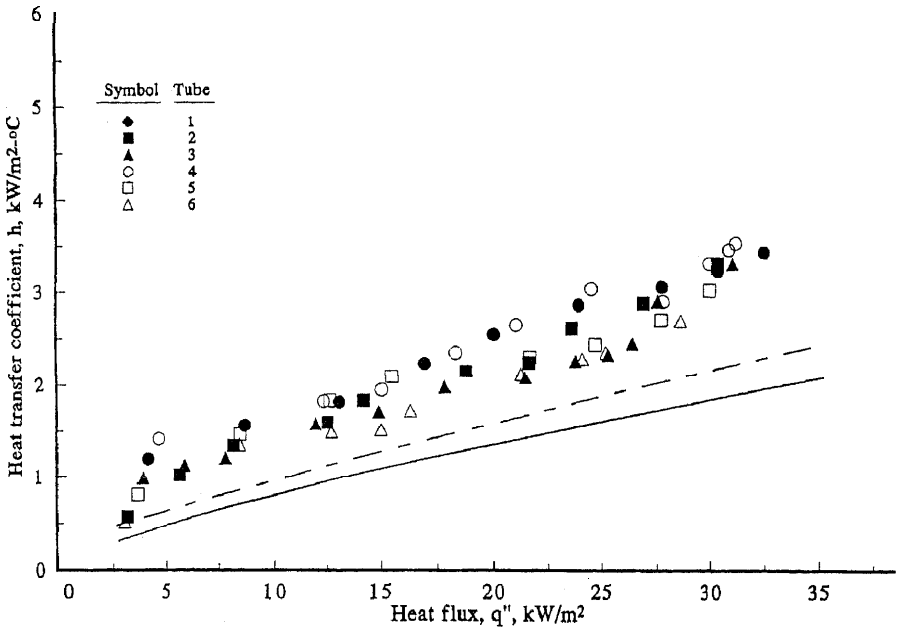

Figure 2.4: Zeng et al. [ZENG97] spray evaporation performance data for ammonia (outside vertical tube row is numbered 1 to 3 from top to bottom, center tube row is numbered 4 to 6 from top to bottom). Dashed line: bundle boiling, solid line: single tube boiling [STEP80].

In the equations 2.12 and 2.15, it is notable that the flow rate (Re_L) has a weak influence on the heat transfer.

Chyu et al. [CHYU82] measured falling film heat transfer coefficient for water on various single tubes with heat fluxes from 1 to $100kW/m^2$. On their plain tube, their measurements were well predicted by the Chun and Seban [CHUN71] correlation while the Lorenz and Yung [LORE79] method overpredicted them. The thermal history (increasing or decreasing heat flux, stepwise or continuous variation) and the liquid flow rate had weak influence on the results. The onset of boiling was at a heat flux of $q_o \approx 20kW/m^2$ and the onset of dryout was at $q_o \approx 40kW/m^2$. On a High Flux porous coated tube, they observed smaller bubbles with higher frequency in the film and no dry spots. They thought that the smaller bubbles should not disrupt the film. Hysteresis was noted in the boiling region of their data (heat transfer coefficient was higher when decreasing the heat flux). Incipient boiling superheat was only $1.3K$. A Gewa-T tube was also tested and gave better performance at low wall superheats in the absence of nucleate boiling by promoting enhanced thin film evaporation.

Chyu and Bergles [CHYU85a], [CHYU87] presented a model for pre-

dicting falling film coefficients by zone around a plain tube without boiling. From top to bottom, three zones were defined: 1) the jet impingement region, 2) the thermal developing region characterized by hydrodynamic and thermal development and evaporation at the free surface and 3) the fully developed region where heat is transferred through the film only by conduction. For each region, an analysis is made to determine its size and the heat transfer coefficient. The resulting overall heat transfer coefficient is a weighted average of each zone. Tests were performed with water at atmospheric pressure flowing on a single plain $25.4mm$ O.D. tube. The heat transfer model using Chun and Seban correlation in the fully developed region predicted the data quite well except at high heat fluxes ($q \approx 200kW/m^2$) where the heat transfer coefficient was high and independent of the film feed rate (nucleate boiling was reached). Liquid feed height and wall superheat had a weak influence on heat transfer.

Chyu and Bergles [CHYU85b], [CHYU89] extended their prior study to three enhanced evaporation tubes: Wieland Gewa-T, Hitachi Thermoexcel-E and High-Flux plus plain tube all with water. At low heat fluxes and for all the tubes, falling film heat transfer coefficients were found higher than pool boiling ones. When increasing thermal loads, the heat transfer coefficients from these two modes tend to merge (at approximately $60kW/m^2$ for the plain tube or the High-Flux) and remain the same for higher heat flux. For the High-Flux tube, hysteresis was present: higher heat transfer coefficients were measured when decreasing heat flux compared to increasing. With the former conditions, all the nucleation sites are activated by the high thermal load and remain activated. Falling film evaporation on the High-Flux porous surface featured generation of numerous tiny bubbles at high frequency that did not significantly disturb the film. Heat transfer coefficients with High-Flux and Thermoexcel-E surfaces were found independent of the film flow rate, except at very low heat flux levels. This was due to the predominant heat transfer mode of those surfaces: enhanced nucleate boiling.

Chun and Seban [CHUN71] measured heat transfer coefficients for water on a vertical tube in both laminar and turbulent flow regimes. They also presented correlations for predicting heat transfer and the threshold between laminar and turbulent flow in non boiling conditions. Compared to liquid flowing on horizontal tubes, the liquid flow has here a longer distance to develop compare to the half of the circumference of one tube in the present study. Despite that, the heat transfer coefficients present an interesting and classical behavior: in a log-log graph, the Nusselt number decreases linearly with Re number to the laminar/turbulent transition. It increases then a little and reaches a constant value for larger liquid flow rates. When changing the liquid, this behavior remains the same, the curve is just shifted. Their correlations for the laminar region is:

$$is : Nu_L = 0.822 Re_L^{-0.22} \tag{2.16}$$

and for the fully turbulent region is:

$$Nu_L = 3.8 \cdot 10^{-3} Re_L^{0.4} Pr^{0.65} \tag{2.17}$$

while the relation to determine the transition from laminar to turbulent film is given by

$$Re_L = 5800 Pr^{-1.06} \tag{2.18}$$

This expression for R-134 at $278K$ ($5°C$) gives $Re = 1400$. Butterworth [BUTTW90] recommends a value of 1600 in condensation on a vertical plate.

Danilova et al. [DANI76] studied a horizontal tube bundle that was six rows deep and had one or three columns of plain tubes. The refrigerants used were R-12, R-22 and R-113. Liquid flow rate ($\Gamma = 0.07$ to $0.150 kg/sm$), tube pitch, heat flux ($q = 0.5$ to $25 kW/m^2$) and saturation temperature ($T_{sat} = 233K$ to $273K$) influences were investigated. Figure 2.5 shows some of their experimental results for R-22 at different saturation temperatures. The mean falling film heat transfer coefficient for single row is plotted as a function of the heat flux (α =f(q)) for different liquid overfeeds. The curves present three main zones: 1) at low heat flux, heat transfer coefficients are mainly a function of the liquid flow rate and increases with it, it is the evaporation zone, 2) at middle heat fluxes (from 6 to $16 kW/m^2$ depending on the saturation temperature) there is a transition region, 3) for higher heat fluxes, α is only function of the heat flux where the boiling is developed. The film Reynolds numbers of those measurements are respectively from the lowest flow rate to the highest: ≈ 300, ≈ 1200 and ≈ 2400 (the Re numbers are function of the temperature). Similar curves were obtained for R-12 and R-113.

Data were correlated with two equations, one for vaporization

$$Nu_L = 0.035 Re_L^{0.22} Re_{*film}^{0.04} Pr_L^{0.32} \left(\frac{s+D}{D} \right)^{0.48} \tag{2.19}$$

and one for boiling

$$Nu_* = 1.32 \cdot 10^{-3} Re_*^{0.63} Kp^{0.72} Pr_L^{0.48} \tag{2.20}$$

in which the Nusselt number Nu_L is defined by equation 2.13, the Prandtl number by equation 2.2 and the film Reynolds number Re_L by

$$Re_L = \frac{4\Gamma}{\mu} \tag{2.21}$$

the other specific dimensionless parameters are

$$Re_{*film} = \frac{q}{h_{LV} \rho_V \nu_L} \left(\frac{\nu_L^2}{g} \right)^{1/3} \tag{2.22}$$

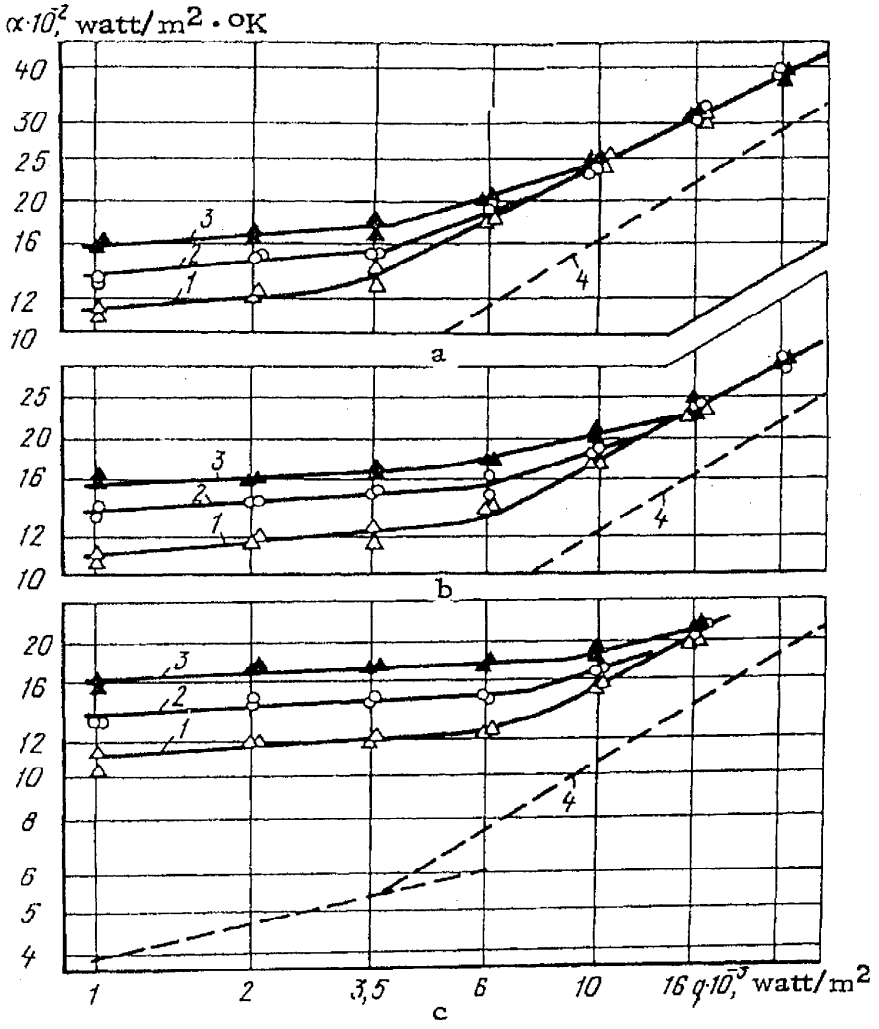

Figure 2.5: Danilova et al. [DANI76] average heat transfer coefficients for R-22 on plain tubes as a function of heat flux, saturation temperatures T_{sat} are: a) 273; b) 253; c) 233 K and liquid flow rate Γ are: 1) 0.0202; 2) 0.0802; 3) 0.161 kg/ms; 4) pool boiling.

$$Nu_* = \frac{\alpha_o}{\lambda_L}\left(\frac{\sigma}{g(\rho_L - \rho_V)}\right)^{0.5} \tag{2.23}$$

$$Re_* = \frac{q}{h_{LV}\rho_V\nu_L}\left(\frac{\sigma}{g(\rho_L - \rho_V)}\right)^{0.5} \tag{2.24}$$

$$Kp = \frac{P}{\sigma}\left(\frac{\sigma}{g(\rho_L - \rho_V)}\right)^{0.5} \tag{2.25}$$

No relation was given to determine the transition in the vaporization/nucleate boiling heat flux but these correlations predicted the data within $\pm 15\%$. It is noticeable that the tube pitch ratio and the film Reynolds Re_L number have an influence only in the vaporization equation. For the nucleate boiling equation, the Reynolds number used (Re_*) is the same as that in the Rohsenow [ROHS62] pool boiling equation.

Parken et al. [PARK90] presented a study on water falling film evaporation on a single plain tube (O.D. $25.4mm$ and $50.8mm$). Local heat transfer measurements showed always a maximum value at the top of the tube (0 rad). Lateral positions ($+\pi/2$, $-\pi/2$) showed a minimum value at non boiling conditions and erratic behavior in boiling conditions. At the bottom of the tube (π), the heat transfer coefficient was always lower than at the top. Concerning average heat transfer coefficients, in non boiling conditions, the values increased with liquid flow rate and were insensible to the heat flux while in boiling conditions, heat transfer coefficients increased with both heat flux and liquid flow rate. In boiling conditions, heat transfer coefficients were significantly higher for the $50.8mm$ diameter tube than for the $25.4mm$ tube. They though that the length to superheat the liquid was the same for both tubes so that the larger tube presents a larger percentage of surface where boiling is present. The results were correlated similarly to Chun and Seban [CHUN71] in two equations:

for non boiling conditions

$$Nu_L = \frac{\alpha_o}{\lambda_L}\left(\frac{\nu_L^2}{g}\right)^{1/3} = 0.042 Re_L^{0.15} Pr_L^{0.53} \tag{2.26}$$

and for boiling conditions

$$Nu_L = \frac{\alpha_o}{\lambda_L}\left(\frac{\nu_L^2}{g}\right)^{1/3} = 0.00082 Re_L^{0.1} Pr_L^{0.65} q_o^{0.4} \tag{2.27}$$

These equations with a mean deviation of 7-10% are valid for the $25.4mm$ tube, other expressions that give approximately a Nusselt number 10% higher were presented for the $50.8mm$ tube.

Lorenz and Yung [LORE78] and [LORE79] have presented a simple but complete analytical model of falling film evaporation on a plain tube. The agreement with their measurements with water and from other studies was relatively good. The model split the liquid flow around the tube in two regions: the thermal developing region with a length L_d from the top in which heat is employed only to superheat the liquid (no evaporation) and a fully developed region where the evaporation takes place and the liquid flow is laminar or turbulent. A boiling contribution was included by adding a

heat boiling heat transfer coefficient to the evaporation one. For the thermal developing region, the length on the circumference of the tube is defined by

$$L_d = \frac{c_{pL}\Gamma^{4/3}}{4\pi\lambda_L}\left(\frac{3\mu_L}{\rho_L^2 g}\right)^{1/2} \tag{2.28}$$

The heat transfer coefficient, calculated from an energy balance, is α_{od} for this region

$$\alpha_{od} = \frac{3C_{pL}\Gamma}{8L_d} \tag{2.29}$$

For the fully developed region from L_d to the bottom of the tube, the heat transfer coefficient is calculated by the Chun and Seban model [CHUN71] presented above including a distinction between laminar and turbulent conditions with the correlation for the transition Reynolds number. For the boiling heat transfer coefficient α_{ob} to be applied all around the tube, Lorenz and Yung used the Rosenhow equation [ROHS62] but more accurate relations have been developed and should be used instead like the Stephan and Abdelsalam one [STEP80].

The average heat transfer coefficient was assumed to be a superposition of convective heat transfer and boiling and is calculated around the entire circumferential length of the tube ($L = \pi D/2$) with

$$\alpha_o = \alpha_{ob} + \alpha_{od}\frac{L_d}{L} + \alpha_o c\left(\frac{L - Ld}{L}\right) \tag{2.30}$$

The convective and boiling heat transfer coefficient are here simply added. Other combinations are like an asymptotic model could be more appropriate if we consider that the two modes do not really coexist but one mode is dominant and the influence of the other one vanishes depending on the conditions.

Fujita et al. made an important work in falling film evaporation on horizontal tubes. They presented [FUJI94] an experimental and analytical study of R-11 flowing on horizontal $25mm$ O.D. plain tubes. Compared to the previous model, they have added a transition region between the developing and the developed one. Figure 2.6 shows the three regions around the tube. A model for laminar and turbulent liquid flow has been developed and showed good agreements with the measurements. However, the measured heat fluxes were low ($< 2500W/m^2$) and no boiling contribution was added. Their laminar/turbulent transition Reynolds number from their measurements or model were also surprisingly low, Re$\approx$ 200 compared to the common value of about Re$\approx$ 1500.

Fujita and Tsutsui [FUJI95] presented a more detailed analytical study of falling film evaporation. They showed primarily that the Nusselt theory for a vertical surface –$Nu = 1.1Re_L^{-1/3}$– applied on a plain tube gives:

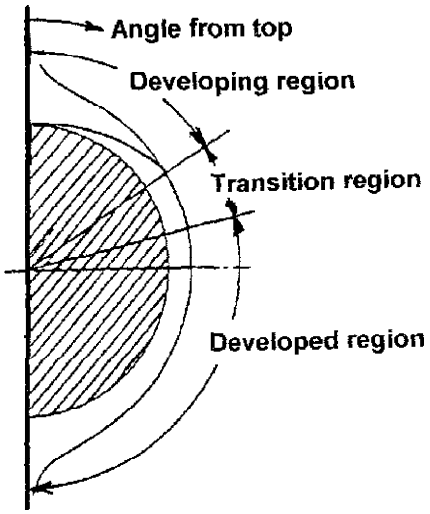

Figure 2.6: Fujita and Tsutsui [FUJI94] triple regions of the liquid flow around the tube.

$Nu = 0.906 Re_L^{-1/3}$ (18% lower) where this Nusselt number is a mean value on the tube. This method assumes that the thermal boundary layer is fully developed and the liquid flow is laminar flow. To take into account the development of the thermal boundary layer, they made a three-zone approach like above and presented equations to evaluate the Nusselt number for each region. This model is not presented here because it is applicable only for low heat fluxes (strictly non boiling conditions).

The Fujita group continued their falling film investigations [FUJI98] with triangular pitch bundle experiments (5 rows $\times$ 3 columns). The refrigerant was R-11 at $318K$ ($44°C$) flowing on $25mm$ O.D. plain tubes. Each row had at the top a different liquid feeder: a sintered porous tube, a tube with small holes in a row along its bottom and a plate with a row of holes at its centerline. The feeder had only a heat transfer influence on the top tube. The heat flux range was 500-15000 W/m^2 while the Reynolds numbers tested ranged from 10 to 2000. As their measurements were not influenced by the heat flux, they deduced that their heat flux was always below the onset of boiling. Their data were well predicted by the Lorenz and Yung correlation [LORE78]. For most of their data, the Nusselt number was decreasing versus Reynolds number in the laminar region ($Re < 200$). In the turbulent region ($200 < Re < 2000$), the Nusselt number was slightly increasing with Re. As mentioned before, their transition Reynolds number was quite low. They also observed lower heat transfer coefficients for the top tube and correlated

thus their measurements in two different equation, for the top tube:

$$Nu_L = \left(Re_L^{-2/3} + 0.008 Re_L^{0.3} Pr^{0.25}\right)^{1/2} \tag{2.31}$$

and for the other tubes

$$Nu_L = \left(Re_L^{-2/3} + 0.010 Re_L^{0.3} Pr^{0.25}\right)^{1/2} \tag{2.32}$$

Where the film Reynolds number is given by equation 2.21 and the Nusselt number by equation 2.13. The second equation is for the bundle and gives a mean value, the flow rate to be taken into account is the one at the top of the bundle. This model is valid until dry patches appear on the tube due to film breakdown. They presented an interesting reflection on the film breakdown that will be presented in the section 2.2.

Alhusseini [ALHU97] studied liquid falling film evaporation on a vertical plain tube with water and propylene glycol (Prandtl number up to 45) in non boiling conditions. To analyse their results, they split the liquid flow into two regions, laminar and turbulent. For the laminar region, they used the equation 2.16 from Chun and Seban and multiplied it by $Ga^{-0.0563}$ to take into account the wave influence through the surface tension σ, where Ga is the modified Gallileo number $= \rho_L \sigma^3 / \mu_L^4 g)$. For the turbulent region, they approximated the results of their numerical simulation. To cover the entire Reynolds number range, they combined their laminar/turbulent heat transfer coefficients in a five order asymptotic model. The resulting prediction was quite good and is applicable over a wide Prandtl number range.

Chen et al. [CHEN94] measured heat transfer coefficients on $19mm$ O.D. vertical plain and Turbo-B tubes with R-11. The heat flux range was 0.6 to $30kW/m^2$ while the film Reynolds number varied from 2500 to 7000 (turbulent region only). The results presented interesting characteristics. For the plain tube, the curve of the heat transfer coefficient as a function of the LMTD presented a hysteresis (heat transfer was logically better when decreasing the heat flux because of the activation of more nucleation sites) and a maximum value of $3000W/m^2K$ with a heat flux of $18kW7m^2$ was reached. The maximum value for the enhanced tube increased to $20000W/m^2K$ at $30kW7m^2$. The degree of enhancement of the Turbo-B was found to be similar to pool boiling conditions. For both tubes, the film Reynolds number was found to have no influence on heat transfer, which suggests that boiling is the predominant phenomenon. When increasing heat flux above the conditions of maximum heat transfer coefficient, dryout spots were visible on the tubes. Investigations of these dryout conditions have been made and are detailed in the following section.

Gross [GROS94] compared experiment results from nine different experimental studies on falling film evaporation of ethanol and R-113 inside a

closed thermosyphon (vertical plain tube). Figure 2.7 shows the heat transfer coefficients for R-113 as a function of heat flux. Three typical ranges were obtained:

a) for an increasing but small heat flux ($1500 < q < 4000W/m^2$), heat transfer coefficients decrease. They may be represented by a straight line (n=-1/3) which is consistent with the Nusselt theory where $q \sim \Gamma$.

b) a stepwise decrease of α around $q = 4000W/m^2$ indicating the apparition of the first bubble in the film.

c) for $q < 5000W/m^2$ heat transfer coefficients increase as indicated by the straight line (n=0.7) which represents the typical boiling behavior.

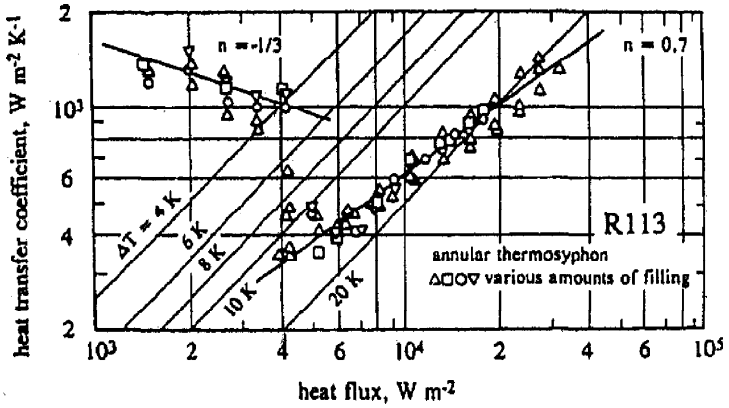

Figure 2.7: Gross [GROS94] identification of the heat transfer regimes.

At low Reynolds number ($Re < 100$), comparisons between the Nusselt solution and experiments showed that the Nusselt equation predictions for the heat transfer coefficient were up to two times larger than the measurements. The authors suspected this to be due to dry patch formation. An interesting discussion is given and is presented in the section 2.2. A model is presented and consists of the Nusselts equation multiplied by two corrective factors: one to take into account the tube diameter and one for the boiling influence ($= (q/q_{ONB})$). It is remarkable that his high heat flux method $\alpha \sim q^n$ with n=-1/3 (Nusselt) +1 (boiling factor) =0.66 which is close to the value of 0.7 found in figure 2.7. The author mentioned that for enhanced tubes, this exponent could be different.

2.2 Film breakdown

Gross [GROS94] listed the mechanisms and fluid forces involved in the dry patch evolution to be as follows:

a) *Liquid inertial forces.* The pressure induced by the liquid deceleration at the stagnation point favors rewetting of a dry patch;

b) *Surface tension forces.* The interfacial surface tension force tends to enlarge the size of a dry patch;

c) *Marangoni effect.* The surface tension gradient created by the temperature gradient acts to transport liquid away from the thin liquid layer and hence create a dry patch;

d) *Vapor inertial forces.* The vapor flow creates a suction force when going around the liquid which tends to increase the dry patch size;

e) *Interfacial shear stress.* The vapor tends to entrain the liquid leading edge (increase the dry patch in upward vapor conditions) and to equalize the liquid film thickness increasing the effective surface coverage.

El-Genk and Saber [ELGE01] made an interesting review of the film breakdown on vertical surface models without heat transfer. They all predict the minimum film thickness below which dry patch are stable. The main models are:

- Hartely and Murgatroyd [HART64] who made a force balance at the stagnation point with the assumption of a constant liquid velocity in the film and found $\Delta_{min} = (1 - \cos\beta)^{1/5}$ in which Δ_{min} is the non dimensional film thickness of the film $\Delta_{min} = \delta \left(\frac{\rho_L^3 g^2}{15 \mu_L^2 \sigma} \right)^{0.2}$;
- Hobler [HOBL64] based his model on the minimization of the total energy of a rivulet (liquid flow in between two dry patches) and the assumption of a circular rivulet and their minimum film thickness was 1.08 times the one from Hartely and Murgatroyd;
- Doniec [DONI91] improved the previous model by solving numerically the rivulet profile and the resulting minimum film thickness was 0.84 times the one from Hartely and Murgatroyd.

For those three models, the liquid flow rate corresponding to the minimum film thickness is derived from the Nusselt theory approximation and is defined by:

$$\Gamma_{min} = 1.693 \left(\frac{\rho_L \mu_L \sigma^3}{g} \right)^{0.2} \Delta_{min}^3 \tag{2.33}$$

Conversely, the velocity profile for the determination of the minimum film thickness is assumed constant. El-Genk and Saber improved that by a numerical simulation and the resulting model is, with the previous definitions:

$$\Delta_{min} = (1 - \cos\beta)^{0.22} \tag{2.34}$$

$$\Gamma_{min} = \left(\frac{\rho_L \mu_L \sigma^3}{g}\right)^{0.2} \left(0.67\Delta_{min}^{2.83} + 0.26\Delta_{min}^{9.51}\right) \tag{2.35}$$

The exponent of 0.22 found here is very close to the earlier value of 1/5 found by Hartely and Murgatroyd. The authors compared their predictions with existing data with water flowing on several surfaces showing an error of about ±20% on the minimum liquid flow rate. A schematic of the falling film breakdown is given in figure 2.8.

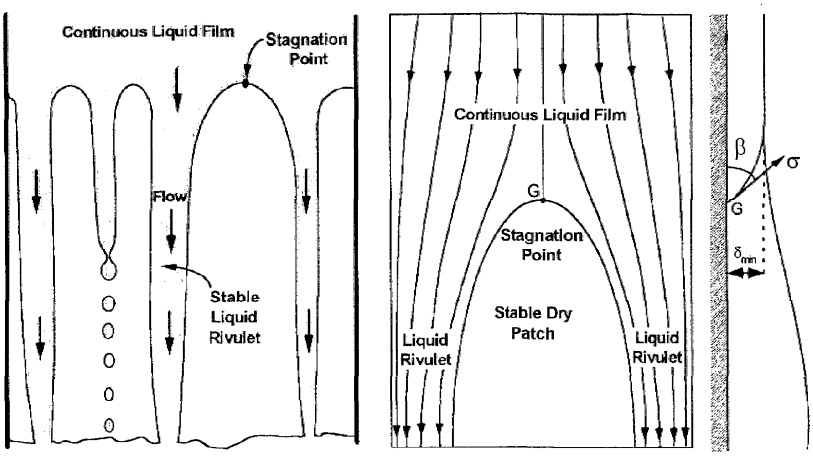

Figure 2.8: El-Genk and Saber [ELGE01] observed breakup of a liquid film (left) and showed a schematic of a stable dry patch (right).

Hsu et al. [HSU65] presented a detailed work on water falling film breakdown on a vertical tubes. They calculated the development length of the thermal and dynamic boundary layer. From this, they defined a wetting film thickness δ_{MWR} which is equivalent to the thermal boundary layer thickness. They explained that if the liquid film is thicker than δ_{MWR}, the thermal layer has not reached the free surface and surface temperature do not present variations. There is thus no thermocapillary effect. This criteria is independent of the heat flux. On the other hand, when the film becomes thick, turbulence tends to mix the liquid, appears close to the surface and the temperature is more uniform. The authors thus set a maximum for δ_{MWR}: $y+ = 26$. A stability criteria was also determined to predict the

necessary film thickness to rewet an existing dry patch. An interesting discussion about boiling in film and its impact on film breakdown is made. The bubbles can break the surface and thus favor the film breakdown but the agitation they create diminishes the temperature gradient and thus the thermocapillary effect. Transposing this model to horizontal tubes of the current study would lead to important difficulties and is not attenpted.

Chen et al. [CHEN94] in their falling film study of R-11 evaporation on a plain and a Turbo-B vertical tube noted a rapid drop of the heat transfer coefficient when increasing heat flux just following the maximum value. They observed the beginning of the film breakdown at this point. Figure 2.9 shows the result of their observations. Film breakdown heat flux is plotted versus the film Reynolds number at the exit of tube. The film breakdown occurred also at the bottom of the tube, the given Reynolds number is thus the local value of film breakdown. For the plain surface, the film breakdown limit increases with film Reynolds number. In other words, increasing flow rate on a plain surface allows higher heat fluxes to be sustained without film breakdown. In contrast, the film breakdown heat flux was constant for the Turbo-B surface, suggesting a heat flux limit above which there is film breakdown independent of the liquid flow rate. For high liquid flow rates, this limit defines maybe a maximum rate at which the reentrant cavities can be refilled with liquid to be evaporated. On the other hand, as the heat flux limit remains high for low liquid flow rates, this surface could be used advantageously to achieve complete evaporation of the overfeed liquid.

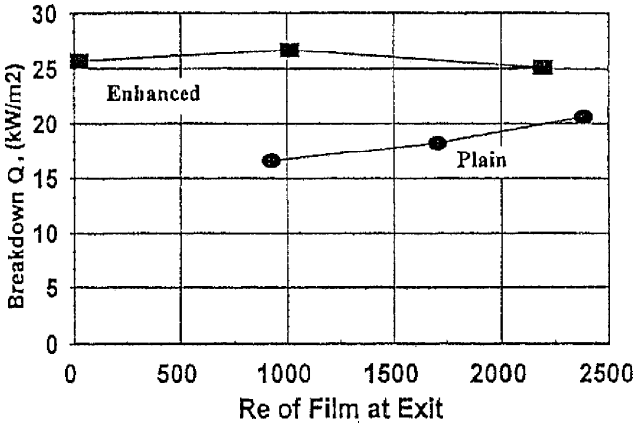

Figure 2.9: Chen et al. [CHEN94] film breakdown observation for the plain and the Turbo-B (enhanced) surfaces with R-11.

Fujita and Ueda [FUJI78] in their first work about falling film heat transfer used saturated water falling on the outside of a $16mm$ O.D. vertical plain

stainless steel tube. They measured heat transfer coefficients and presented interesting results about film breakdown. Figure 2.10 shows the liquid flow rate at the bottom of the test section plotted versus the liquid distributed at the top as a function of the heat flux on the surface (from an energy balance, the curves should be lines, they presented a curvature because of the entrained droplets). The solid circles represent conditions with intermittent dry patches while the squares correspond to permanent dry patches, the latter which are surprisingly only weakly a function of the heat flux. Similar to the figure 2.14, the film flow rate of intermittent dry patch formation seems to be a linear function of the heat flux.

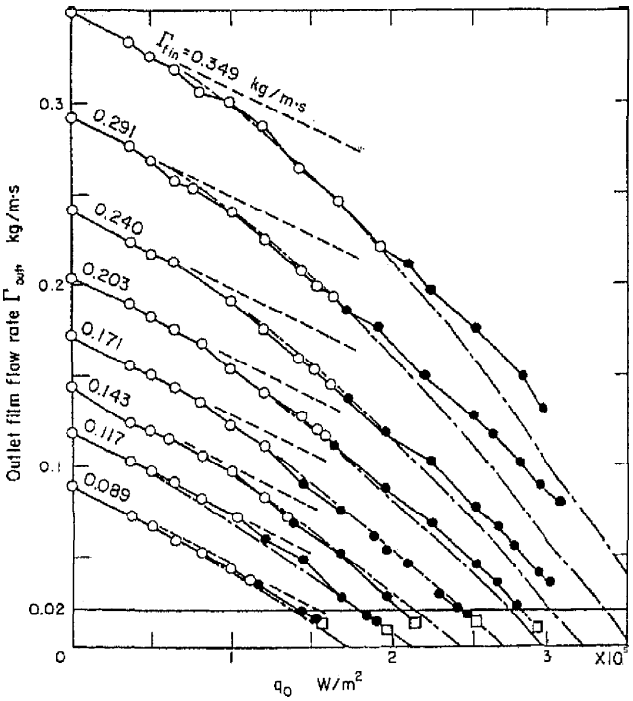

Figure 2.10: Fujita and Ueda [FUJI78] variation of outlet film flow rate with heat flux and formation of dry patches (○: no dry patches, •: intermittent dry patches and □: permanent dry patches).

In their study on falling film evaporation of R-11 on plain tubes, Fujita and Tsutsui [FUJI98] presented more work on falling film breakdown. Figure 2.11 is a representative drawing of the observed flow pattern on a row of $25mm$ O.D. tubes for two different heat fluxes and flow rates. From these type of photographs, they measured the fraction of wetted area. The result was that the wetted area fraction is decreased as a function of heat flux for a fixed flow rate and it also decreased with flow rate.

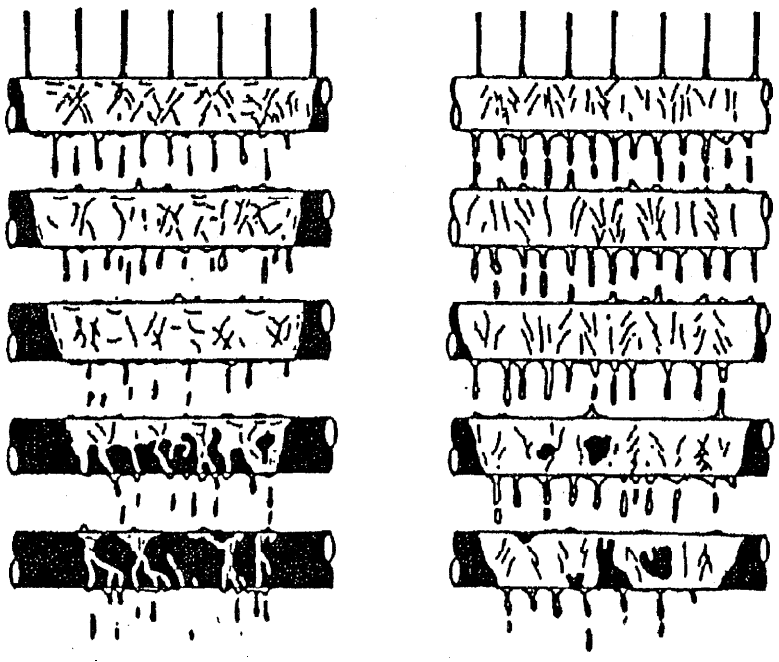

Figure 2.11: Fujita and Tsutsui [FUJI98] film breakdown observations, left: $Re = 100$ and $q = 4.9kW/m^2$, right: $Re = 250$ and $q = 9.8kW/m^2$.

The impact on the heat transfer coefficient was also pointed out and is presented in figure: 2.12. The measured Nusselt number divided by the one from their model (equations 2.31 and 2.32 is plotted as a function of the film Reynolds number. Most of the data are gathered on or around the horizontal line at unity and represent the fully wetted tube surface conditions. In contrast to the tube number 1, some data fall below the horizontal line for low Reynolds numbers, this is caused by dry areas on the tubes. The point where the data starts to fall is function of the liquid flow rate and the heat flux. They correlated this with the following film breakdown threshold equation

$$q_{dry} = 48Re_L \tag{2.36}$$

This equation is valid with Re up to 200 and heat fluxes up to $10kW/m^2$.

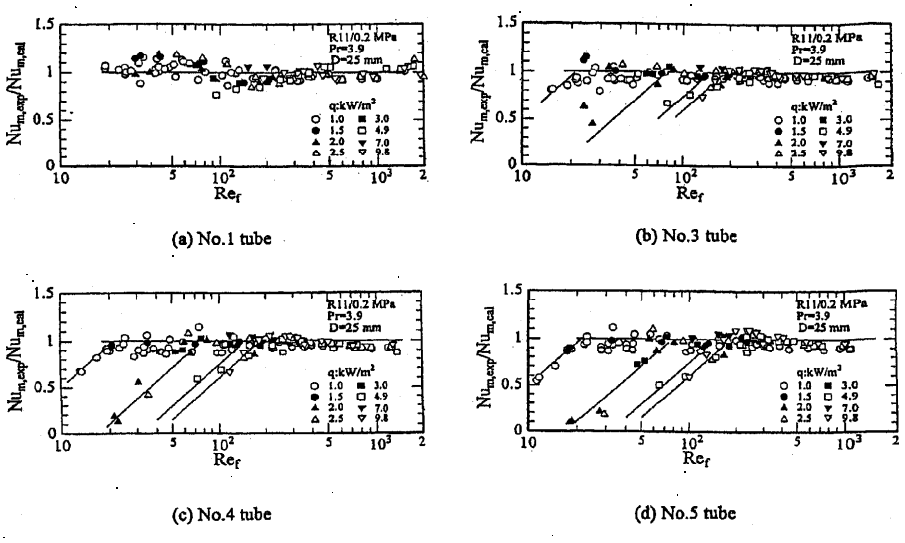

Figure 2.12: Fujita and Tsutsui [FUJI98] ratio of measured to predicted Nusselt number.

Ganic and Roppo [GANI80] started their work on falling film breakdown with heat transfer tests with subcooled water on a plain $12.7mm$ O.D. copper tube. They found that the film breakdown heat flux increased with liquid flow rate and tube spacing. The effect of water inlet temperature was on the other hand weak. Figure 2.13 shows the measured heat transfer coefficient at film breakdown as a function of film Reynolds number. These heat transfer coefficients seem to vary linearly versus the liquid flow rate.

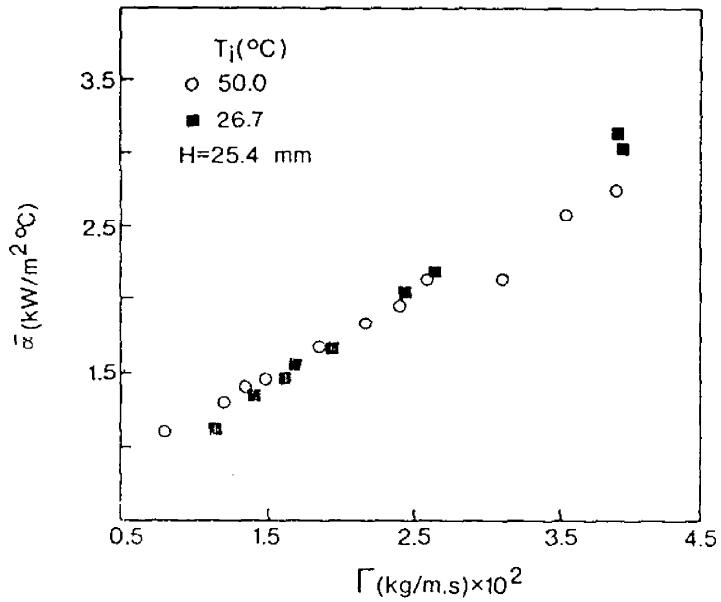

Figure 2.13: Ganic and Roppo [GANI80] results for heat transfer coefficient versus flow rate at two different inlet temperatures.

Ganic and Getachew [GANI86] next studied falling film breakdown on horizontal plain and porous coated tubes ($25,4mm$ O.D.) with ethyl alcohol and water. Based on their observations, they gave an explanation about dry patch formation: when a liquid flows on the tube surface, waves are presents. These waves create areas where the liquid film thickness is thinner. The thinner film favors higher local temperature and thus a lower surface tension. The pressure drop through the surface is thus lower at this position than at the wave crest and the liquid is pushed from the thinner liquid layer to the thicker one favoring dry patch formation. This is the Marangoni effect or thermocapillary effect. In addition with the porous coated tube only, bubbles were observed at this place that might perturb the thin film. Figure 2.14 presents their results for ethyl alcohol on plain and porous tubes. For one liquid flow rate on the tube, they reported two breakdown heat fluxes: one corresponds to first intermittent dry patch and the second corresponds to a permanent dry patch. Film breakdown occurs at higher heat fluxes for the porous coated tube than for the plain tube. The authors mentioned that the porosity of the surface helps the liquid to wet it and retards film breakdown. Ethyl alcohol was found to sustain higher heat fluxes than water on the plain tube while the opposite trend was observed on the porous tube.

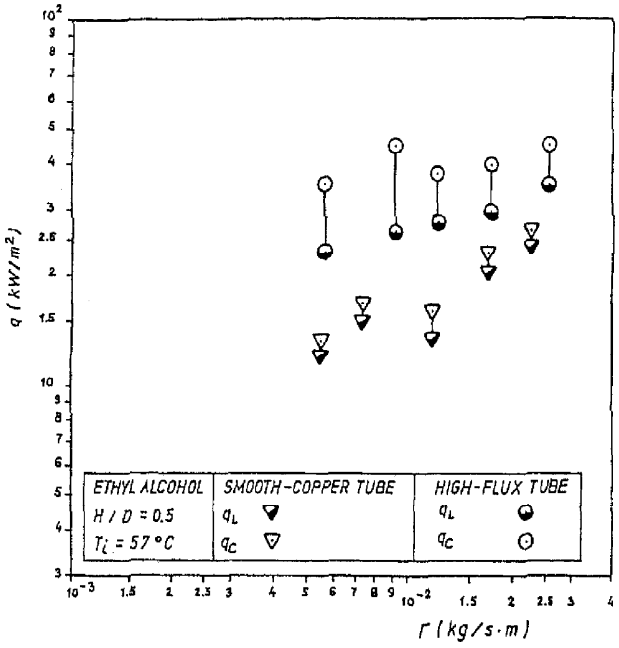

Figure 2.14: Ganic and Getachew [GANI86] film breakdown as a function of the liquid flow rate Γ with ethyl alcohol, H is the intertube distance, q_L and q_B onsets of intermittent and permanent dry patches.

Przulj and Ganic [PRZU91] extended this work to falling film breakdown on copper and stainless steel plain tubes with 25.4 and 12.7mm diameters. They compared their results with the dry patch model, the rivulet

model and small perturbation models [BAN78] and the differences were significant. They thus correlate their measurements in specific equations. Some interesting general trends of their work are: the mean film breakdown heat flux increases with flow rate and spacing between tubes (higher kinetic energy), water can sustain higher heat fluxes than ethyl alcohol and the liquid flow mode (droplets, column or sheet) has an effect on the film breakdown heat flux.

2.3 Conclusions

Recent important works on nucleate pool boiling have been reviewed. For the plain tube, several studies present specific correlations for the refrigerant R-134 (for example Webb and Pais [WEBB92] or Barthau and Hane [BART00]). General correlations including physical properties and surface roughness influences are also detailed. For the Turbo-BII HP, a correla-

tion from the results of Tatara and Payar [TATA00] is presented while for the Gewa-B and the High-Flux tubes, most of the available studies have been performed with other fluids but the results are presented in terms of enhancement factor compared to a plain tube and can thus be utilized to make comparisons later in chapter 6.

For falling film evaporation, measurements with R-134a are presented by Moeykens showing that the heat transfer coefficient is slightly higher than in pool boiling conditions for the plain tube. The tests were performed at relatively low flow rates and the eventual presence of dry patches was not clear in this work. Predictive methods are also reviewed but they are all based on measurements with different fluids compared to the current study (ammonia [ZENG95], water [CHUN71]). Generally, the performance in falling film conditions is better than in pool boiling conditions by a factor 1.5 to 2.

Finally, one model was found that predicts the film breakdown on a plain surface in adiabatic conditions ([ELGE01]). Under heat transfer conditions and with a plain tube, the film breakdown flow rate was observed to increase with the heat flux ([CHEN94]). The enhanced tubes were found to sustain a higher heat flux before film breakdown compared to a plain tube ([CHEN94], [GANI86]).

In summary, no general heat transfer prediction methods for plain nor enhanced tubes are currently available but several fluid specific methods are available, but they ignore any effect of partial dryout.

Chapter 3

Diabatic test facility description

In this chapter, the falling film heat transfer test facility built specifically for this project is described. A global presentation is first made, then the three different liquid circuits (refrigerant, water and ethylene-glycol) are detailed with their components. A focus on the test section follows. The computer controlled operation of the test facility is then described with a special focus on the instrumentation accuracy. Finally, characteristic dimensions and the operating test conditions are listed. The conception, design and construction of the test facility has been made together with Daniel Gstöhl. He is working in the Heat and Mass Transfer Laboratory of the Swiss Federal Institute of Technology on a falling film condensation project using the same test facility. For more information, refer to [GSTO04].

3.1 Global presentation

The goal of this test facility shown in figure 3.1 is to recreate the conditions of a horizontal falling film evaporator and provide the possibility to measure what we are mainly interested in: the external heat transfer coefficient on the individual tubes. This test facility is completely new, designed especially for this study. Its capabilities are: one vertical array of horizontal tubes of $19.05mm$ ($3/4inch$) O.D. (from six to ten tubes can be installed depending on the tube spacing). The length of the tested tubes is $554mm$. The external heat flux on the surface of the tubes can be varied from 10 to $80kW/m^2$ and the tubes are heated with water flowing inside. The test section also has six windows ($250 \times 120mm$) for visualization during falling film evaporation.

To avoid pump vibrations and simplify the construction, the test facility is divided in two units:

- The main unit with the test section, the auxiliary condenser and evaporator for the refrigerant conditioning.

- The auxiliary unit with the large pumps for conditioning the glycol for the condenser and the water for the test section.

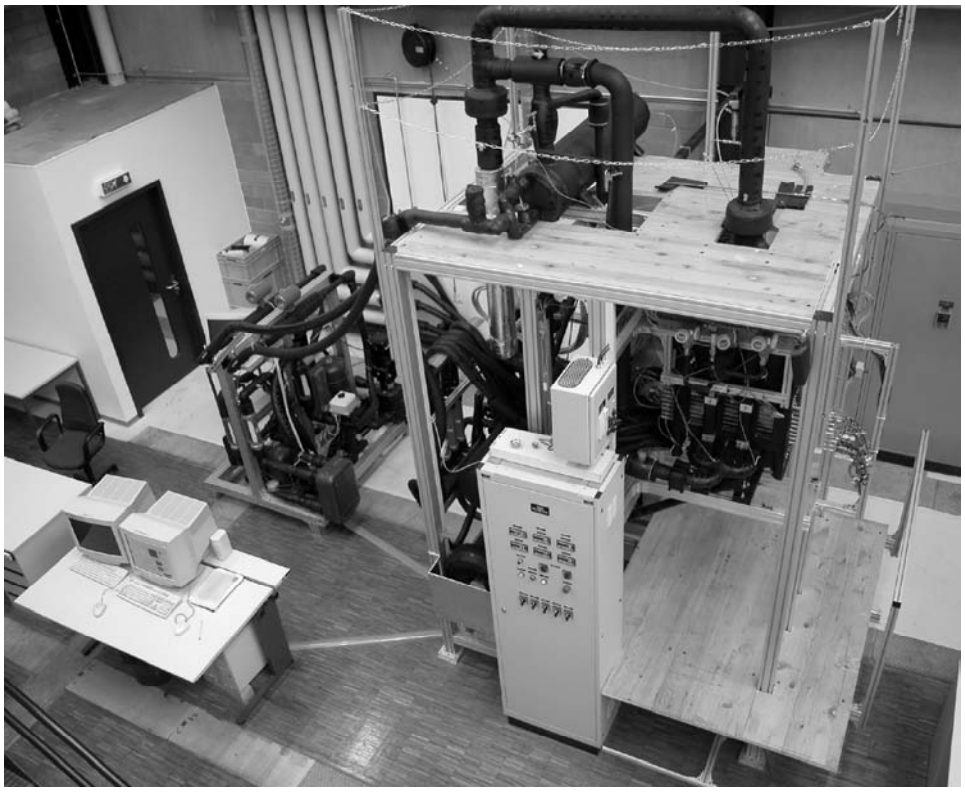

Figure 3.1: Overall view of the falling film test facility. Main unit on the right and auxiliary unit on the left.

3.2 Refrigerant circuit

This is the main circuit of the test facility. It globally comprises an electrically heated evaporator to maintain the desired saturation condition, a condenser to condense the vapor created in the test section and the test section itself. A schematic of this circuit is presented below in figure 3.2.

3.2.1 Liquid refrigerant circuit

During operating, most of the liquid is in the evaporator which acts as a liquid reserve in the circuit (all liquid tends to drain to the flooded evaporator). Starting the description from this flooded evaporator, the refrigerant flows through the filter and the subcooler to the magnetically driven gear pump

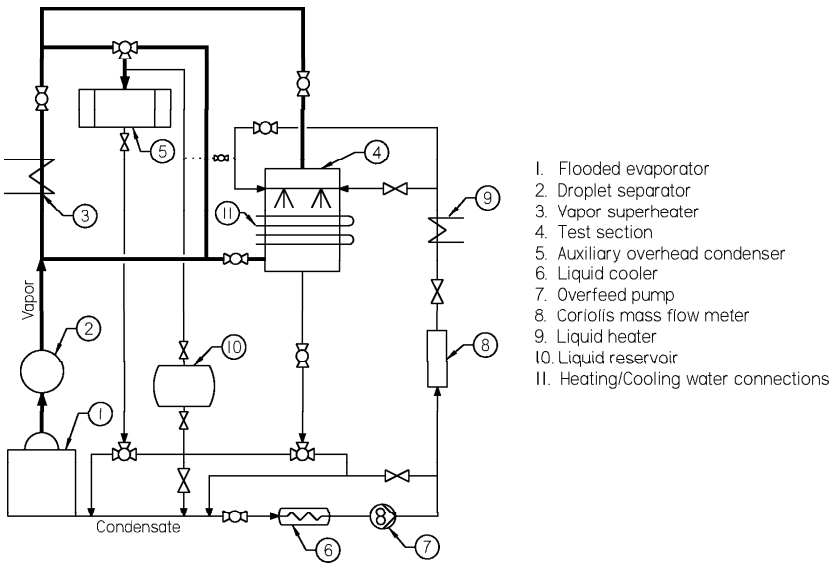

Figure 3.2: Refrigerant circuit

(self lubricating without oil). The filter removes eventual particles from the liquid refrigerant and contains also a refrigerant drying cartridge. The subcooler is a heat exchanger connected to an external thermal temperature controlled bath. It is thus possible to control the subcooling of the liquid refrigerant before the pump to avoid cavitation. Typical values of the liquid subcooling before the pump are 2-3K. Parallel to the pump, bypass piping together with a frequency controller are also installed to achieve the desired liquid flow rate. For very low flow rates, the bypass is opened rather than going to very small frequencies with the gear pump, which would give an oscillating flow rate. There is then a vibration absorber, a coriolis mass flow meter and an electric heater to come back close to the saturation conditions at the test section inlet. At this point, the liquid enters the test section and has to be distributed uniformly on the heated tubes. Special care has been taken to achieve this distribution and the liquid distributor detailed below has been used. Once the liquid leaves the distributor, it falls on the top of the heated tubes. It is here partially evaporated and the residual liquid leaves the test section by gravity. This flow could – by means of a three way valve – be oriented to the auxiliary reservoir or back to the flooded evaporator. At the exit of the auxiliary condenser, the refrigerant is also liquid and has the two same possible destinations.

3.2.2 Liquid distributor

The distributor is a rectangular box inserted in the test section above the tested tubes. Its external dimensions are $554 \times 200 \times 20\text{mm}(W \times H \times D)$. The liquid refrigerant enters from each side at the top and is pre-distributed with an stainless steal pipe ($13mm$ I.D.) in which there are holes oriented upwards ($3mm$ in diameter and $5mm$ center to center). Then the liquid flows through two layers of foam. A first $150mm$ high layer is Polyurethane foam (pore diameter:$200\mu m$). There is then a second $10mm$ high layer of Polyethylene foam (porosity:37%, pore diameter:$35\mu m$). This last layer is more compact and creates a larger pressure drop to force a good lateral liquid repartition in the distributor. After this porous section, the liquid reaches the bottom of the distributor, which is a removable machined brass piece with 268 holes; of $1.5mm$ diameter with a distance center to center of $2mm$. The liquid distribution width is $550mm$. Figure 3.3 shows a schematic of the distributor while figure 3.4 shows a photograph of it.

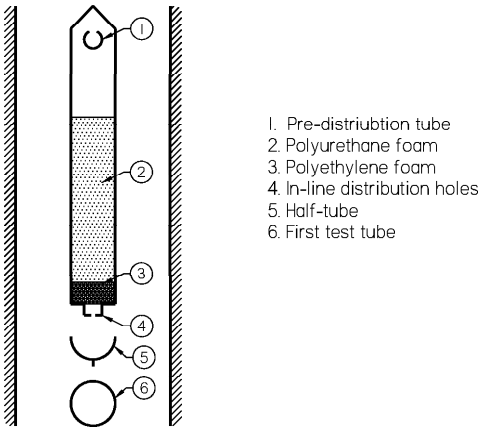

Figure 3.3: Schematic lateral view of the distributor

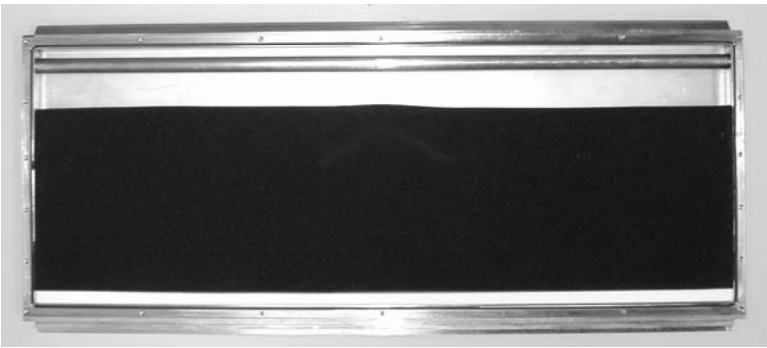

Figure 3.4: Front view of the distributor $550 \times 200mm$ (W $\times$ H)

3.2.3 Vapor refrigerant circuit

The circuit of the vapor refrigerant is a natural circulation loop. The vapor is evaporated in the lower part of the circuit and condensate is formed in the upper parts. The liquid flows back from the auxiliary condenser to the flooded evaporator by gravity. A height of $2m$ between those two elements insures a maximum driving pressure difference of about $25kPa$ with refrigerant R-134a at 278K. The test facility offers three different possibilities for the vapor circuit:

Downward vapor overfeed. In this mode, the three upper vapor pipes of the test section are connected to the flooded evaporator and the four lower ones to the auxiliary condenser. The vapor in the test section thus flows in a downward direction. If the power of the auxiliary condenser is adjusted to compensate the evaporation in the test section, the power of the flooded evaporator is very small and the system operates without vapor overfeed. The vapor flow is only due to the evaporation in the test section. If the power of the auxiliary condenser is increased, the flooded evaporator will automatically follow the same trend to maintain the saturation conditions and the system will then operate in a vapor overfeed condition. It is possible to choose the vapor overfeed flow rate by setting the power of the auxiliary condenser.

Upward vapor overfeed. By changing the vapor valve positions, the above described situation can be inverted: The three upper vapor pipes of the test section are connected to the auxiliary condenser and the four lower ones to the flooded evaporator. Similar to above, it is possible to operate with or without vapor overfeed but the flow direction has changed.

All exits in the test section opened. The test facility offers this third possibility. In this mode, the vapor can enter or exit through every vapor pipe of the test section. The auxiliary condenser and the auxiliary evaporator are connected together before the test section. From this con-

necting point, one pipe goes to the top of the test section (the three upper pipes) and one goes to the bottom (the four lower pipes). The vapor created in the test section can leave through any exit. In this mode, it is not possible to create a vapor overfeed flow. This mode has been chosen to be used for this study because in this mode, the vapor is not forced and leaves the test section very slowly. This created test conditions that are the desired ones: no or very little vapor shear effect.

3.3 Water circuit

Water is conditioned in its auxiliary unit and cooled in the test section in the test copper tubes. The water circuit is illustrated in figure 3.5.

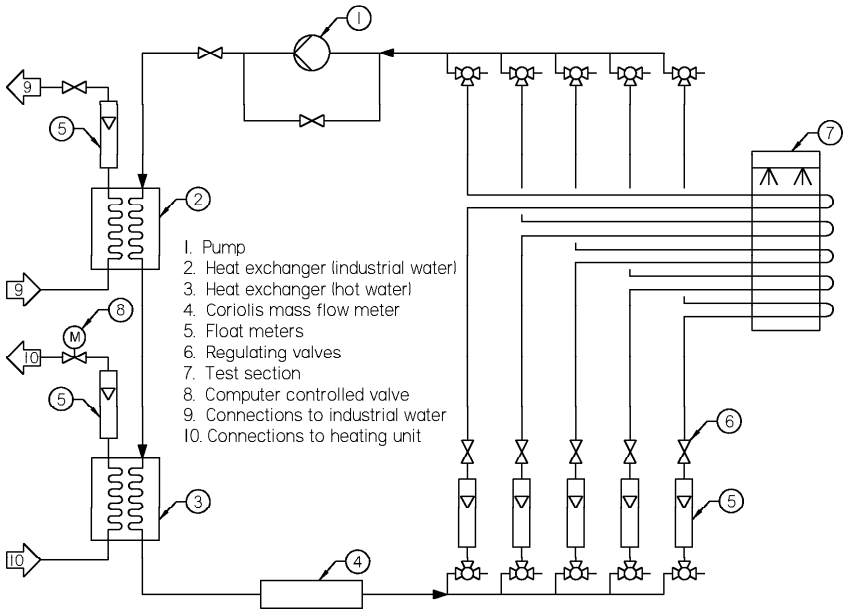

Figure 3.5: Water circuit

The circuit starts with the centrifugal pump. An electronic speed controller together with a bypass affords a good precision in the mass flow adjustment. The water then goes into the first liquid-liquid heat exchanger. In this heat exchanger, the test section water can exchange heat with industrial water (water from Lake Geneva available in the laboratory at a constant temperature of $280K/7°C$). This first step in the water conditioning brings the temperature of the water from the test section back to

a constant and stable value independent of the operating conditions in the test section. The test section water flows then through a second liquid-liquid heat exchanger where it is heated with hot water from a network (a gas-fired hot water heater which provides hot water with adjustable temperature from $323K/50°C$ to $363K/90°$C with a maximum capacity of $160kW$). The heat exchanged in this heat exchanger is linked to the flow rate of the hot water. A computer controlled valve sets this flow rate based on the test section water temperature at the outlet of the heat exchanger. The water temperature at the test section inlet is thus automatically maintained constant when the flow rate is changed or if there are any small oscillations in the network hot water temperature. At this point, the water for the test section is well conditioned in terms of stability of its temperature and flow rate. The total mass flow rate is then measured with a Coriolis mass flow meter.

The main flow of water is then split to the sub-circuits of the test section. Each sub-circuit has is own float flow meter and valve to control its flow rate and thus set the water distribution uniformly between the sub-circuits. The goal is to have the same flow rate in all sub-circuits. There are five sub-circuits and each one can be included in the main circuit (or not) with two three-way valves for each. A sub-circuit usually has two tube passes, i.e. water goes in a copper tube in one direction (right to left) and comes back through the copper tube just above in the opposite direction. With this setup, the water temperature profiles in the two tubes are opposed. The quantity of liquid refrigerant evaporated after each two tubes in the test array is thus nearly uniform along the tube length (a one-pass circuit design used in many previous bundle tests tend to create a liquid maldistribution along the tube axis, which should be avoided). After the test section, the water flows from the sub-circuits, merge and goes back to the pump to complete the circuit.

3.4 Glycol circuit

The glycol circuit is depicted in figure 3.6.

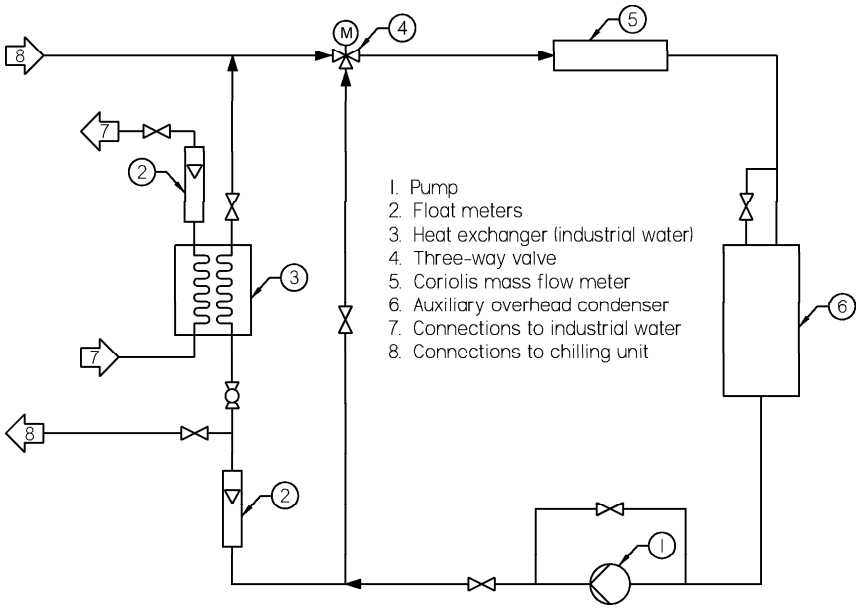

Figure 3.6: Glycol circuit

Glycol is used as a cold source for the auxiliary condenser of the test facility. It is provided by a network installation (at $253K / -20°C$ and a maximum continuous cooling capacity of $80kW$) available in the laboratory. This network installation has already a system to insure the glycol circulation but a pump has been added in the test facility to increase flow rate and the cooling capacity in the auxiliary condenser. The glycol from the network installation passes first through an electrically controlled three-way valve where the mass flow is adjusted with a computer (the valve is a three-way one to allow glycol recirculation in the case of low capacity requirement). The mass flow is then measured by a Coriolis flow meter. The liquid reaches next the auxiliary condenser. It is a three pass condenser with a design capacity of $50kW$. It is possible to use only one half of the tubes in the condenser to have a good power adjustment accuracy over a wide operating range. The glycol goes then to the pump (with a bypass connection). At this point, there are two possibilities: the recirculation valve is closed and all the liquid goes back to the network installation (the three-

way valve acts in this case as a one way valve) or the recirculation valve is open and part of the glycol is recirculated through the three-way valve to have a lower temperature difference at the inlet of the auxiliary condenser. In fact, the condenser capacity adjustment is simpler for low cooling loads when the inlet temperature difference is lower and the mass flow is larger. Most of the time during measurements, the recirculation valve is closed and the three-way valve regulates the glycol flow rate.

3.5 Test section

The test section is a rectangular stainless steel vessel illustrated in figure 3.7. Its internal dimensions are $554 \times 650 \times 69mm$ ($W \times H \times D$).

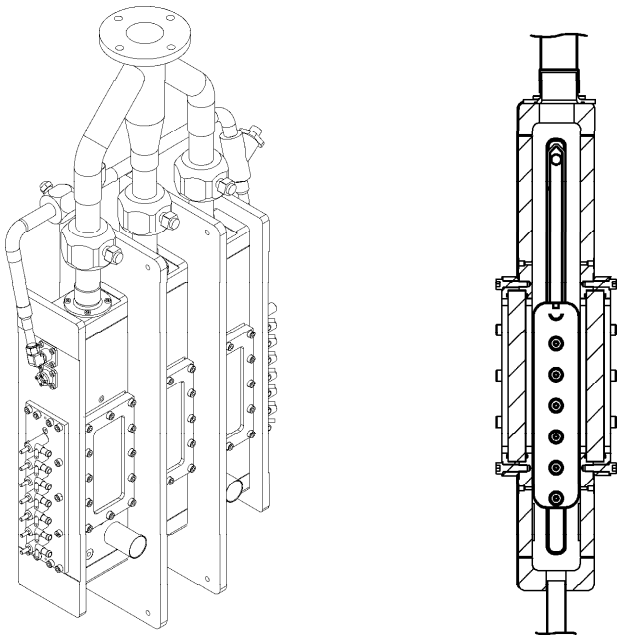

Figure 3.7: Test section.

In the present investigation the heat transfer coefficient during falling film evaporation on the outside of horizontal tubes is measured. The tubes tested have a nominal outer diameter of $19.05mm$ (3/4 in.) and are arranged in a vertical array. The end plates which hold the tubes on the left and on the right are removable. This allows the set of end plates to be changed to obtain different distances between the tubes. The length of the tubes tested is $554mm$. In order to have full visual access to observe the flow on the tubes the test section is equipped with six large windows. Three windows

are situated on the front of the test section and three opposed on the rear. The windows measure $120mm$ in width and $250mm$ in height. The liquid refrigerant enters the test section by two inlets; one inlet is located on the left and one on the right. Both inlets are equipped with hand valves to adjust the distribution between left and right. The liquid falling on the tubes is partially evaporated. The generated vapor leaves test section through three outlets at the top and four outlets in the lower part. The liquid refrigerant from the distributor which is not evaporated on the tubes leaves the test section by a outlet on the bottom. The tubes tested are described in detail below.

3.5.1 Copper tubes tested

Four commercially available tubes were tested: a plain tube and two mechanically enhanced boiling tubes (Turbo-BII HP and Gewa-B) and a porous coated tube (High-Flux). The plain tube and the Turbo-BII HP tube were provided by Wolverine Tube Inc, the Gewa-B tube was provided by Wieland-Werke AG and the High Flux tube by UOP Inc. All tubes were made from copper. Close-up pictures of the external tube surfaces are given in figure 3.8.

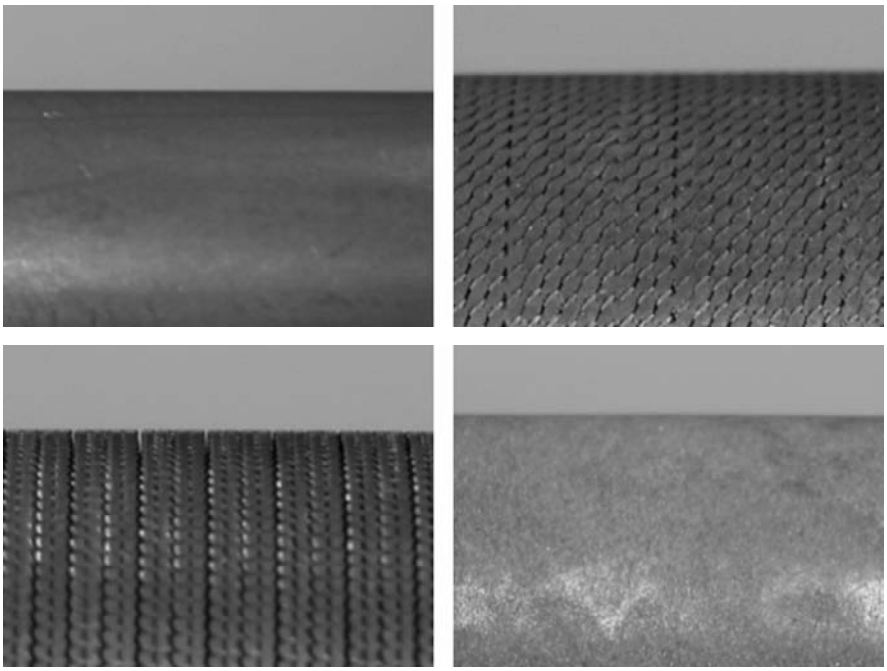

Figure 3.8: Close-up pictures of the surface of the four types of tubes: Plain tube (on the top left), Turbo-BII HP tube (on the top right), Gewa-B tube (on bottom left), and High-Flux tube (on the bottom right).

Photomicrographs of an axial cut of the four types of tubes tested are shown in figure 3.9.

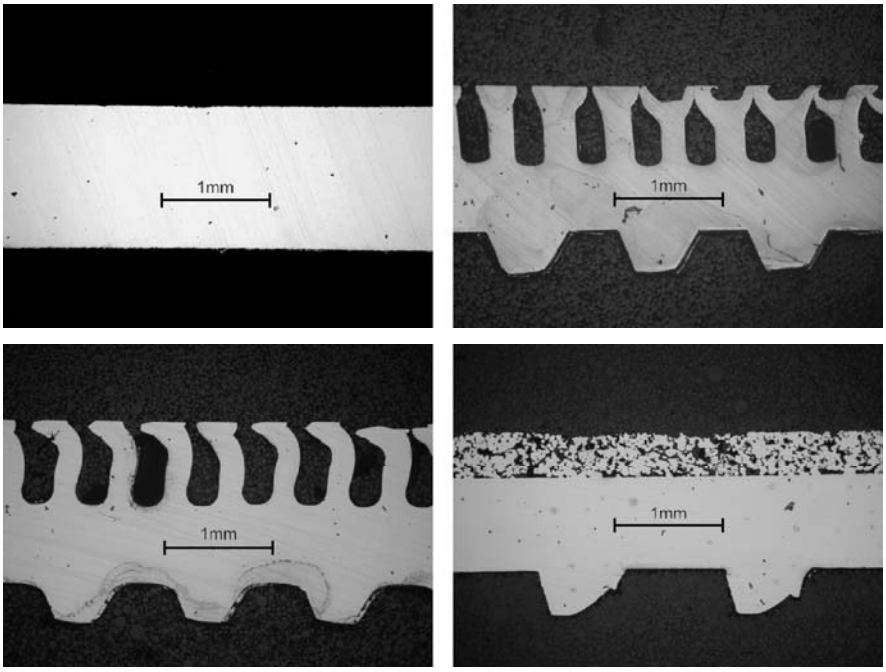

Figure 3.9: Photomicrographs of an axial cut of the tubes tested: Plain tube (on the top left), Turbo-BII HP tube (on the top right), Gewa-B tube (on bottom left), and High-Flux tube (on the bottom right).

A schematic of an externally and internally enhanced tube is depicted in figure 3.10 to illustrate the used definition of the external diameter D_o, the root diameter D_{or}, and the internal D_i.

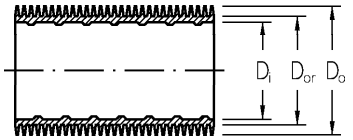

Figure 3.10: Schematic of externally and internally enhanced tube.

The tube diameter at the fin tip was measured with a micrometer. The root diameter of the tube was determined by a measurement with a microm-

eter after machining off the fins. The internal diameter was determined in the same way than the root diameter. The fin pitches of the Turbo-BII HP tube and the Gewa-B tube were measured on the photomicrographs. The results of these measurements are given in table 3.1.

Tube	D_o	D_{or}	D_i	fin pitch
Plain Tube	18.91	-	16.22	-
Turbo-BII HP	18.84	17.41	16.12	0.53
Gewa-B	18.84	17.38	15.97	0.55
High-Flux	18.87	18.05	16.67	-

Table 3.1: Geometrical specifications of the tubes tested. All dimensions are in mm.

3.5.2 Tube instrumentation

A new type of heat transfer measurement strategy has been developed in order to obtain local values of the heat transfer coefficient on each tube in the array. In previous published studies, only the inlet and outlet temperatures of the water have been measured. With that type of measurement, only a mean heat transfer coefficient for each tube can be obtained. In this study, a stainless steel tube with an external diameter of $8mm$ is inserted inside each copper tube. This tube is instrumented with six thermocouples. A schematic of this instrumentation setup is depicted in figure 3.11.

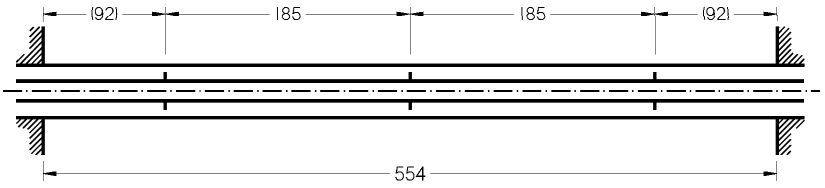

Figure 3.11: Schematic of the instrumentation setup of the tube to measure the temperature profile of the water flowing inside.

The thermocouples are located at three positions in axial direction of the tube. At every location, one thermocouple is facing upwards and one is facing downwards to measure the temperature of the water flowing in the annulus between the stainless steel tube and the tested tubes. The thermocouple heads are all brought out at one end on the inside of the tube. The distance between the thermocouples is $185mm$ and the distance to the

wall approximately $92mm$. The distance to the wall assures that no entrance effects are measured. The thermocouples are $0.5mm$ in diameter and have a length of 400 to $750mm$.

In addition, the stainless tube helps to increase the water side coefficient as flow area for the water is reduced. For an accurate measurement of the water temperature, a copper wire with a rectangular cross section has been wound helically around the stainless steel tube (not shown). The cross section dimensions of this copper wire are $0.9 \times 2.8mm$ (H $\times$ W) and it has been wound with a step a $12mm$. This promotes mixing and a further increase of the waterside heat transfer coefficient. The temperature difference between two thermocouples at one location was reduced with this enhancement. During the measurements, this difference was typically lower than $0.06K$ (thermocouples were re-calibrated in the case of larger difference). This method of inserting turbulators in the water flow channel has been widely used in evaporation when the tubes are heated with water (for example in [MOEY95b] spring type turbulators are used). It has also been applied successfully for ammonia flow boiling evaporation in the Laboratory for Industrial Energy System here at the Swiss Federal Institute of Technology.

3.5.3 Instrumentation of the test section

The vapor pressure in the test section is measured with two absolute pressure transducers. One is connected to the test section above the array of tubes and one below. The vapor temperature above the tubes is measured with six thermocouples. Three are situated on the front and three on the rear of the test section. They are $1mm$ in diameter and the junction is located in the middle between the test section wall and the distributor. The temperature of the liquid entering the test section is measured with one thermocouple inserted in each inlet. Below the array of tubes, three thermocouples $2mm$ in diameter are installed on the front of the test section. The junctions of these thermocouples are situated in the middle between the front and rear side. The temperature of the vapor leaving the test section is measured with one thermocouple in the vapor pipe on the front after the two vapor outlets on the front joined and one at the same position on the rear. The temperature of the liquid leaving the test section is measured with a thermocouple inserted in the liquid outlet. The wall temperature of the test section is measured with one thermocouple attached on the outside.

3.6 Data acquisition and control

3.6.1 Data acquisition system

All the measurements are made with the separate data acquisition computer. The acquisition system is a National Instruments SCXI. The acquisition card is a PCI MIO 16XE 50 installed in the PC. The resolution of this card is 16 bits and the maximum acquisition frequency on a single channel is $10kHz$. A SCXI 1000 module with four bays is connected to this card. For the acquisition computer, each of the four bays has a 32 channel voltage measurement card (type 1102). The total number of acquisition channels is thus 128. Each channel of this system has a computer programmable gain: 1 for 0 to $10V$ signal (pressure transducer and mass flow meter) and 100 for low voltage signals (thermocouples). The signals can be adjusted to the 0 to $10V$ range of the acquisition card in the computer. A $2Hz$ low pass frequency filter is also included in the card for each channel.

This helps diminish the measurement noise and does not affect the steady-state measurements of this study. At the end of the acquisition chain, a terminal block with 32 sockets is connected to the 1102 card. Each card has its own terminal block. The cold junction for every thermocouple is made in this terminal block at the socket. The material of this socket is copper for both poles (+ and -), the continuity of the two different specific materials of the thermocouple is so broken at this point located inside the terminal block. The temperature of the 32 cold junctions is maintained uniform with a metallic plate and is measured by the system via a RTD installed in the middle. Additionally, all the terminal blocks are placed in a closed cupboard away from external thermal influences.

The acquisition frequency of the system is high, it is so possible to make a first average during the acquisition. To measure a test parameter in a channel, 100 acquisitions are made in $0.02s$ – the $50Hz$ electric network period – and the average of these 100 values is calculated. The result is the measured value of this channel. By this way, the noise from the network alternative current on the measured signal is partially removed. This value is stored and the system goes to the next channel. With this measurement method, the theoretical channel measurement frequency is 50 $channels/s$, but due to the switching time between channels, this frequency is 30 $channels/s$. The time to measure all the channels of the acquisition computer is thus $4.3s$. To obtain one data point, 30 such acquisition cycles are taken and averaged.

3.6.2 Control system

A second computer is used to control the test facility. It has the same SCXI system as the data acquisition computer. The four bays of the SCXI 1000 module contain two cards for voltage measurement, one card for current measurement and one card with eight output channels. These outputs are

used to control the three-way valve for the glycol, the valve for the hot water, the two electric heaters in the flooded evaporator, the heater for the liquid refrigerant and the heater for the vapor refrigerant. Two PID controllers are programmed on this computer: One for the electric heater of the flooded evaporator (the saturation pressure in the test facility is maintained automatically constant) and one for the hot water valve (the flow rate of hot water in the heat exchanger is controlled based on the temperature of the water entering the copper pipes).

All the parameters are displayed online on the screens of the two computers and experimental parameters are calculated, for example: water temperature profile in the copper tubes, heat transfer coefficient on the measurement computer or PID status, various heating and cooling capacities on the control computer, etc.

3.7 Operating procedures

The operating procedures determine the way the test facility is utilized to get the measurements of all the desired parameters (pressure, temperature, flow rate ...) for every point of the test matrix array. The most important thing is to obtain stable conditions during the data acquisition period. First of all, the chosen tubes are mounted with the chosen spacing (one variable of the test matrix). The condenser is then started at a fixed capacity with a constant glycol flow rate. The pressure together with the temperature decrease in the test facility. To compensate, the electric heaters in the evaporator are started with the controller based on the pressure. The saturation conditions are automatically attained and maintained constant at the desired value. This regulation mode has been chosen because it is easier and faster to change electric power in the evaporator than the glycol flow rate or temperature in the condenser. By using a solid state relay (Triac) for the electric command, the response between the command voltage and output power is more or less linear over the complete range. The flow of water in the copper tubes is then started. The second controller maintains this water temperature at a given set point. The temperature difference between this water and the refrigerant influences strongly the heat flux q. The water flow rate in the copper tubes determines the water Reynolds number and thus the value of the internal heat transfer coefficient α_i. It is best to keep the internal heat transfer coefficient (or the water flow rate) as high as possible. The uncertainty in the determination of the external heat transfer coefficient is smaller with a higher value of α_i. On the other hand, a higher water flow rate means, for a given thermal duty, a smaller temperature difference between inlet and outlet. This creates a larger uncertainty on the energy balance. For every case, a compromise between these two opposite tendencies is necessary. The data acquisition subroutine is written to perform a

propagation of error analysis for each test condition (online) so an optimum can be imposed.

As a last step, the refrigerant pump is started and its flow rate set. Evaporation starts on the tubes. Based on the quantity of refrigerant vapor produced, it may be necessary to increase the condenser capacity to maintain the equilibrium between the auxiliary condenser and the flooded evaporator. After a stabilization period, the acquisition can be done. The computerized regulation on the pressure is accurate and the resolution on the electric power is fine. This regulation is maintained turned on during acquisition. On the other hand, the computerized regulation on the water flow into test section introduces some steps in its temperature. This regulation is only used to reach a given set-point but is turned off during acquisition ($\simeq 2min$). During this time, the temperature shift in the network water is very small and its affect on the induced temperature glide in test section water is negligible.

3.8 Instrumentation accuracy

Errors in measurements have mainly two origins. Errors directly from the measurement devices: error of a pressure transducer, thermocouple deviation... And errors due to oscillations of the measurement conditions, such as temperature variation of the glycol/hot water during an acquisition. These two points are discussed below. Another aspect with respect to errors is the statistical propagation in the calculations of the desired variables such as the heat transfer coefficient. This will be treated later in chapter 6 where the complete analysis of errors is estimated.

3.8.1 Thermocouples

The measured temperatures are around $278K$ ($5°C$) for the refrigerant and between $278K$ ($5°C$) and $295K(15°C)$ for the water in the copper tubes. Thermocouples type K are used because they offer a good precision in this range. The working principle of a thermocouple is based on the Seebeck effect. When two wires made of two different metallic materials are welded together at each end, a voltage appears if the two welded ends (or junctions) are at different temperatures. This voltage can be correlated to the temperature difference between the two ends. Measuring the temperature with a thermocouple consists of measuring the temperature of one junction (called cold junction) and the voltage that appears. With these two values, the temperature of the other junction (measurement point of the thermocouple) can be calculated.

In our case, the system measures the temperature of the cold junction and the voltage. It calculates the temperature of the thermocouple with standard polynomials of the K type thermocouples. This is the default function of the system.

To improve accuracy, a calibration is made. A calibration procedure consists of immersing the thermocouples in a thermal bath at one temperature and measuring the temperature of this thermal bath with a reference thermometer, changing the temperature step by step to cover the desired range. The results are compiled to find an individual correlation between the temperatures measured by the specific thermocouple and the reference thermometer connected in the same circuit as it will be used in the experiments. The calibrations are made versus a precision platinum RTD thermometer (Omega DP251). The calibration range is from $276K$ ($3°C$) to 306K($33°C$) for water temperature and from $263K$ ($-10°C$) to K $323K$ ($50°C$) for refrigerant temperature. The temperature step is $3K$ and the calibration is made upward and then downward to average hysteresis effects. Between calibration and measurement, all the acquisition system is maintained turned on all the time and the connections are never unplugged. The most important thermocouples are the ones inside the copper tubes for the water. These ones are calibrated after their mounting in the stainless steel internal pipe where they are tin soldered. They protruded out through holes into the water flow. A new calibration is also made while changing the type of tube to be tested or the intertube spacing. These thermocouples are thus calibrated once every month to obtain optimum accuracy.

The result of this careful calibration is a maximum deviation of $\pm 0.03K$ between the reference thermometer and the temperature from the thermocouple. As an example of their relative accuracies, the isothermal temperatures for a two-pass sequence of the water-side thermocouples are shown in figure 3.12. The agreement is here within $\pm 0.02K$.

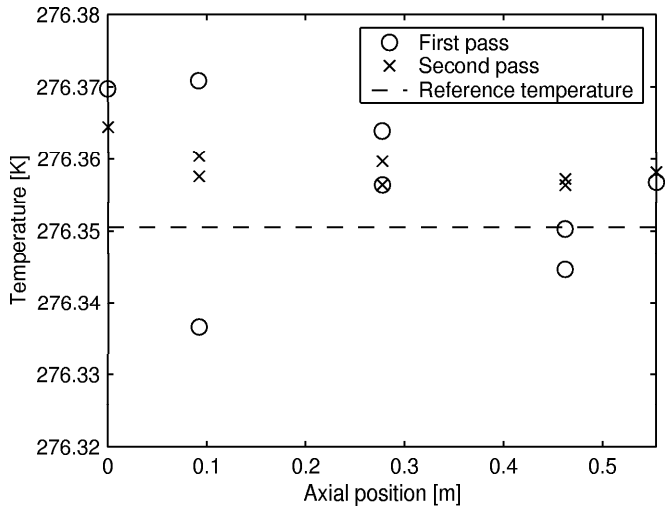

Figure 3.12: Temperature measured after calibration and compared to the reference thermometer at isothermal conditions.

3.8.2 Pressure transducers

All the pressure transducers used are electronic and based on membrane deformation measurement. The operating range of the transducers is 0 to $1000kPa$, except for the transducer at the outlet of the evaporator, which is also used for security purpose that has a range of 0 to $2000kPa$. They are class 1, 2, and 4 devices. The most critical for the measurements are the two transducers connected to the test section, which are class 1 devices. They have an accuracy of 0.1% of full scale, which corresponds to an absolute error of $1kPa$. Once again, the transducers are calibrated in the laboratory for a better accuracy. The reference (known) pressure was made by a calibrator balance. The calibration ranges are 100 to $1000kPa$ and 100 to $1600kPa$, respectively, with a step of $100kPa$. The deviation after calibration is always smaller than the specified absolute error.

In addition to the transducers mentioned above there is one pressure transducer, connected to the test section with a small operating range from 0 to $10kPa$. This transducer is used only when the air is pumped out of the test section to measure the pressure of the remaining gas.

3.8.3 Mass flow meters

There are three mass flow meters on the test facility, two with an operating range from 0 to $1.666kg/s$ in the water and glycol circuits and one with range 0 to $0.166kg/s$ in the refrigerant circuit. They are all Coriolis type and measure directly the mass flow rate in kg/s. The uncertainty of their measured mass flow rates is given by the following equation:

$$\Delta\dot{m}/\dot{m} \leqslant \pm(0.15 + S/\dot{m})\% \tag{3.1}$$

where $\dot{m}$ is the measured mass flow rate and S a constant that depends on the mass flow meter. The values are $S = 8.3 \cdot 10^{-3} kg/s$ for the large mass flow meters and $S = 8.3 \cdot 10^{-4} kg/s$ for the small one. Hence, the errors on water and glycol flowrate measurements are smaller than 0.18% while the error on refrigerant flowrate measurement is smaller than 0.17%.

3.9 Conclusions

A new test facility constructed specifically for the current study was described. It comprises mainly three circuits: a refrigerant circuit with a natural circulation loop for the vapor while the liquid circulation is insured by a gear pump, a water circuit in which the temperature and the flow rate are accurately set before utilization as a heat source for the refrigerant evaporation and a glycol circuit for the auxiliary condenser. In the refrigerant circuit, the saturation pressure is maintained constant by a regulated electric

flooded evaporator. Tests are performed at 3.5 *bar* (5°). An overhead auxiliary condenser is installed at the top of the circuit to condense the vapor generated in the test section and in the flooded evaporator. The test section is a rectangular pressure vessel with a vertical array of ten horizontal tubes. Six large windows allow complete flow visualizations on and in-between the tubes. The tubes have a length of $554mm$ and a diameter of $19.05mm$ and they are held by tube sheets that can be changed for different tube pitch measurements. The test section is equipped with an elaborated distribution system of liquid refrigerant onto the top of the tube array to study the liquid flow rate influence. All the tubes are instrumented to measure the temperature profile of the water flowing inside. This temperature profile approach, importantly, allows local heat transfer coefficients to be measured at the center of each tube in the test array, rather than tube length averaged values available in the past in the literature. Local heat transfer coefficients are more valuable for developing local prediction methods required for incremental design of heat exchangers. The tube array also used a two pass design for the water-side to achieve uniform axial liquid flow rates after each two tubes as opposed to one-pass designs in previous studies that tend to create a progressive maldistribution.

For one tube, the measured parameters to define the heat transfer conditions and then calculate the heat transfer performance are: the water flow rate inside the tube from the water flow meter, the temperature profile from the six thermocouples (two at each of the three locations), the saturation pressure from the two pressure transducers in the test section and the liquid refrigerant flow rate on the tube, measured for the top of the tube array and calculated from an energy balance for the other tubes.

Chapter 4

Modified Wilson Plot Technique

In this chapter, the procedure to determine the external heat transfer coefficient between the outside surface of the copper tubes and the refrigerant from the measurements is described. This procedure requires knowledge of the internal heat transfer coefficient α_i between the the water and the copper tube. The Wilson plot technique to find this internal heat transfer coefficient is described and the results of this method applied to each type of tube tested. The Wilson plot procedure was implemented using nucleate pool boiling on the outside of the tubes.

4.1 Heat transfer calculation principle

The local heat transfer coefficient during boiling on the outside of a tube is given by Newton's law of cooling to be the ratio of the heat flux to the temperature difference across the film layer:

$$\alpha_o = \frac{q_o}{T_{wall,o} - T_{sat}} \tag{4.1}$$

where T_{sat} is the saturation temperature of the vapor and $T_{w,o}$ the temperature of the tube surface. The surface temperature of the tube is not measured in this study. The external heat transfer coefficient is derived from a temperature measurement of the water flowing inside the tube.

The internally mounted thermocouples measuring the water temperature within the tubes in the axial flow direction permit the water temperature profile to be determined as a function the distance x along the tubes:

$$T_{wat} = f(x) \tag{4.2}$$

With the assumption that axial conduction along the tubes is negligible, an energy balance on a differential element of water inside the tube gives

$$\mathrm{d}q = \dot{m} c_{p,wat} \mathrm{d}T_{wat} \tag{4.3}$$

where $\dot{m}$ is the mass flow rate and $c_{p,wat}$ is the specific heat of water. The local heat flux on the outside of the tube may be expressed as

$$q_o = \frac{\mathrm{d}q}{\mathrm{d}A_o} = \frac{dq}{\pi D_o \mathrm{d}x} \tag{4.4}$$

Substituting from equation 4.3, it follows that

$$q_o = \frac{\dot{m} c_{p,wat}}{\pi D_o} \frac{\mathrm{d}T_{wat}}{\mathrm{d}x} \tag{4.5}$$

A similar method was first developed by Zürcher [ZURC00] for evaporation inside tubes. In this work, an enthalpy profile is determined from discrete water temperature measurements in a tube. Local values of the heat flux are determined by the derivative of this enthalpy profile. It was adapted here to boiling on the outside of tubes similar to Thome and Robinson [THOM03].

The thermal resistance of a differential element of the tube is the sum of the thermal resistance for boiling on the outside of the tube, the thermal resistance for convection inside, and the thermal resistance for conduction through the wall:

$$R_{tot} = R_o + R_i + R_w \tag{4.6}$$

In terms of heat transfer coefficients, this equation gives locally

$$\frac{1}{U_o \mathrm{d}A_o} = \frac{1}{\alpha_o \mathrm{d}A_o} + \frac{1}{\alpha_i \mathrm{d}A_i} + R_w \tag{4.7}$$

where U_o is the overall heat transfer coefficient and α_o and α_i are the outside and the inside heat transfer coefficients, respectively. Multiplying equation 4.7 by the outer surface of the differential element $dA_o = \pi D_o \mathrm{d}x$ results in

$$\frac{1}{U_o} = \frac{1}{\alpha_o} + \frac{1}{\alpha_i} \left(\frac{D_o}{Di} \right) + r_w \tag{4.8}$$

where

$$r_w = \pi D_o \mathrm{d}x R_w = \frac{D_o}{2\lambda_{cop}} \ln \left(\frac{D_{or}}{D_i} \right) \tag{4.9}$$

D_i is the inside diameter of the tube and D_{or} the outside root diameter of the enhanced tubes. For the plain tube D_{or} is the outer diameter D_o. This means for the thermal conductive resistance of the tube wall, the fins on the outside and the ribs on the inside of the tube are not considered. They are encompassed in the external and internal heat transfer coefficients.

Using the local overall heat transfer coefficient U_o, the heat flux can be written alternatively to equation 4.5 as

$$q_o = U_o(T_{wat} - T_{sat}) \tag{4.10}$$

The goal of this study is to determine the heat transfer on the outside of the tube. With the help of equations 4.5, 4.8, 4.9, and 4.10, the external heat transfer can be calculated only if the internal heat transfer coefficient is known. In order to determine the experimental boiling heat transfer coefficient with a minimum of uncertainty, it is necessary to characterize the water side heat transfer coefficient as accurately as possible. The technique used to determine the water side coefficient is described in the following section.

4.2 Modified Wilson plot method

The principle of this method is to assume that each heat transfer coefficient (internal and external) is following its characteristic relationship. However, these two relationships each include an unknown multiplicative constant. The Wilson plot technique consists of measuring the overall heat transfer for several conditions (at different water Reynolds number covering the expected range in the experiments) and correlating all the results together to find the two unknown constants. The goal is to find an accurate predictive relation for the internal heat transfer in the tube between the water and the copper.

4.2.1 Internal heat transfer coefficient

For the internal heat transfer coefficient, one of the most accurate relations for single phase internal flow is the Gnielinski correlation [GNIE76]. This correlation is suitable for Reynolds numbers corresponding to the transition region ($2300 \lesssim Re_{Dh} \lesssim 10000$) as well as the fully turbulent regime up to $Re_{Dh} = 10^6$:

$$\alpha_{gni} = \frac{Nu_{gni}\lambda_{wat}}{D_h} = \frac{(f/8)(Re_{Dh} - 1000)Pr_{wat}}{1 + 12.7(f/8)^{1/2}(Pr_{wat}^{2/3} - 1)} \frac{\lambda_{wat}}{D_h} \tag{4.11}$$

Pr_{wat} is the Prandtl number

$$Pr_{wat} = \frac{\mu_{wat} c_{p,wat}}{\lambda_{wat}} \tag{4.12}$$

Nu is the Nusselt number

$$Nu = \frac{\alpha D_h}{\lambda_{wat}} \tag{4.13}$$

and where D_h is the hydraulic diameter inside the tube for the annulus section (there is an 8.0mm stainless steel tube centered inside the tubes tested with the water-side thermocouples that measure the water temperature profile):

$$D_h = \frac{4 \times cross\ section}{wetted\ perimeter} = \frac{4\pi(D_i^2 - D_{inox}^2)}{4\pi(D_i + D_{inox})} = D_i - D_{inox} \tag{4.14}$$

A correlation for the friction factor f for a smooth surface has been developed by Petukhov [PETUKHOV96]:

$$f = (0.79 \ln Re_{Dh} - 1.64)^{-2} \quad 3000 \lesssim Re_{Dh} \lesssim 5 \times 10^6 \tag{4.15}$$

The enhanced tested tubes have also an enhancement of their internal surface to improve the overall heat transfer coefficient between the water and the refrigerant. The Petukhov relation for the friction factor is strictly only valid for a smooth internal tube surface. However, this correlation was used for all measurements. The effect of all internal enhancement is taken into account in the leading constant C_i (see equation 4.16).

In the Wilson plot technique, one assumes that the internal heat transfer coefficient α_i is the one given by the Gnielinski correlation multiplied by a constant C_i to be determined experimentally:

$$\alpha_i = C_i \alpha_{gni} \tag{4.16}$$

The leading constant C_i characterizes the influence of the inside surface enhancement on the heat transfer. It also includes the influence of the copper wire wound around the inner stainless steel tube to increase mixing and improve the accuracy and uniformity of water temperature measurements.

4.2.2 External heat transfer coefficient

For the outside of the tube, the chosen test condition is nucleate pool boiling. The main reasons of this choice are:

- It is easy to recreate and maintain the external conditions. The tube being evaluated is immersed in a refrigerant liquid pool within the test section while an upper tube condenses the vapor formed.
- The external coefficient is important and its influence on the measured overall U_o is thus minimized, which is desirable for measuring Ci accurately (an attempt was made to achieve Wilson plots with condensation on the outside of the tubes but the external heat transfer coefficients were too small).

- The external boiling heat transfer coefficient is easily represented by a proportional correlation, similar to the assumption of the Wilson plot technique.

For nucleate pool boiling, the correlation from Cooper [COOPER84] predicts the following relation between the external heat transfer coefficient and the heat flux:

$$\alpha \sim q_o^{0.7} \tag{4.17}$$

Which became in our case:

$$\alpha_o = C_o q_o^{0.7} \tag{4.18}$$

The value of the exponent (0.7) in this relation might be different for the current tested tubes, but it is used as a first step and the influence of this exponent value on the constants C_i will be will be discussed in section 4.4.

4.2.3 Overall heat transfer coefficient

The overall heat transfer coefficient U_o is given by equation 4.8. Substitution of equations 4.16 and 4.18 in this equation and rearranging leads to

$$\left(\frac{1}{U_o} - r_w\right) q_o^{0.7} = \frac{1}{C_i}\left(\frac{q_o^{0.7}}{\alpha_{gni}}\right)\left(\frac{D_o}{Di}\right) + \frac{1}{C_o} \tag{4.19}$$

Defining

$$Y = \left(\frac{1}{U_o} - r_w\right) q_o^{0.7} \tag{4.20}$$

and

$$X = \left(\frac{q_o^{0.7}}{\alpha_{gni}}\right)\left(\frac{D_o}{Di}\right) \tag{4.21}$$

Equation 4.19 has a simple linear form of

$$Y = \frac{1}{C_i} X + \frac{1}{C_o} \tag{4.22}$$

With a change of the water velocity, the values of X and Y are altered. The modified Wilson plot technique consists of measuring several points of this linear relation and performing a linear regression on these points. The inverse slope of this fit gives the value of C_i and the inverse of the Y-axis intercept yields C_o. Our interest is the value of C_i, as in combination with the Gnielinski correlation the water side coefficient can be determined according to 4.16.

4.2.4 Measurement procedure

The experimental procedure for the Wilson plot technique on a single tube is the following:

1. The tube to be tested is connected to the water loop in a one water pass configuration. The top two tubes are connected in a two pass configuration to a thermal bath which provides cold glycol. Condensation takes place on these two tubes to compensate for the evaporation on the tested tube. All the other tubes are inactive.

2. The outlet of the test section is closed and test section is filled with refrigerant by the pump. The liquid level is adjusted to be just above the tested tube and then the test section is isolated from the rest of the refrigerant circuit.

3. The temperature and the flow rate of the water are adjusted to reach the desired heat flux on the tube while the temperature of the glycol is chosen to maintain the saturation conditions. When everything is stable, an acquisition of the key parameters is made.

4. Water flow rate and water temperature are then changed so that the heat flux (and thus the external heat transfer coefficient of equation 4.18) remains constant. For example, the inlet temperature is decreased and the flow rate is increased.

This last operation is repeated for each measurement point. The conditions of the water in terms of temperature and flow rate in this Wilson plot technique are chosen to cover the planned experimental conditions so that the relation for the water side heat transfer will be applicable.

4.3 Physical properties evaluation

All the physical properties of water were determined with the software EES©. For the physical properties of the refrigerant, the software REFPROP© was used. The values have been exported from these programs as a function of temperature into a look up table with a step size of $0.1K$. Every time a physical property is necessary, the calculation program goes into this table and makes a linear interpolation of the value based on the current temperature and the two closest ones in the table. The linear interpolation is usually based on the temperature but could also be any other property. For example, the properties of the refrigerant at saturation are often determined based on the pressure. By this procedure, accurate values of the physical properties are used all the time in the calculations. This is important especially for the water, which is just above its freezing point where the viscosity changes rapidly.

4.4 Results and accuracy

The results of a modified Wilson plot for a plain tube is shown in figure 4.1 (those for the other tubes are shown in Appendix B).

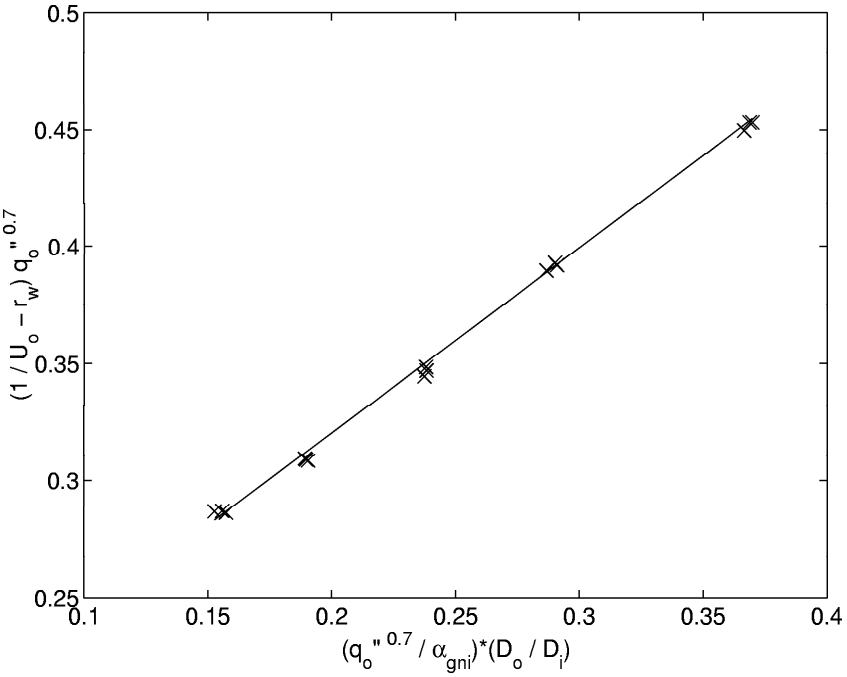

Figure 4.1: A modified Wilson plot for the plain tube, heat flux of $26kW/m^2K$ and water Reynolds numbers from 6000 to 16000, C_i=1.26.

The slope of the linear regression in this plot corresponds to the inverse of the corrective multiplier, C_i, for the internal heat transfer coefficient.

The modified Wilson tests were conducted over a water side Reynolds number range from 6000 to 16000. For the plain tube, different instrumented stainless steel tubes inside different plain tubes were tested to verify the reproducibility of the measurements. To check the reliability of the method, tests were performed also at different heat fluxes and different saturation temperatures, implying different water temperatures.

The results of all modified Wilson plots for the plain tube are summarized in table 4.1.

instrumented rod	T_{sat} [K]	q_o $[kW/m^2]$	C_i [-]
5	284	25	1.30
6	284	25	1.18
3	284	24	1.27
4	284	26	1.26
2	284	26	1.19
4	284	25	1.40
4	292	34	1.26
4	300	34	1.30
average value for plain tube			1.27

Table 4.1: Measurements of the corrective multiplier of the water side coefficient for the plain tube.

The measured value C_i does not show a distinct dependence of heat flux or temperature. For this reason, the average value of 1.27 obtained from all eight Wilson plots is used for the plain tubes. The uncertainty of this value is estimated to be within ± 0.1. The value of C_i includes the effect of the inserted rod with a spiral wire wound on it and so it is expected to be larger than the normal value of 1.0. The coefficients C_i have also been calculated at the three different temperature measurement locations in the tube. No significant difference between the three values was observed indicating that the water flow is developed all along the tube. The flow developing length is reduced by the spiral wire. For the three other tubes, the developing length should be even shorter as they are internally enhanced.

For each type of enhanced tube, three modified Wilson plots tests were conducted: Two measurements of different instrumented rods under identical conditions and one test at a different heat flux. All tests were performed at a saturation temperature close to room temperature. The results of these tests are given in tables 4.2 to 4.4.

instrumented rod	T_{sat} [K]	q_o $[kW/m^2]$	C_i [-]
10	287	40	4.29
10	287	80	3.95
3	287	80	3.83
average value for Turbo-BII			4.03

Table 4.2: Measurements of the corrective multiplier of the water side coefficient for the Turbo-BII tube.

The average values of C_i are: for Turbo-BII HP, 4.03, for Gewa-B, 4.09, and for High-Flux, 4.22. The uncertainty for these values is estimated to be within ± 0.2.

instrumented rod	T_{sat} [K]	q_o $[kW/m^2]$	C_i [-]
3	287	80	3.98
10	287	80	4.16
10	287	40	4.13
average value for Gewa-B			4.09

Table 4.3: Measurements of the corrective multiplier of the water side coefficient for the Gewa-B tube.

instrumented rod	T_{sat} [K]	q_o $[kW/m^2]$	C_i [-]
10	295	70	4.08
3	292	40	4.50
3	295	60	4.09
average value for High-Flux			4.22

Table 4.4: Measurements of the corrective multiplier of the water side coefficient for the High-Flux tube.

The modified Wilson plot technique takes into account the eventual variation of the heat flux during the measurements by assuming a relation for the external heat transfer coefficient (equation 4.18) but this heat flux was maintained as constant as possible during the experiments (variation of 1 to 1.5%). The variation of the external heat transfer coefficient is thus limited.

It will be found in chapter 6 that, in nucleate pool boiling conditions, $\alpha \sim q_o^n$ with n=0.4 for the plain tubes and n is negative for the enhanced tubes. These values of this exponent are different than the one used in equation 4.18 (n=0.7). However, the influence of this parameter on the constant C_i is small. For example, the measurements of the first Wilson plot on the High-Flux tube have been reprocessed. The initial value of C_i was 4.08 with the exponent n=0.7 while C_i is found to be 4.095 with the exponent n=-0.6 from the pool boiling measurements. This difference is largely covered by the uncertainty of ± 0.2 taken on the C_i coefficient.

4.5 Conclusions

The water side heat transfer coefficients were determined experimentally for all tubes using a modified Wilson plot technique. The Wilson plot procedure was implemented using nucleate boiling on the outside of the tube. The external heat transfer coefficient was thus only a function of the heat flux. During the measurements, the water flow rate and temperature were changed to obtain a variation of the water side heat transfer coefficient

but the heat flux was maintained constant. The water-side heat transfer multipliers C_i for the various tubes to be experimentally tested were accurately obtained, which include the characteristics of the experimental setup. This means mainly the influence of the instrumented stainless steel tube with its spiral wound wire and also the internal enhancement of the copper tubes. With these corrective multipliers and the Gnielinski correlation, the water side coefficient can be accurately calculated. A known water side coefficient allows the determination of the external heat transfer coefficient during boiling and falling film evaporation based on measurement of the water temperature inside the tube and its profile to get the local heat flux.

Chapter 5

Flow pattern visualization and map

Besides heat transfer considerations in the falling film evaporators, the intertube flow pattern and respective map are investigated as part of this study. A flow pattern map is basically a diagram or a predictive method from which it is possible to determine, at given conditions, the particular flow mode of the liquid falling between the tubes. Additionally, it could also be used to investigate any influence of flow mode on heat transfer. This chapter starts with an introduction to the flow patterns with the definition of the flow modes. Next, the adiabatic flow mode test facility is described. Then follows a description of the adiabatic measurements made on this test facility. A fourth part presents the flow mode observations with the refrigerant in the heat transfer test facility. These observations are made with and without heat transfer.

5.1 Flow pattern map and flow modes

In two phase heat transfer, the liquid flows are complex. In falling film evaporation, the liquid is usually flowing on enhanced surfaces; when the heat flux is high enough, there is boiling in the liquid film. For those reasons, it is extremely difficult to study in details the liquid flow. There are heat transfer models for low Reynolds number films on simple geometries (i.e. condensation on fin tubes) but with the eventual boiling and the higher liquid flow rate necessary for evaporation, liquid flow is more complex (especially with numerous growing bubbles in the falling film too). However, there are observable characteristics. These characteristics are classified and make up the flow modes. The parameters of these flow modes are: liquid physical properties, the liquid flow rate on the tube, the tube itself, the distance in-between the tubes and the tube diameter.

There are three principal flow modes when a liquid is flowing from tube

to tube on a vertical array of horizontal tubes: droplet mode, column mode and sheet mode. These three principal flow modes are depicted in figure 5.1.

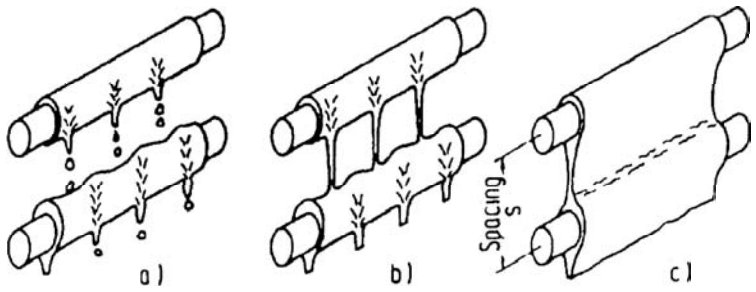

Figure 5.1: Schematic of the three main flow modes: a) droplet mode, b) column mode and c) sheet mode from Mitrovic [MITR86]

Despite numerous observations of condensation and falling film evaporation on rows of tubes, apparently no generalized flow mode map is currently available for either plain or enhanced types of tubes, although Honda et al. [HOND87] have presented several transition expressions for fluids condensing on low finned tubes. These processes however are similar to that of an adiabatic falling film of liquid fed onto the top of a tube array, which has been studied extensively by Hu and Jacobi [HU96a] on plain tubes for a variety of fluids, tube diameters, tube pitches and flow rates and with/without cocurrent gas flow. Based on their observations, they proposed a flow mode transition map with coordinates of film Reynolds number (Re) versus a modified Galileo number (Ga). The map delineates the transitions between the three dominant modes (sheet, column and droplet) with two mixed mode zones (column-sheet and droplet-column) in which both modes are present. Their corresponding four flow transition expressions between these five zones are given below for plain tubes (valid for passing through the transitions in either direction and hence the symbol $\Longleftrightarrow$):

$$Droplet \Longleftrightarrow Droplet - Column : Re = 0.074\ Ga^{0.302} \tag{5.1}$$

$$Droplet - Column \Longleftrightarrow Column : Re = 0.096\ Ga^{0.301} \tag{5.2}$$

$$Column \Longleftrightarrow Column - Sheet : Re = 1.414\ Ga^{0.233} \tag{5.3}$$

$$Column - Sheet \Longleftrightarrow Sheet : Re = 1.448\ Ga^{0.236} \tag{5.4}$$

where the modified Gallileo number of the liquid is defined as

$$Ga = \frac{\rho\sigma^3}{\mu^4 g} \tag{5.5}$$

and the liquid film Reynolds number is defined as

$$Re = \frac{4\Gamma}{\mu} \tag{5.6}$$

where Γ is the flow rate on one side and 2Γ is the total flow rate on both sides of the tube [kg/m s], ρ is the density of the liquid, μ is liquid dynamic viscosity, σ the surface tension, and g is the acceleration due to gravity. This map is applicable to plain tubes for cocurrent, i.e., downflow, air velocities less than 15 m/s. With these relations, the authors could predict accurately their measurements. For this, this type of relation between the Reynolds number and the modified Gallileo has been used to correlate the current measurements.

The modified Gallileo number may be interpreted as the second power of the gravity to viscous forces: $Ga = (F_g/F_\nu)^2$. It is equal to the square of the Gallileo number (gL^3/ν^2) calculated with the capillary length ($L = \sqrt{\sigma/\rho g}$).

An extensive investigation on falling film flow mode transitions of adiabatic and non-phase change films was presented for plain tubes by Mitrovic [MITR86]. Various other studies have investigated the dynamics of transitions, droplet formation and column departure wavelengths, such as those of Taghavi and Dhir [TAGH80], Tang and Lu [TANG91] and Mitrovic and Ricoeur [MITR95]. Hu and Jacobi [HU98] have recently reported additional data on tube spacing effects on column and droplet departure wavelengths.

In the present investigation the three principal and two intermediate transition modes have been observed. Photographs of these flow modes using the adiabatic test are given in figure 5.2.

The principal flow modes are described below together with the two intermediate modes.

5.1.1 Droplet mode

When a small amount of liquid is flowing on a tube, the flow off the bottom of the tube is intermittent and presents only droplets. There are no continuous liquid links between the bottom of one tube and the top of the next tube below. The frequency of these droplets increases with flow rate while the distance between the droplet departure sites remain the same. This distance is defined by the Taylor instability and corresponds to the length of the wave that is most likely to occur:

$$\lambda_d = 2\pi\sqrt{\frac{2\sigma}{\rho_L g}} \tag{5.7}$$

5.1.2 Column mode

When the flow rate is increased further, there is a point when there is enough liquid to make the droplets merge vertically together and form continuous liquid columns between the tubes. If the liquid is flowing only in this form

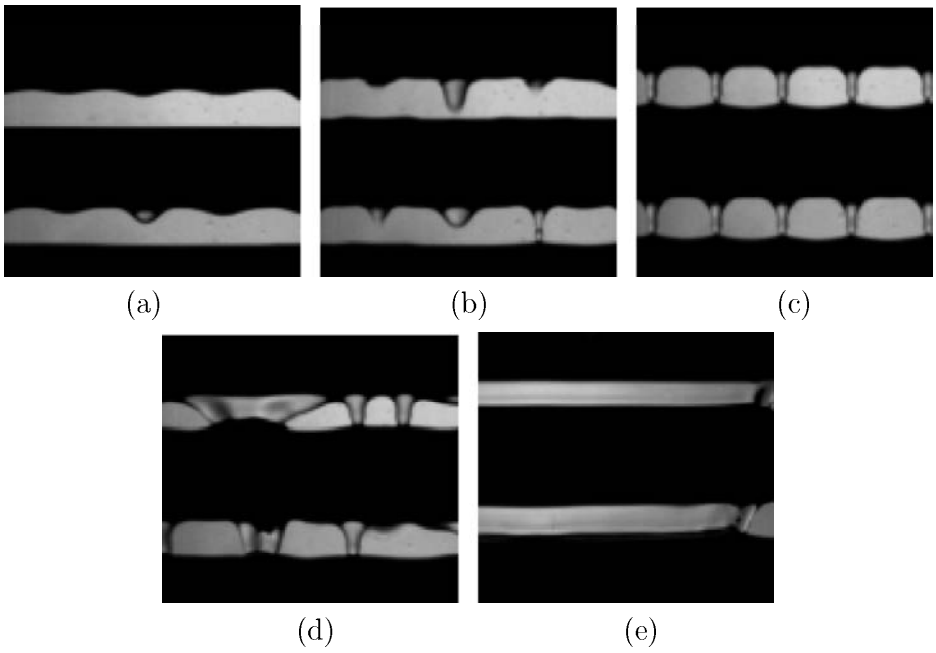

Figure 5.2: Intertube flow modes observed on the adiabatic test facility using glycol as working fluid: (a) droplet, (b) droplet-column, (c) column, (d) column-sheet and (e) sheet.

from the bottom of one tube to the top of the one below, the mode in this intertube is: Column mode. The diameter of the columns width increases with the flow rate while the distance between columns remains constant and close to the droplet departure site distance and the wavelength of the Taylor instability.

A distinction is made in this mode regarding the relative position between the columns of one inter-tube space and the columns of the following inter-tube space:

In-line column. At the beginning of the column mode (in terms of increasing flow rate), the liquid does not spread enough when it impinges on the top of a tube to encounter that of the neighboring columns and the next column at the bottom of this tube is formed exactly at the same position. The columns are thus vertically aligned. This inline column position does not exist for all the liquid/tube combinations. It is more likely observed with viscous fluids and with low fin tubes. These two factors limit the lateral spreading of liquid and make the in-line column mode possible (the column mode in figure 5.2 corresponds to the above description).

Staggered column. When the flow rate is high enough (remaining in the column mode), the liquid spreads evermore laterally on the tube surface. On both sides of the impingement region, the liquid flows horizontally on

the surface. The flows from two neighboring columns encounter each other and create a crest in the liquid layer. This crest forms a ring all around the tube. At the bottom of the tube, this ring is the departure site for a column in the next intertube space. The column positions are consequently shifted from one intertube to the following one. This shift length one half of the inter-column distance. This staggered column mode exists for each tube/liquid configuration and is that most typically observed.

5.1.3 Sheet mode

At even higher flow rate, the diameters of the columns increase and they become non cylindrical. The liquid columns spreads in the lateral direction along the tubes and form a liquid sheet. At the beginning, this sheet is not continuous but forms several unstable triangular small sheets (see Column-Sheet description below) from two neighboring columns. With increasing flow rate, those small sheets merge together and form a complete sheet along the entire tube length. The sheet mode is reached when there is one single wide sheet between the two tubes.

These three modes are the principal ones but in between, there are two intermediate modes. These intermediate modes help in the description of the transition between one principal mode to the following one and corresponds in fact to the coexistence of the two principal modes.

5.1.4 Droplet-Column mode

Between the stable droplet and column modes, there is an intermediate mode where droplets and columns coexist. In this mode, the liquid falls at the bottom of the tube from the departure sites (identical for droplet or column). Between these departure sites, the distance is most of time λ and the liquid falls from these sites as a column or droplet. The droplet-column mode starts when there is at least one stable column and finishes when the last droplet site is replaced with a column site.

5.1.5 Column-Sheet mode

Between the column and sheet mode, there is an intermediate mode in which there are both columns and small sheets coexisting. This mode is the column-sheet mode. It starts when the two first columns merge and form a small sheet and finishes when a complete single sheet is formed.

5.2 Adiabatic flow mode test facility

In order to study the flow modes in adiabatic conditions a test facility has been developed. Results obtained with this test facility have been pub-

lished already in [ROQU01], [ROQU02A], [ROQU02B], and [ROQU03]. A description of the test facility and a summary of the main results are given below.

A diagram and photos of the test facility used for these adiabatic falling film test are shown in figures 5.3 and 5.4. It is composed of three main parts:

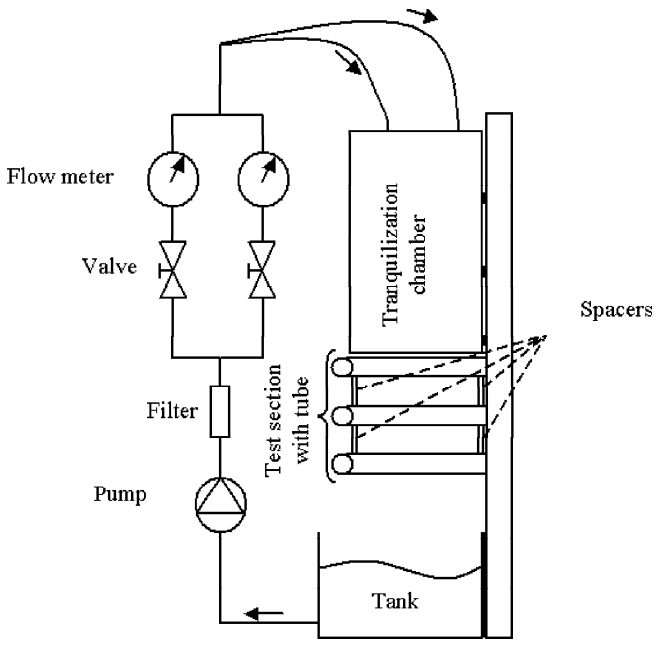

Figure 5.3: Diagram of the adiabatic test rig.

- Fluid Circuit: The fluid starts first from the tank that serves as a reservoir for the whole circuit, and then passes through a centrifugal pump. This type of pump was chosen to avoid oscillations in the mass flow and the pressure. A filter then eliminates any dust or particles in the fluid. The flow rate is measured with one of two rotameters, which are necessary because the ranges of mass flow and viscosity were too large for only one rotameter. The temperature in the liquid bath is measured with a thermocouple for calculation of the liquid properties.

- Flow Tranquilization Chamber: Its function is to insure a uniform flow from the top tube onto the second tube. It is a box of $300 \times 260 \times 10mm$ (inside $Height \times Width \times Depth$) in which the flow enters at the top through two holes. For the lowest viscosity fluid in this study (water), a grid with foam is added in the middle of this chamber to increase the homogenization effect. The fluid leaves this box at the bottom through

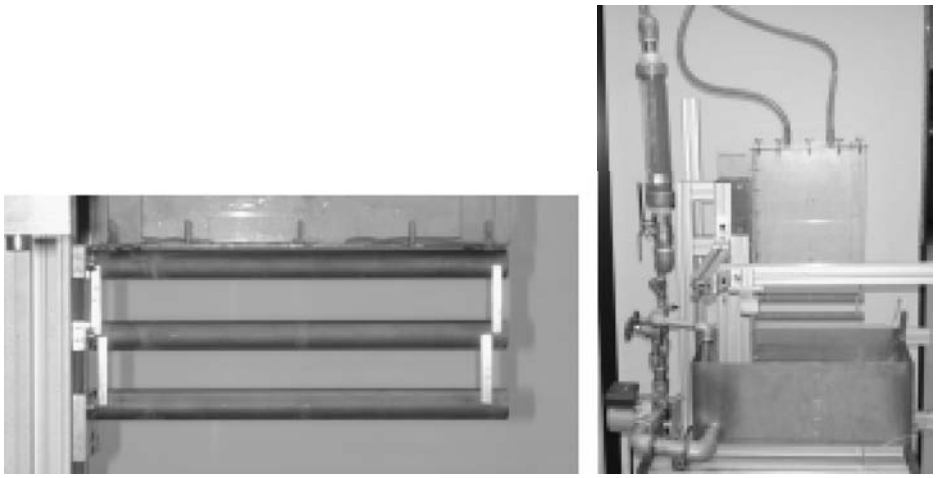

(a) (b)

Figure 5.4: Photos of the test section: (a) test section; (b) overall view.

a flat plate with $1mm$ diameter holes spaced $2mm$ apart. The length of this distribution system (and the resulting film visualized) is $200mm$.

- Test Section: It is comprised of three tubes on which the fluid flows. They are held at one end and the distance between them is fixed with appropriately manufactured spacers. Care is taken to obtain a precise alignment of the horizontal tubes into a vertical array.

5.3 Flow mode transitions on the adiabatic test facility

The first objective was to observe the intertube flow modes and determine what transition takes place as the flow rate is varied. Secondly, the flow rate was measured in order to determine the flow rate at which the various transitions take place. In order to cover a wide range of physical properties three different working fluids were used: water, glycol and a water glycol mixture (50%/50% weight). Measurements have been taken at ambient temperature. Conditions with six different tube pitches were studied: 22.25, 23.85, 25.45, 28.55, 38.45 and $43.95mm$. Nine different types of tubes have been tested including a plain tube, low finned tubes (19 fpi, 26 fpi, 40 fpi), enhanced boiling boiling tubes (Turbo-BII HP and Gewa-B), and enhanced condensing tubes (Turbo-CSL, Gewa-C and Thermoexcel-C).

Below the main results for the types of tubes of interest in the current study, the plain tube, the Turbo-BII HP tube, and the Gewa-B are given. For detailed results of all tubes tested refer to [ROQU01], [ROQU02A],

[ROQU02B], and [ROQU03].

Neglecting the effect of tube spacing, the results have been analyzed using two dimensionless groups. The fluid type is characterized by the modified Gallileo number Ga. The mass flow rate is included in the film Reynolds number Re. The Reynolds number at transition can be correlated as a function of the Galileo number as:

$$Re = a \cdot Ga^b \tag{5.8}$$

where a transition is the change from one flow mode to another one. As there are five modes, there are four transitions (or eight if one takes into account the hysterisis effect for increasing or decreasing flow conditions). Since only a small degree of hysteresis was observed, the observations of these two cases are put together to find the transitions.

As an example the observations of the four flow transitions for the plain tube are presented in figure 5.5. Each graph corresponds to a transition between two successive flow modes. The circles are the measured Reynolds numbers at the transition and the three groups of measurements correspond to the three different tested fluids (three Gallileo numbers). The solid lines represent the transition prediction method calculated from the measurements (equation 5.8).

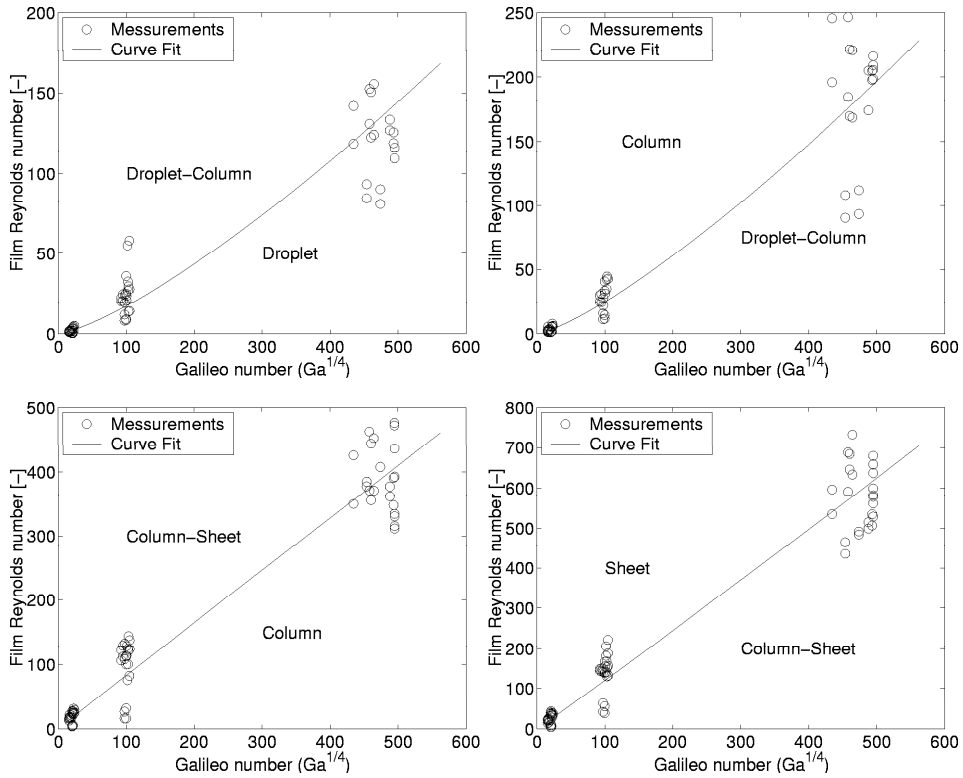

Figure 5.5: Observed flow modes on plain tube in adiabatic conditions for glycol, water-glycol and water (all tube pitches).

Tube	Transition	a	b
Plain Tube	Droplet to/from Droplet-Column	0.0417	0.3278
	Droplet-Column to/from Column	0.0683	0.3204
	Column to/from Column-Sheet	0.8553	0.2483
	Column-Sheet to/from Sheet	1.0680	0.2563
Turbo-BII HP	Droplet to/from Droplet-Column	0.0754	0.3007
	Droplet-Column to/from Column	0.1594	0.2748
	Column to/from Column-Sheet	0.7591	0.2582
	Column-Sheet to/from Sheet	1.3487	0.2453
Gewa-B	Droplet to/from Droplet-Column	0.0683	0.3039
	Droplet-Column to/from Column	0.1618	0.2745
	Column to/from Column-Sheet	0.5988	0.2561
	Column-Sheet to/from Sheet	0.5737	0.2847

Table 5.1: Coefficients for transition relations

The numerical values of the coefficients a and b of the relation 5.8 for each tube and transition are presented in table 5.1. The values for the plain tube have been used to draw the curves in the figure 5.5. For the High-Flux tube no flow mode observations were made on the adiabatic test facility as the tube was not available at that time. All together, more than 2000 transition observations were made for all nine tubes for the three test fluids at six tube pitches.

A comparison for the correlations obtained for the plain tube, the Turbo-BII HP tube and the Gewa-B tube and the correlations of Hu and Jacobi [HU96a] is given in figure 5.6.

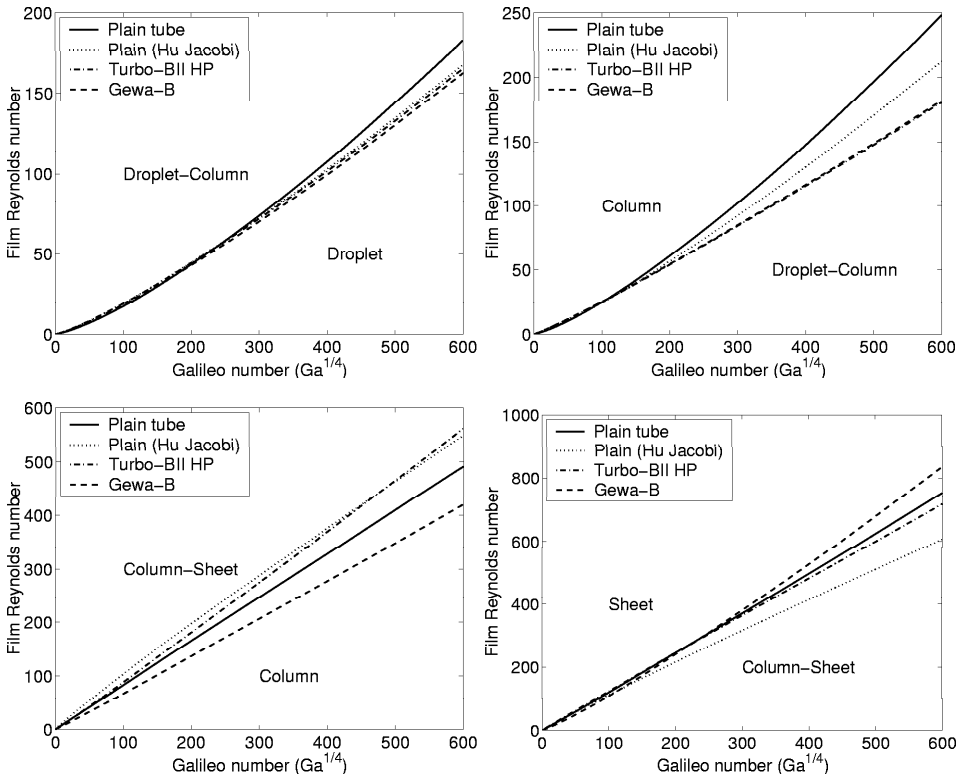

Figure 5.6: Observed flow modes on plain tube in adiabatic conditions for glycol, water-glycol and water (all tube pitches).

5.4 Flow mode transitions with refrigerant

5.4.1 Adiabatic conditions

The flow mode transitions were also determined with R-134a as working fluid under adiabatic condition for all four types of tubes tested. For this purpose the diabatic test facility was used. The test were performed at room temperature without water circulation inside the tubes.

The flow modes observed with $R134a$ on the plain tube at tube pitch of $23.9mm$ are depicted in figure 5.7

As seen on the figure, the flow mode detection with R-134a is very difficult as viscosity is very low and thus the flow is very unstable. For the other types of tubes a similar behavior was observed.

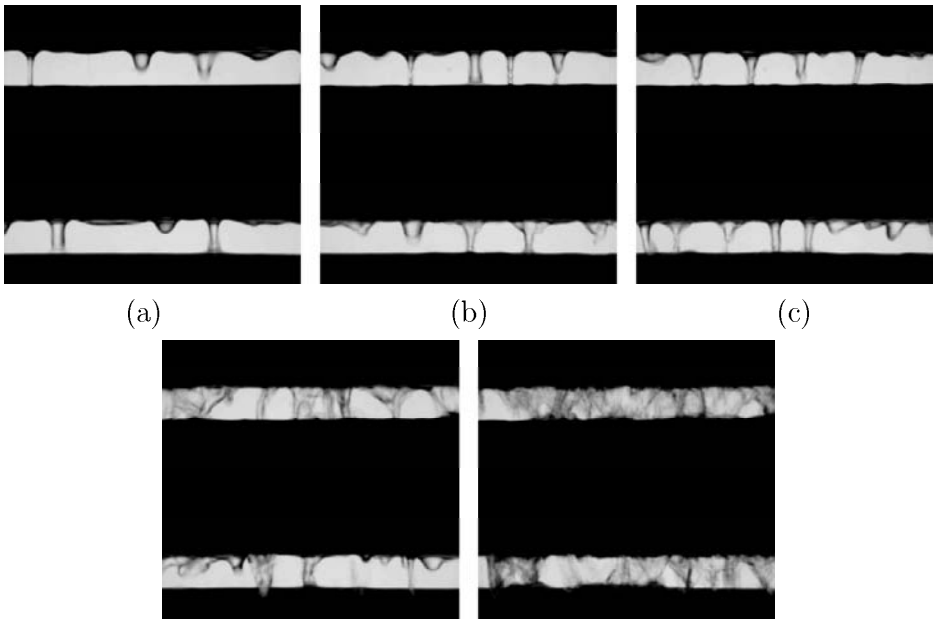

Figure 5.7: Intertube flow modes observed on the main test facility using R-134a (tp=23.8mm, plain tube) as working fluid: (a) droplet, (b) droplet-column, (c) column, (d) column-sheet and (e) sheet.

The results of all observations are presented in the figures 5.8 to 5.11. On each figure, the observations for the four transitions for one tube are plotted as circles. The effect of the tube pitch is neglected. In addition, in each figure, the transitions determined on the adiabatic test facility with other fluids as a function of the Galileo number are drawn as solid lines. In figure 5.11 for the High-Flux tube the prediction lines of the plain tube are plotted as no observations were performed on the adiabatic test facility and the difference in transitions Reynolds number are expected to be small for this tube compared to the plain tube.

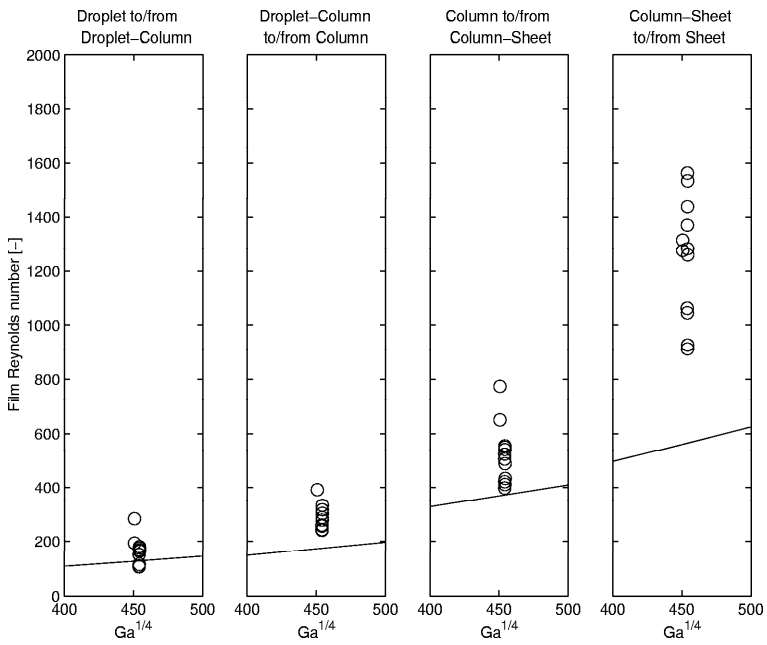

Figure 5.8: Comparison between the observed flow modes with R-134a and the previous predictive relation for the plain tube.

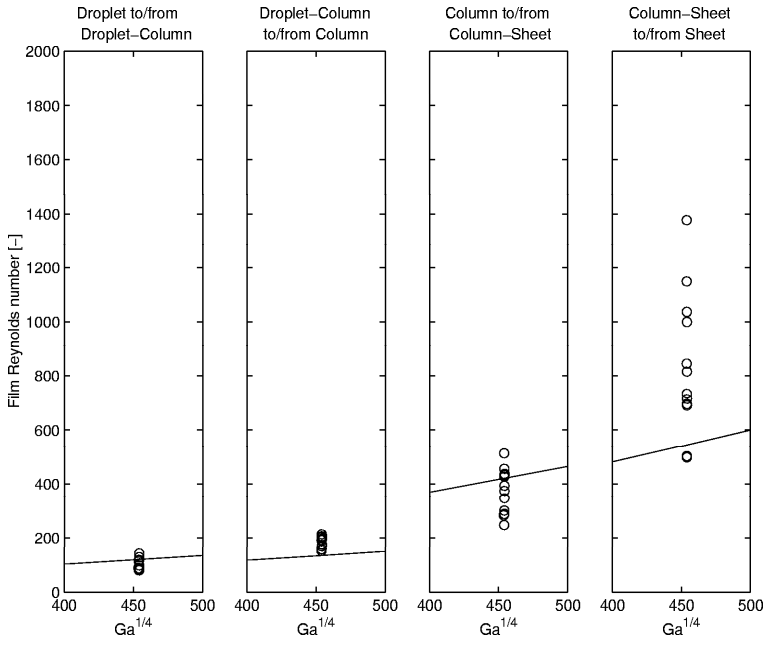

Figure 5.9: Comparison between the observed flow modes with R-134a and the previous predictive relation for the Turbo-BII HP tube.

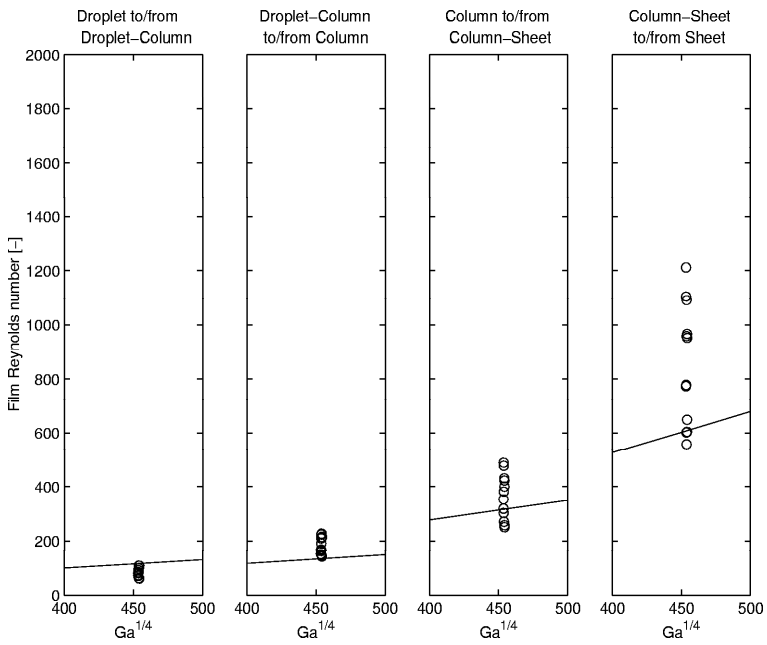

Figure 5.10: Comparison between the observed flow modes with R-134a and the previous predictive relation for the Gewa-B tube.

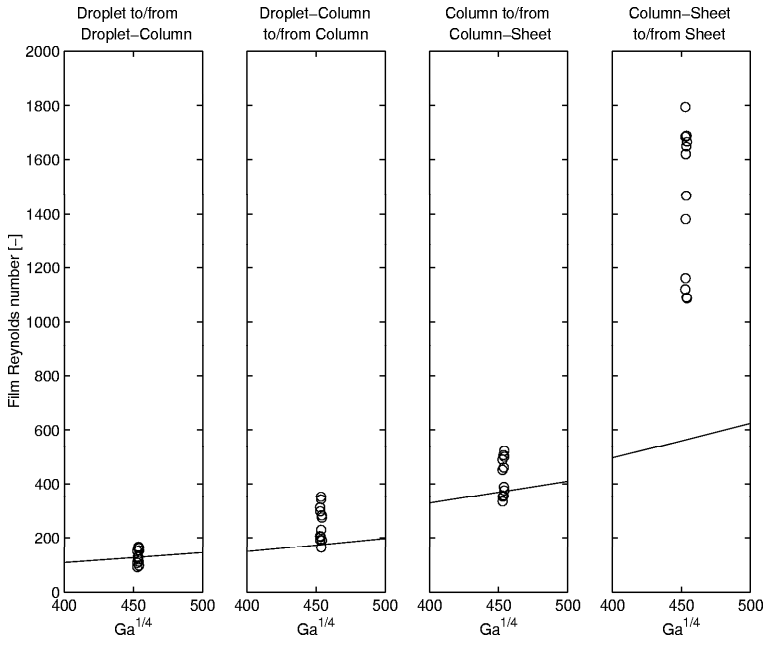

Figure 5.11: Comparison between the observed flow modes with R-134a and the previous predictive relation for the High-Flux tube.

The Galileo number of R-134 at $293K$ is about 454 and at $278K$ about 446. Thus, the variations in the transition Reynolds number are expected to be small for the further comparisons with the diabatic tests at saturation temperature of $278K$.

In general the transitions observed with refrigerant are predicted with the relations from the other fluids with similar accuracy. Except the transition column-sheet to/from sheet which was observed at higher film Reynolds number with refrigerant than the prediction. The differences where the transitions occur for the four types of tubes are small compared to differences in film Reynolds numbers that were observed for one tube at one transition.

The large ranges for the transition Reynolds numbers are probably due to classification difficulties as the transitions between the modes are not always discrete phenomena and it is hence difficult to ascertain exactly when it occurs.

5.4.2 Diabatic conditions

Figure 5.12 depicts the influence of heat transfer on the flow modes. The liquid overfeed rate is the same for all four cases. Without heat transfer, sheet mode is observed. With heat transfer, the film breaks down and column-sheet mode is obtained. When increasing the heat flux, the number of bubbles in the film increases and the flow is more destabilized.

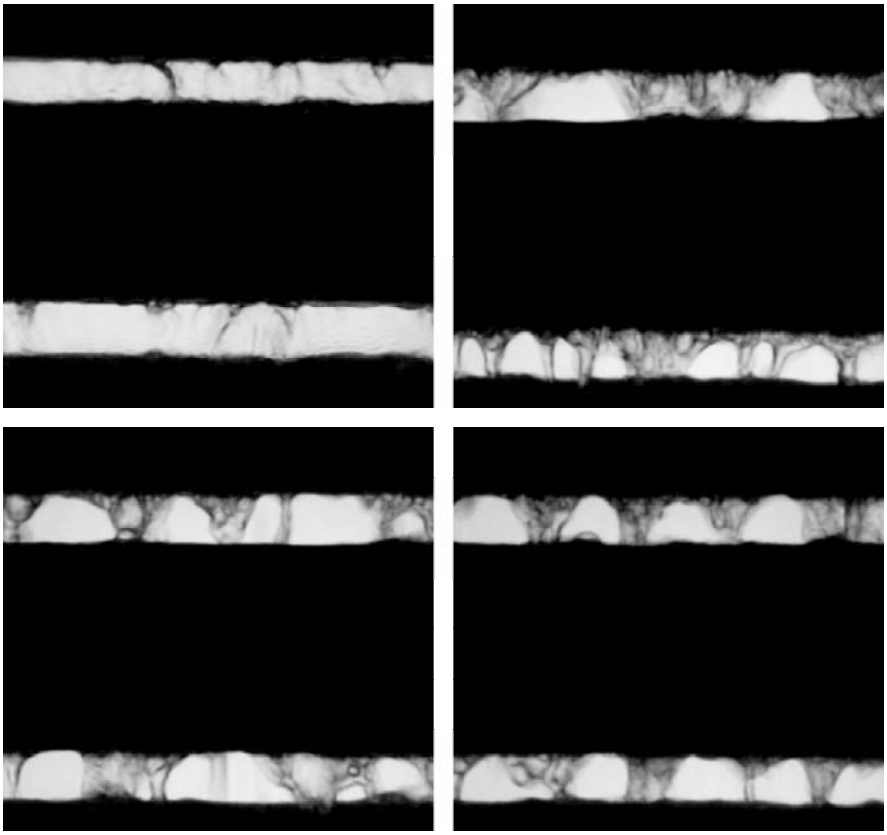

Figure 5.12: Influence of heat flux on Turbo-BII HP tube: no heat transfer (on the top left), $q_o = 20kW$ (on the top right), $q_o = 40kW$ (on bottom left), and $q_o = 60kW$ (on the bottom right).

The flow modes observed for the four types of tubes during the heat transfer measurements as a function of the film Reynolds number are given in figures 5.13 to 5.16. In those figures, the observed flow modes represented by the crosses are given as a function of the film Reynolds number. On the vertical axes, the flow modes are mentioned with abbreviations: D, droplet mode; D-C, droplet-column mode; C, column mode; C-S, column-sheet and S, sheet mode. In addition the flow mode transitions with $R134a$ determined under adiabatic conditions with the previous predictive method are drawn as vertical lines. From this graphs, it can be seen that the sheet mode was rarely observed on the enhanced tubes. The column-sheet mode is observed above his corresponding transition: column to/from column-sheet and the column mode is observed also above his corresponding transition: droplet-column to/from column but the overlap between these flow modes is important in terms of film Reynolds number. For the droplet-column and the droplet modes, the range of film Reynolds numbers where they

were observed is wider than the predictions in the adiabatic conditions. It can be concluded from this that the flow mode transitions in heat transfer conditions occur at significantly different Reynolds number compared to the adiabatic conditions. The transition are shifted to higher flow rate due to the film perturbation induced by the presence of nucleate boiling.

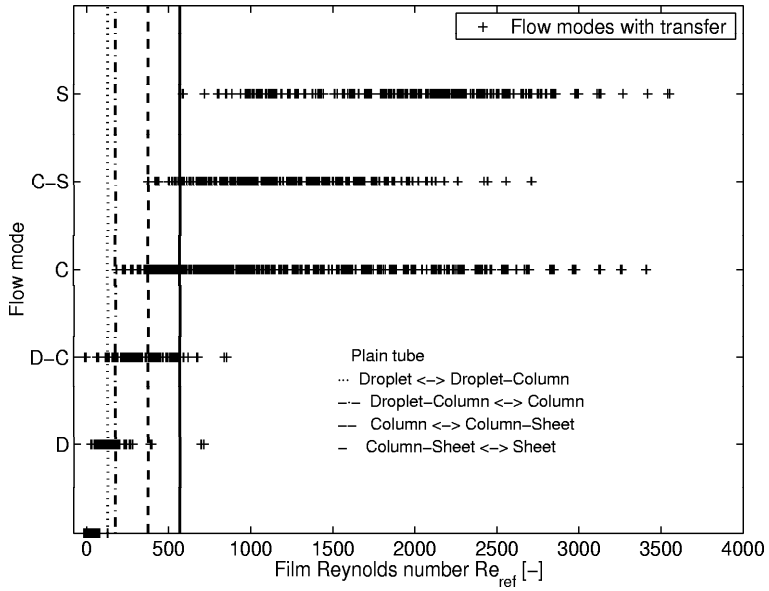

Figure 5.13: Observed flow modes in heat transfer conditions and adiabatic predictions for the plain tube.

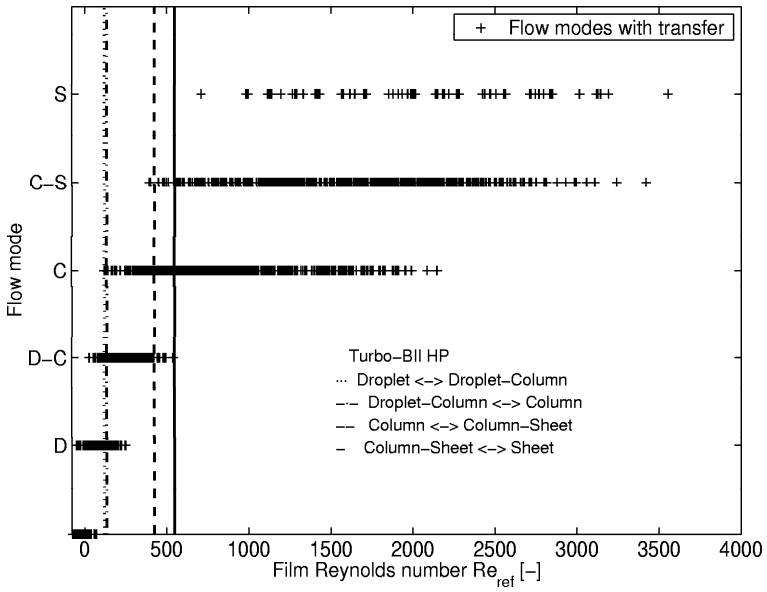

Figure 5.14: Observed flow modes in heat transfer conditions and adiabatic predictions for the Turbo-BII HP tube.

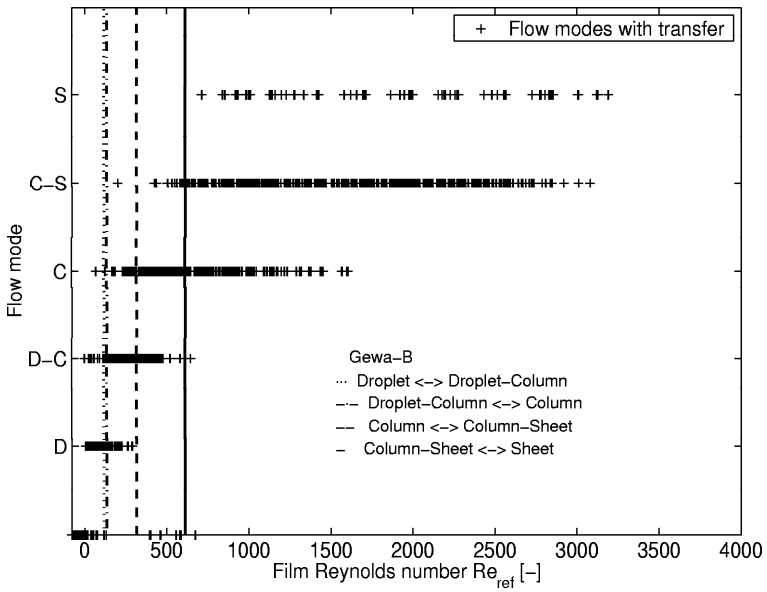

Figure 5.15: Observed flow modes in heat transfer conditions and adiabatic predictions for the Gewa-B tube.

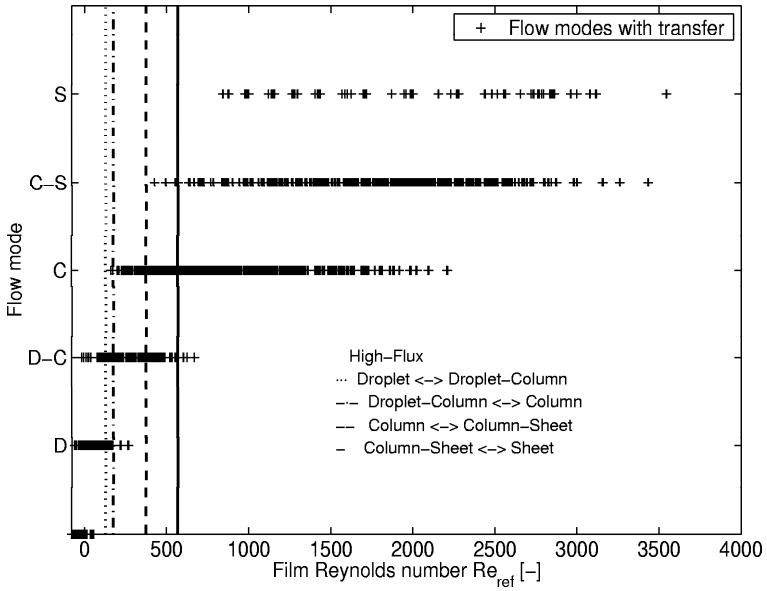

Figure 5.16: Observed flow modes in heat transfer conditions and adiabatic predictions for the High-Flux tube.

5.5 Flow mode and heat transfer

The influence of the flow modes on the heat transfer is illustrated in figures 5.17 and 5.18. The measured heat transfer coefficient is given as a function of the film Reynolds number for the plain tube and a enhanced tube, the Turbo-BII HP with a nominal heat flux. The observed flow modes are given by the different symbols. The heat transfer coefficient will be shown in chapter 6. Two main regions could be observed: one region number where the heat transfer coefficient present a weak variation versus the film Reynolds number and one region for low film Reynolds numbers where the heat transfer coefficient fall off rapidly. In each of these regions, different flow modes are observed with no significant impact on the general trend. The transition between these two regions was also not found to occur at a specific flow mode. Similar behaviors were observed for all the other test conditions. For these reasons, and as a first approach, the observed flow modes are not taken into account in the further discussions.

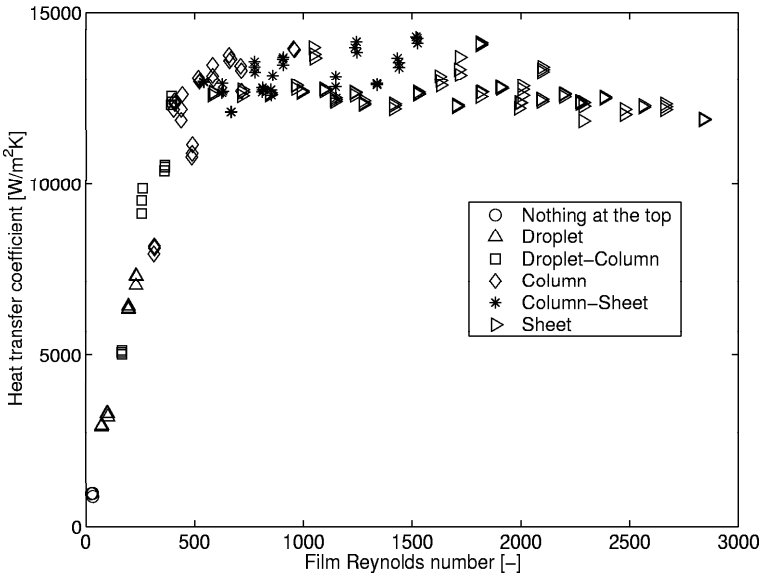

Figure 5.17: Heat transfer coefficient and observed flow modes for plain tube (tube pitch: $22.3mm$ and $q_{plateau} = 36kW/m^2$).

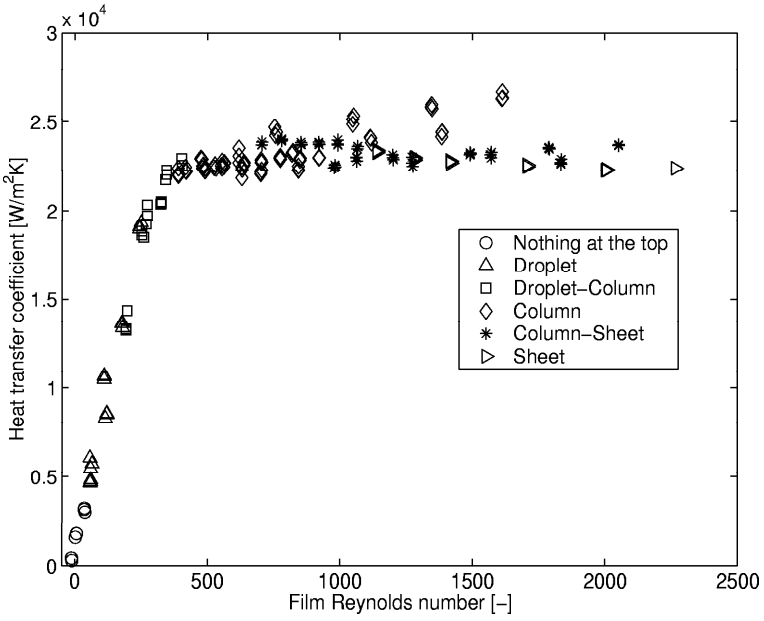

Figure 5.18: Heat transfer coefficient and observed flow modes for Turbo-BII HP (tube pitch: $25.5mm$ and $q_{plateau} = 39kW/m^2$).

5.6 Conclusions

The different flow modes that occur when a liquid is flowing on horizontal tubes have been presented. Observations and measurements of the different transitions in adiabatic conditions were obtained for several types of tubes and three different liquids (water, glycol and 50%/50% water-glycol mixture) on the small adiabatic test facility. Correlations to predict the transition film Reynolds number between the different flow modes were presented. In these relations, the transition film Reynolds number was linked to the modified Gallileo number. Flow modes have been also observed with the refrigerant R-134a in the new large test facility. Without heat transfer, the agreement with the predictions was satisfying except for the column-sheet to/from sheet transition. Under heat transfer conditions, the transitions between the flow modes were found to occur at higher film Reynolds numbers than in adiabatic conditions. Finally, no real influence of the flow mode on the heat transfer coefficients was found and hence flow mode will not be taken into account account in the heat transfer prediction method.

Chapter 6

Heat Transfer Measurements

In this chapter, first the method used to determine the heat transfer coefficient locally on the outside of the tubes during falling film evaporation is described and then a propagation of error analysis is performed. Next, the test conditions are given and finally the results of the heat transfer measurements are presented.

6.1 Data Reduction

Using water flowing through the tubes to evaporate the refrigerant on the outside of the tubes, the water undergoes a temperature change while the phase changing refrigerant stays at the same saturation temperature. This produces a change in local heat flux as the temperature difference between the water and the refrigerant decreases along the length of the tubes. In previous published studies, only the inlet and outlet temperature of the water have been measured. This means they have all assumed a linear water temperature profile as function of tube length, subsequently implying a constant heat flux, to obtain a mean heat transfer coefficient for each tube rather than local values.

In this study, the internally mounted thermocouples measuring the water temperature within the tubes in the axial direction permit the determination of the water temperature profile as a function of the distance along the tubes:

$$T_{wat} = f(x) \tag{6.1}$$

As shown in chapter 4 the local heat flux on the outside of the tube can be derived from the water temperature profile as

$$q_o = \frac{\dot{m} c_{p,wat}}{\pi D_o} \frac{\mathrm{d}T_{wat}}{\mathrm{d}x} \tag{6.2}$$

where $\dot{m}$ is the mass flow rate and $c_{p,wat}$ the specific heat of water. The local overall heat transfer coefficient U_o can be calculated from the heat flux

as

$$U_o = \frac{q_o}{T_{wat} - T_{sat}} \tag{6.3}$$

with the saturation temperature of the refrigerant T_{sat} and the bulk temperature of the water T_{wat}. The heat transfer coefficients are linked as shown before by

$$\frac{1}{U_o} = \frac{1}{\alpha_o} + \frac{1}{\alpha_i}\left(\frac{D_o}{Di}\right) + r_w \tag{6.4}$$

where α_o is the boiling side, α_i is the water side heat transfer coefficient and r_w the thermal resistance of the copper tube given by

$$r_w = \frac{D_o}{2\lambda_{cop}} \ln\left(\frac{D_{or}}{D_i}\right) \tag{6.5}$$

D_i is the inside diameter of the tube, D_{or} the outside root diameter, and λ_{cop} the thermal conductivity of the tube material.

The inside heat transfer coefficient α_i is obtained from the Gnielinski correlation with a corrective multiplier.

$$\alpha_i = C_i \alpha_{gni} \tag{6.6}$$

The determination of this corrective multiplier C_i, which includes influences of the used experimental setup, was described earlier in chapter 4.

With the help of equations 6.2 to 6.6, the heat transfer on the outside of the tube can be calculated from a measured water temperature profile, the water mass flow rate, and the saturation temperature of the refrigerant. For a given water temperature profile, the outside heat transfer coefficient can be calculated at any location along the axis of the tube. However, in this study the coefficient α_o is only evaluated at the midpoint of every tube where the mean of two thermocouples gives T_{wat} and where the most accurate measurement can be made as the heat flux is calculated from the derivative of the temperature profile. This local heat transfer coefficient corresponds to that for the outside perimeter of the tube at diameter D_o.

The amount of liquid refrigerant evaporated on the outside of one tube is derived from the local heat flux given by equation 6.2 and the latent heat h_{LV} of the refrigerant. With the assumption that the liquid on the tube is at its saturation condition, the mass flow of refrigerant evaporating on one tube locally is calculated by an energy balance on a differential element

$$(2\Gamma_{top} - 2\Gamma_{bot}) h_{LV} \mathrm{d}x = q_o \pi D_o \mathrm{d}x \tag{6.7}$$

where 2Γ is the total mass flow rate on the tube per unit width and Γ is the flow rate on one side of the tube per unit length of tube falling on top

of the tube or leaving at the bottom, respectively. With this definition, the film Reynolds number on the tube is

$$Re_{film} = \frac{4\Gamma}{\mu_L} \tag{6.8}$$

and is equivalent to that on a vertical plate in the Nusselt Theory.

For the measurements with liquid overfeed, the film Reynolds number of the liquid arriving on the first tube is obtained from the measured mass flow rate (coriolis meter) and the tube length assuming that the refrigerant is at saturation conditions. The amount of liquid lost by evaporation on the first tube is calculated with 6.7 is substract to obtain the film Reynolds number at the bottom of the first tube. The film Reynolds number of the liquid falling on the second tube is set to the value leaving the first and so on. This means an ideal one-dimension downward flow is assumed on the tube rows. All the liquid flows from one tube to the next without leaving the tube row.

6.2 Measurement Accuracies

As shown in the previous section, the experimentally obtained external heat transfer coefficient α_o is mainly a function of the saturation temperature T_{sat}, the water temperature T_{wat}, the heat flux q_o and the internal heat transfer coefficient α_i. The influence of parameters like the tube dimensions and geometrical properties of the experimental setup have been found to be of minor importance and are not considered in this error analysis. Thus:

$$\alpha_o = f(T_{sat}, T_{wat}, q_o, \alpha_i) \tag{6.9}$$

The saturation temperature is calculated from the pressure measured by one pressure transducer above the tube row and one below the tube row with the assumption that the vapor is at saturation. The absolute error of both pressure transducers is $1kPa$. The measured variation in pressure during the data acquisition is always smaller than the absolute error of the transducers. The measured pressure difference of the two transducers is in most of the measurements also smaller than $1kPa$. With refrigerant R-134a, a change in saturation pressure of $1kPa$ corresponds to a change in saturation temperature of $0.05K$. To cover this temperature range, the error on the saturation temperature is estimated to be within $\Delta T_{sat} = \pm 0.03K$ as it is measured by two transducers $= \pm 0.05/\sqrt{2}$.

The water temperature in the middle of the tube is evaluated from the polynomial fit of the water temperature profile. As a second order polynomial is used for the fit of the six thermocouples at three axial locations, the fit is exactly the mean value of the two thermocouples at every location. In other words, the water temperature calculated with the

polynomial in the middle of the tube is the same as the mean value of the two thermocouples at this position. The uncertainty of single thermocouple after calibration is $\pm 0.03K$. As it is measured by two transducers, the error of the water temperature is consequently estimated to be within $\Delta T_{wat} = \pm 0.03/\sqrt{2}K = \pm 0.02K$, as it is measured by two thermocouples at the same location.

According to equation 6.2, the *heat flux* is calculated from the derivative of the water temperature profile. Alternatively, it can be shown that for the specific case of a second order polynomial fit through the thermocouples at three equidistant locations, the heat flux in the middle of the tube can also be calculated by

$$q_o = \frac{\dot{m} c_{p,wat}}{\pi D_o L} (T_{wat,in} - T_{wat,out}) \tag{6.10}$$

where $T_{wat,in}$ is the mean value of the two thermocouples at the inlet, $T_{wat,out}$ the mean value of the two thermocouples at the outlet and L the distance between these two locations. This means that the local heat flux in the middle of the tube (equation 6.2) is exactly the mean value over the tube length (equation 6.10).

The uncertainty of the local heat flux Δq_o can now be estimated for this case as follows

$$\Delta q_o = \sqrt{\left(\frac{\partial q_o}{\partial \dot{m}} \cdot \Delta \dot{m}\right)^2 + \left(\frac{\partial q_o}{\partial T_{wat,out}} \cdot \Delta T_{wat,out}\right)^2 + \left(\frac{\partial q_o}{\partial T_{wat,in}} \cdot \Delta T_{wat,in}\right)^2} \tag{6.11}$$

Evaluation of the partial derivatives and substitution of the temperature uncertainties by $\Delta T_{wat} = \Delta T_{wat,out} = \Delta T_{wat,in}$ leads to

$$\Delta q_o = \sqrt{\left(\frac{c_{p,wat}}{\pi D_o L} (T_{wat,in} - T_{wat,out}) \cdot \Delta \dot{m}\right)^2 + 2\left(\frac{\dot{m} c_{p,wat}}{\pi D_o L} \cdot \Delta T_{wat}\right)^2} \tag{6.12}$$

The uncertainty of the total water mass flow is given by equation 3.1, which gives a relative value smaller than 0.18% for all measurements. During the measurements, the total water mass flow is split in five parallel circuits going to the test section as mentioned before. To assure a uniform distribution to the sub-circuits, all five are equipped with a rotameter. With an ideal distribution, the absolute error of the total mass flow can be divided by the number of circuits. To account for maldistribution the absolute uncertainty of the water flowing in one tube is assumed to be the same as the one of the total mass flow. That means that the relative uncertainty of the water flow rate in one tube is 0.9% (that is five times more). The given relative uncertainty of the float meters was not utilized as they are

used for flow rate comparison (the systematic error is removed). This value in any case is in the same order as they are class one measurement devices (uncertainty=1% of the full scale). With this assumption, the uncertainty of the heat flux is mainly determined by the second summand in equation 6.12, the uncertainty of temperature measurement.

According to equation 6.6 the internal heat transfer coefficient α_i is calculated from the Gnielinski correlation and a corrective multiplier C_i. The accuracy of the internal heat transfer coefficient is mainly determined by the accuracy of this corrective multiplier. The relative uncertainty in the value of C_i corresponds approximately to the relative uncertainty of the internal heat transfer coefficient. The values of C_i, the absolute error and the relative error determined in chapter 4 for the four tested tubes are summarized in table 6.1.

Tube	C_i [-]	ΔC_i [-]	$\Delta C_i/C_i$ [%]
Plain Tube	1.27	0.1	7.9
Turbo-BII	4.03	0.2	5.0
Gewa-B	4.09	0.2	4.9
High-Flux	4.22	0.2	4.7

Table 6.1: Corrective multipliers for internal heat transfer coefficient α_i with absolute and relative errors.

Finally, the accuracy of the external heat transfer coefficient $\Delta\alpha_o$ is estimated based on equation 6.9 by

$$\Delta\alpha_o = \left[\left(\frac{\partial\alpha_o}{\partial T_{wat}}\cdot\Delta T_{wat}\right)^2+\left(\frac{\partial\alpha_o}{\partial T_{sat}}\cdot\Delta T_{sat}\right)^2+\left(\frac{\partial\alpha_o}{\partial q_o}\cdot\Delta q_o\right)^2 + \left(\frac{\partial\alpha_o}{\partial\dot{m}}\cdot\Delta\dot{m}\right)^2+\left(\frac{\partial\alpha_o}{\partial C_i}\cdot\Delta C_i\right)^2\right]^{1/2} \quad (6.13)$$

The values of the mean relative errors in local heat flux for all principal tests at three different heat fluxes are presented in table 6.2. The mean relative errors in local heat transfer coefficient are given in table 6.3. (no measurements were made for the High Flux tube at the lowest heat flux range).

The uncertainty in local heat flux and local heat transfer coefficient decreases with increasing heat flux. For a higher heat flux, the temperature differences become larger which means that the relative error of a temperature difference decreases for a constant absolute error in the temperature measurement.

The above propagation of error analysis has been applied to each experimental data point. For all measurements, the experimental uncertainty

	$\Delta q_o/q_o$		
Tube	q_o $20kW/m^2$	q_o $40kW/m^2$	q_o $60kW/m^2$
Plain Tube	4.6%	4.7%	4.7%
Turbo-BII	7.2%	3.3%	3.9%
Gewa-B	7.4%	2.5%	5.6%
High-Flux	$\times\times$	7.0%	5.2%

Table 6.2: Mean relative errors of the local heat fluxes.

	$\Delta \alpha_o/\alpha_o$		
Tube	q_o $20kW/m^2$	q_o $40kW/m^2$	q_o $60kW/m^2$
Plain Tube	20.4%	16.9%	15.0%
Turbo-BII	19.9%	8.8%	7.6%
Gewa-B	16.6%	7.4%	8.7%
High-Flux	$\times\times$	24.0%	14.8%

Table 6.3: Mean relative errors of the local heat transfer coefficients.

of the heat transfer coefficient α_o is on average $\pm 14\%$, with 90% of points having an uncertainty less than $\pm 22\%$. The plain tube has higher values because the inside is smooth without heat transfer enhancement and hence creates a larger uncertainty on α_o; the High-Flux tube has higher values because its boiling performance is so high (α_o is very large). The uncertainty comes mainly from the water temperature inside the tube and the C_i coefficient.

The uncertainty on the refrigerant flow rate at the top of the tube row is given by equation 3.1, which gives a relative value smaller than 0.17% and a maximum absolute value of $0.3g/s$ for all the measurements. Under heat transfer conditions, all the liquid was observed to flow from tube to tube (no liquid was leaving). The presence of nucleate boiling in the film was a stabilizing factor.

6.3 Test conditions

Four commercially available tubes were tested at three different tube pitches: a Turbo-BII HP provided by Wolverine Tube Inc, a Gewa-B tube provided by Wieland-Werke AG, a porous coated or High-Flux tube provided by UOP Inc. and a plain tube. All have a nominal external diameter of 19.05mm. The tube pitches center-to-center were: $22.3mm$, $23.9mm$, and $25.5mm$ (which represent spacings between the tubes of 3.2, 4.8 and 6.4mm). During the measurements, the heat flux was kept constant. The uncertainty on the external heat transfer coefficient was calculated and displayed continuously

on the measurements computer. The water flow rate and temperature to achieve one heat flux were adjusted to minimize this uncertainty.

The refrigerant liquid overfeed rate was decreased stepwise. The temperature at the inlet of the distributor was controlled with the liquid cooler before the pump. A subcooling of $0.5K$ was maintained to avoid evaporation of the liquid when passing through the foam layers of the distributor. With this, no bubbles were visible at the exit of the distributor.

The nominal heat fluxes were 20, 40, and $60kW/m^2$ for the three enhanced tubes. The matrix of the principal tests is given in table 6.4. The tests were run with refrigerant R-134a at a nominal saturation temperature of $278K$ (5°C).

Tube pitch	Plain Tube q_o $[kW/m^2]$	Turbo-BII q_o $[kW/m^2]$	Gewa-B q_o $[kW/m^2]$	High-Flux q_o $[kW/m^2]$
$22.3mm$	20/36/53	25/40/60	25/37/53	37/54
$23.9mm$	20/37/55	25/38/58	24/35/53	38/53
$25.5mm$	19/34/58	26/42/61	25/39/51	36/54

Table 6.4: Test matrix for the measurements.

It will be shown in chapter 7 that nucleate boiling was present during the measurements. The nucleate boiling performance can be influenced by the thermal history of the surface. Typically the thermal performance presents an hysteresis versus heat flux. The test facility was run at high heat flux ($q_o > 70kW/m^2$) at startup to take that into account and thus define clearly the measurements conditions.

6.4 Falling film evaporation results

6.4.1 Plain tube

Figure 6.1 shows the heat transfer coefficient for the plain tube at different heat fluxes as a function of the film Reynolds number and for one tube pitch. The results presented correspond to the even tubes. Measurements from the even and the odd tubes are treated separately because for one nominal heat flux for the bundle, the water temperatures at the inlet of the even and the odd tubes are different as the water circuit comprises two passes. The heat transfer coefficient increases rapidly with the film Reynolds number to an upper limit (a function of the nominal heat flux) and then changes slightly for large Reynolds numbers. In the first region, the heat flux is lower than the nominal specified one. In the second region (for large film Reynolds number), the heat transfer coefficient increases with the nominal heat flux from 10 to $15kW/m^2K$ when the nominal heat flux increases from $19kW/m^2$ to $56kW/m^2$. The film Reynolds number where the heat transfer coefficient starts to fall off increases with the nominal heat flux from a value of 300 for

the low heat flux to 550 for the high heat flux. The same trend has been observed for the other tube pitches.

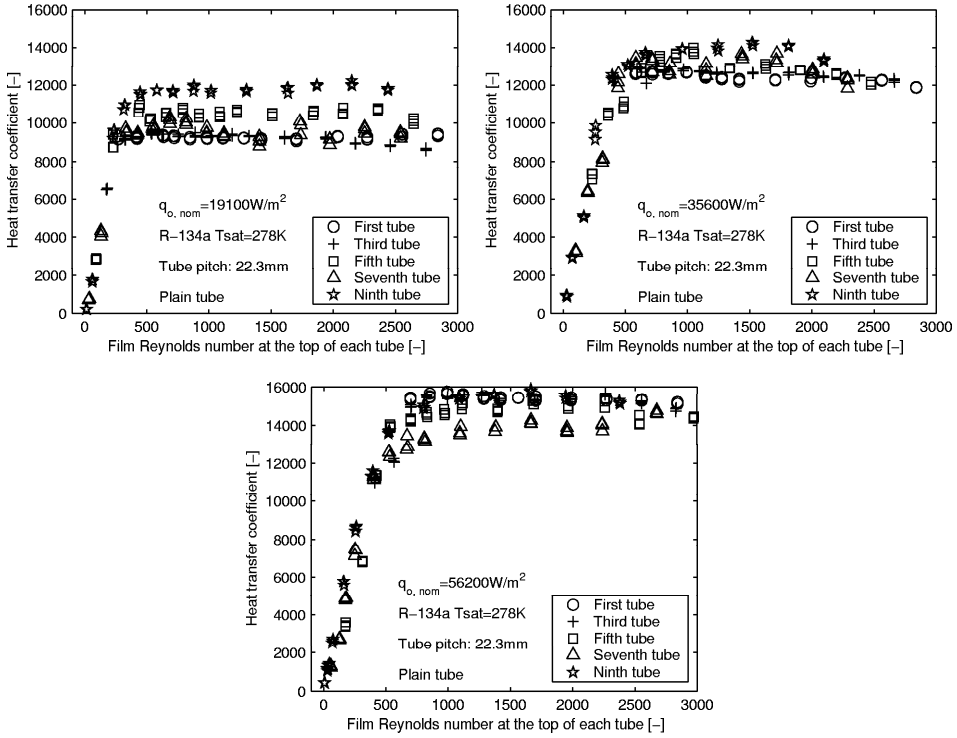

Figure 6.1: Heat transfer coefficient for the plain tube, tube pitch=22.3mm, heat fluxes:19, 36, and $56kW/m^2$.

6.4.2 Turbo-BII HP tube

Figure 6.2 shows the heat transfer coefficient for the Turbo-BII HP tube at different heat fluxes as a function of the film Reynolds number and for one tube pitch. Similar behavior as the plain tube is observed. The heat transfer coefficient for large film Reynolds number decreases from $35kW/m^2K$ to $20kW/m^2K$ when the heat flux increases from $22kW/m^2$ to $55kW/m^2$. The limit of the heat transfer coefficient fall off, is lower for this enhanced tube than for the plain tube. This limit is at a film Reynolds number lower than 400 even for the high heat flux.

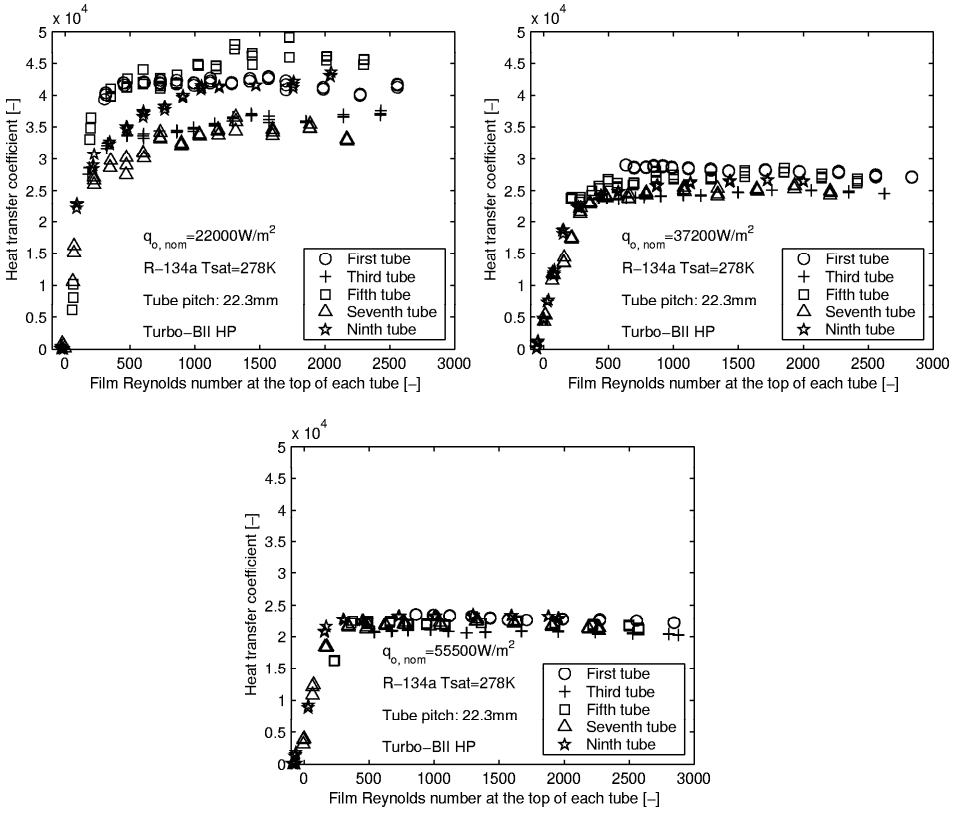

Figure 6.2: Heat transfer coefficient for the Turbo-BII HP tube, tube pitch=22.3mm, heat fluxes: 22, 37, and $56kW/m^2$.

6.4.3 Gewa-B tube

Similarly, figure 6.3 shows an example of measurements for the Gewa-B tube. The general variation of the heat transfer coefficient versus the film Reynolds number is similar than for the plain and the Turbo-BII HP tubes: a uniform part for the large film Reynolds numbers and a rapid decrease at low flow rate. The variation of the heat transfer coefficient (in the uniform part) versus the nominal heat flux is less pronounced for this tube. It decreases from $25kW/m^2K$ at $20kW/m^2$ to $20kW/m^2K$ at $50kW/m^2$. The limit of the heat transfer coefficient fall off is similar than the one for the Turbo-BII HP tube.

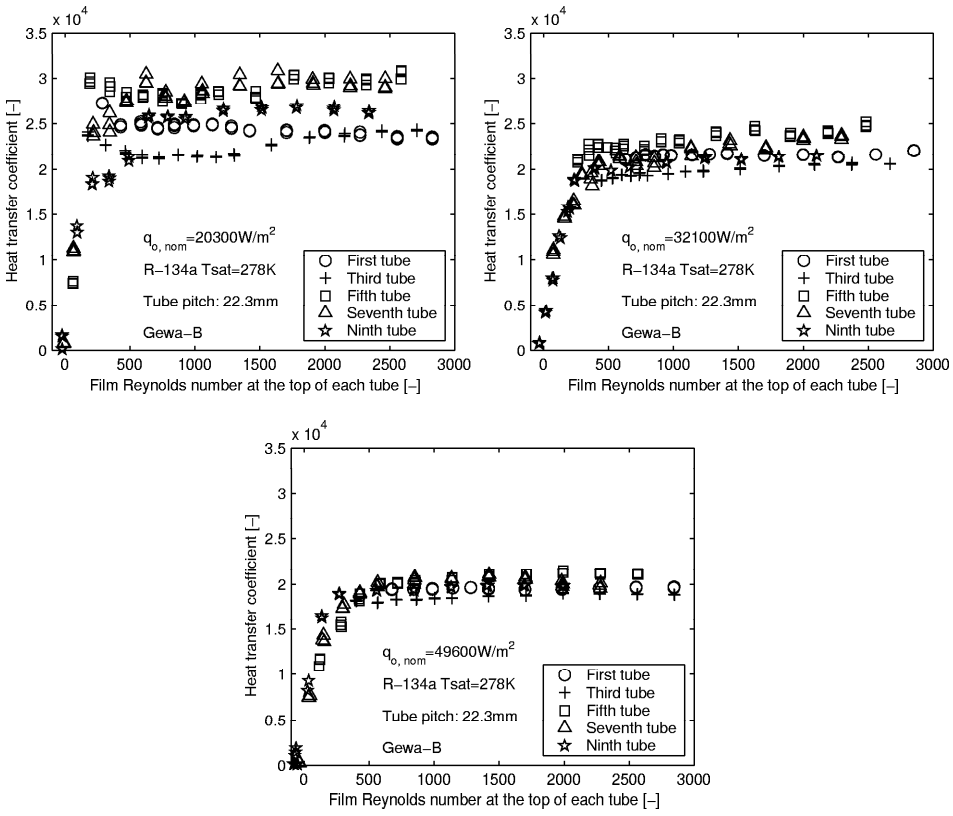

Figure 6.3: Heat transfer coefficient for the Gewa-B tube, tube pitch=22.3mm heat fluxes: 20, 32, and $50kW/m^2$.

6.4.4 High-Flux tube

Finally, figure 6.4 shows an example of measurements for the High-Flux tube. Tests have been performed at low heat flux but the high heat transfer coefficient lead to important measurements errors and the results have not been taken into account. The general trend of the heat transfer coefficient versus the film Reynolds number is similar for this tube than for the three others ones. The heat transfer performance is globally higher: more than $50kW/m^2K$ compared to 20 to $40kW/m^2K$ for the two other enhanced tubes. A decrease of the heat transfer coefficient versus heat flux is also observed from 60 to $50kW/m^2K$ when the heat flux is equal to respectively 50 and $73kW/m^2$.

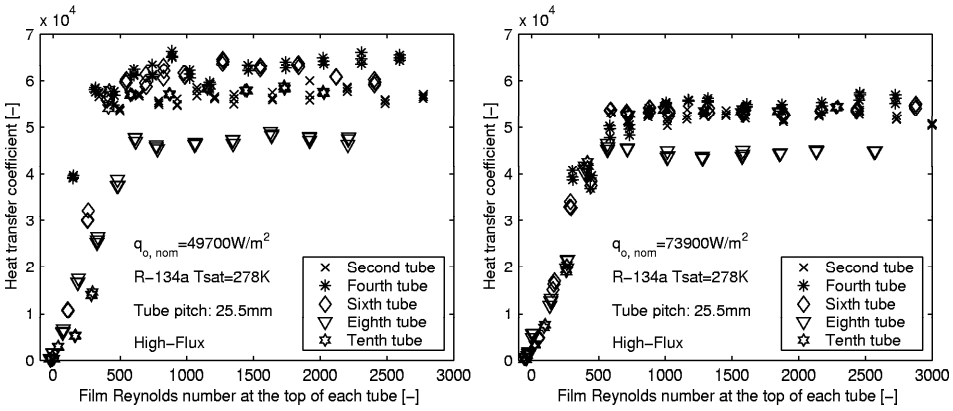

Figure 6.4: Heat transfer coefficient for the High-Flux tube, tube pitch=25.5mm, heat fluxes: 50, 73 kW/m^2.

6.5 Measurements in pool boiling conditions

As a reference for each tube, measurements were made in pool boiling conditions. The test section was filled with refrigerant at $278K$ (the liquid level was set to be around $20mm$ above the test tube). Tests were conducted from high heat flux to low heat flux, decreasing stepwise the heat flux and with two different samples of tube. Data for each type of tube were correlated in the following type of equation:

$$\alpha_o = aq_o^b \tag{6.14}$$

Results of these pool boiling measurements are shown in figure 6.5 and the coefficients a and b are given in table 6.5

Comparisons between the measurements and relations from chapter 2 are shown in figure 6.6 and 6.7.

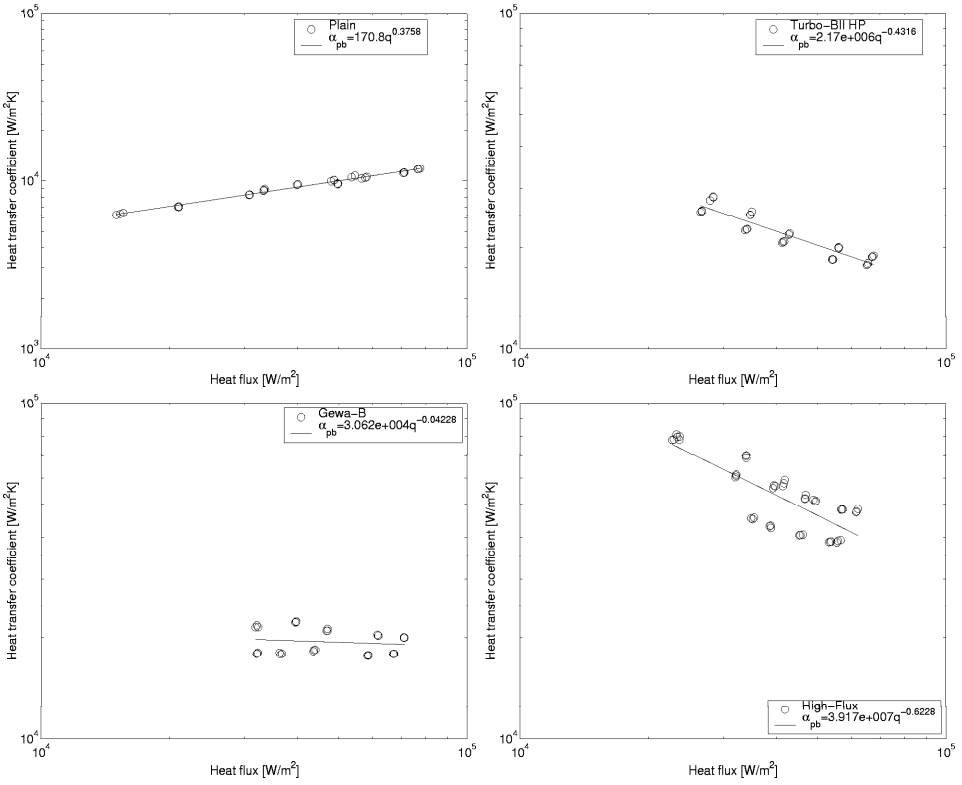

Figure 6.5: Measurements in pool boiling conditions for R-134a at $278K$.

Tube	a	b
Plain	171	0.376
Turbo-BII	$2.17{\cdot}10^6$	-0.432
Gewa-B	$3.06{\cdot}10^4$	-0.042
High-Flux	$3.92{\cdot}10^7$	-0.623

Table 6.5: Coefficients for the pool boiling relation.

The present plain tube is identical to the one tested by Thome and Robinson [THOM03] and the results are similar. The copper plain tube has a relatively high surface roughness and the heat transfer coefficient is generally higher than the other data at low heat flux while at high heat flux, the measured values corresponds to the prediction of the Gorenflo correlation. Figure 6.7 shows a comparison for the Turbo-BII HP and the High-Flux tubes. For the Turbo-BII HP, the testing range is different and it seems that this tube presents lower heat transfer coefficients at high heat flux explaining the difference in trend. For the High-Flux tube, the results from McNeil et al. [MCNE02] in terms of enhancement factor (from the current

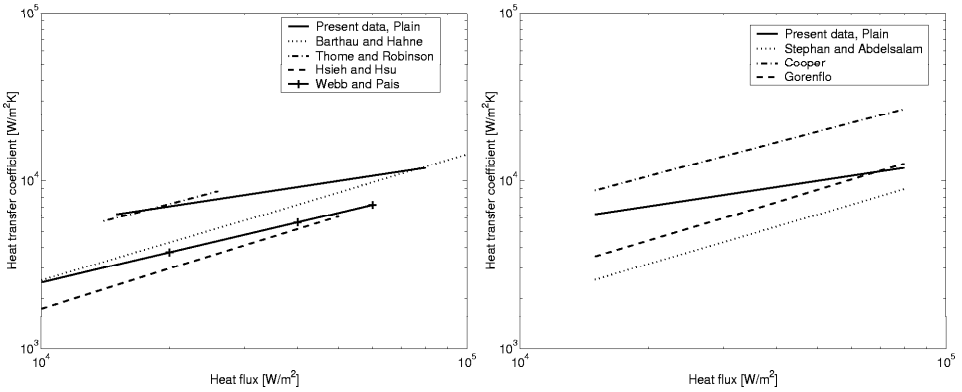

Figure 6.6: Comparison in pool boiling conditions for the plain tube, mean measured roughness Ra=0.8μm and Rp=2μm R-134a at 278K.

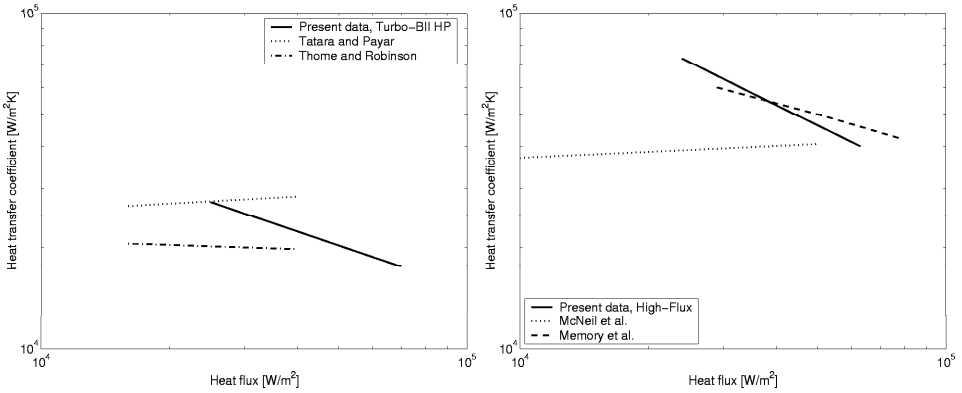

Figure 6.7: Comparison in pool boiling conditions for the Turbo-BII HP and High-Flux tubes for R-134a at 278K.

plain tube) gives significant differences while the ones from Memory et al. [MEMO95a] present a better agreement.

6.6 Onset of film breakdown measurements

During falling film evaporation, the liquid flowing around a tube can breakdown if the liquid flow rate is not sufficient. This limit is a function of the heat flux on the tube. More liquid is necessary to avoid dryout at higher heat flux. As no criterion is available for the enhanced tubes, tests were made to obtain this limit as a function of the heat flux. The visual criteria to define the film breakdown was: the film breaks when there is a stagnation point at 90° from the top dead center. The procedure was to first set a

heat flux, then decrease the liquid flow rate from high values until the film breaks. The film breakdown on the enhanced tubes was difficult to define accurately. For those tubes, the liquid can flow in-between the fins or in the porous layer for the High-Flux tube. The result of these measurements are shown in figure 6.8.

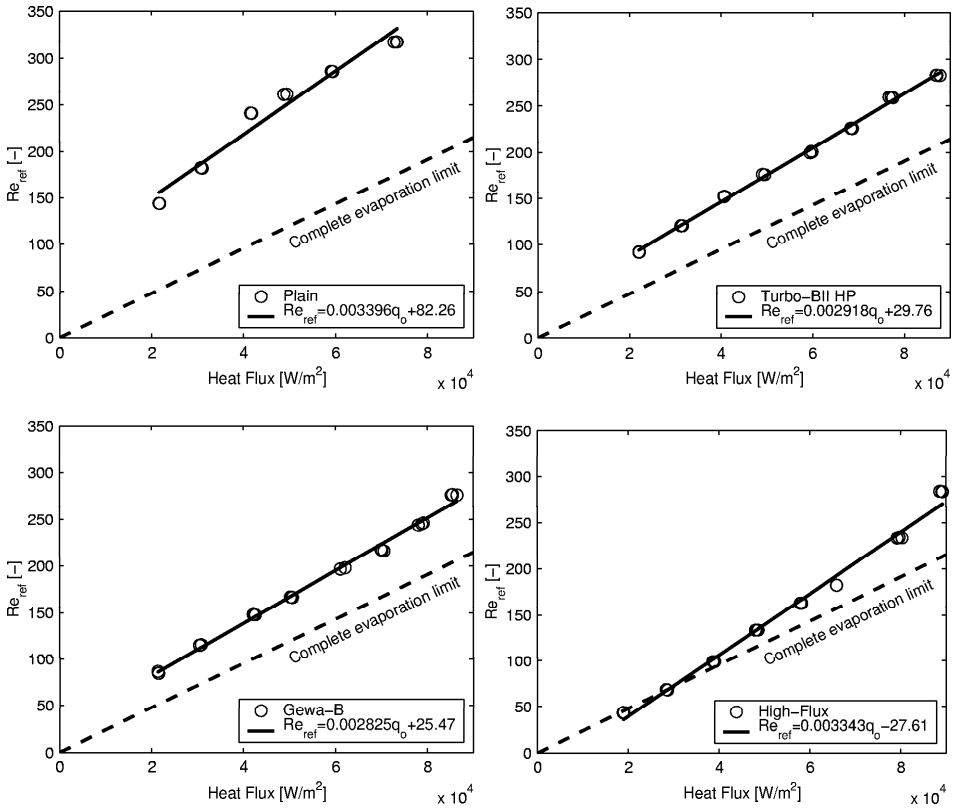

Figure 6.8: Film breakdown Reynolds number (at the top of the tube) as a function of heat flux for each tube.

The dash line corresponds to the complete evaporation limit or what is the minimum flow rate to achieve a given heat flux if all the liquid is evaporated on the tube (conduction and radiation from the dry areas are neglected). It is also the amount of liquid evaporated on the tube. The film breakdown Reynolds number was found to be a linear function of the heat flux:

$$Re_{ref,dryout} = cq_o + d \tag{6.15}$$

The film breakdown Reynolds number increases with heat flux for all the tubes and is higher for the plain tube than for the enhanced ones. It is notable that for the Turbo-BII HP and the Gewa-B tubes, the distance between the film breakdown line and the complete evaporation line presents

Tube	c	d
Plain	$3.39 \cdot 10^{-3}$	82.3
Turbo-BII	$2.92 \cdot 10^{-3}$	29.8
Gewa-B	$2.83 \cdot 10^{-3}$	25.5
High-Flux	$3.34 \cdot 10^{-3}$	-27.6

Table 6.6: Coefficients for the film breakdown relations.

a weak variation versus heat flux. This distance corresponds to film Reynolds at the bottom of the tube. In other words, the film breakdown occurs for these two tubes at a constant Reynolds number at the bottom of the tube. This value is independent of the heat flux. Finally, the High-Flux tube can sustain high heat flux before film breakdown. On this type of tube, the boiling induces smaller bubbles in the film due to the porous surface. The liquid film is less disturbed and the film breakdown is delayed.

With equation 6.15, it is possible to calculate the breakdown film Reynolds number on a tube as a function of the heat flux. When applying this equation in adiabatic conditions (q_o=0), the result is $Re_{ref,dryout}$=d. For the plain tube, this value is 82. The film breakdown model from El-Genk and Saber (equation 2.35) with refrigerant R-134a at $278K$ and a contact angle of 25° give a comparable value of 81.8.

6.7 Conclusions

Falling film evaporation measurements have been made with four different types of tubes at three tube pitches of 22.3, 23.9 and $25.5mm$ for heat fluxes from 20 to $70kW/m^2$. The general trend is that the heat transfer coefficient remains constant when decreasing the film flow rate at constant heat flux until a the onset of dryout is reached and then decreases rapidly towards a value of zero at complete dryout. The heat transfer coefficient is strongly dependant on the heat flux. All the graphs of the measurements are shown in the Appendix A.

Single tube pool boiling measurements have also been performed for each type of tube and tube specific correlations for the heat transfer coefficient in pool boiling conditions have been presented. They will be used in the following chapter for predicting the heat transfer coefficient in falling conditions.

Film breakdown has been observed on the tubes and the corresponding film Reynolds number measured. An empirical expression was then proposed to predict the film Reynolds number at which the film breakdown occurs as a function of the heat flux (onset of dryout). This film breakdown Reynolds number is linked to the rapid decrease of the heat transfer coefficient during falling film evaporation as dry patches transfer little heat. It will be found

to be an important parameter in predicting heat transfer in falling film evaporation.

Chapter 7

Heat transfer prediction methods

In this chapter, the falling film evaporation results are treated to obtain a prediction of the heat transfer coefficient for each tube. A prediction method in two parts is developed.

7.1 General description of the results

For a given tube, the parameters that might have an influence on the falling film evaporation heat transfer coefficient are:

1. The quantity of liquid flowing on the top of the tube characterized by the liquid refrigerant Reynolds number Re_{ref}. The liquid flow mode also defined by the film Reynolds number could be an additional parameter (droplet, columns or sheet).

2. The thermal load on the tube may influence the heat transfer, especially when boiling occurs in the liquid film. As it was shown in section 6.5, the heat transfer coefficient is only a function of the heat flux in pool boiling conditions.

3. The tube pitch: in-between the tubes, the gravity force accelerates the liquid. The impingement velocity at the top of the tubes thus increases with the spacing. The tube pitch has also an indirect influence through the liquid flow modes.

4. The onset of film breakdown: when the film breaks up, dry patches appear on the tube and create areas where there is no evaporation and thus nearly no heat transfer. These patches may be intermittent or remain dry. The heat transfer coefficient on the tube thus decreases.

5. The tube position in bundle: considering two tubes with all the above parameters identical but the position of the tubes different, viz. one is situated at the top of the tube array, in position one or two and the other tube is situated at the bottom of the tube array, in position eight or nine for example. The heat transfer coefficient between these two tubes could be different due to the difference of the liquid flow "history". This is the real bundle effect because it is not only a function of the parameters of one single tube.

The influence of all the parameters above is analyzed based on the measurements. For this, the results of one day of measurements are shown in figure 7.1, which corresponds to one type of tube, one tube pitch and one nominal heat flux or more exactly one water temperature and one water flow rate at the inlets of the five two-pass circuits.

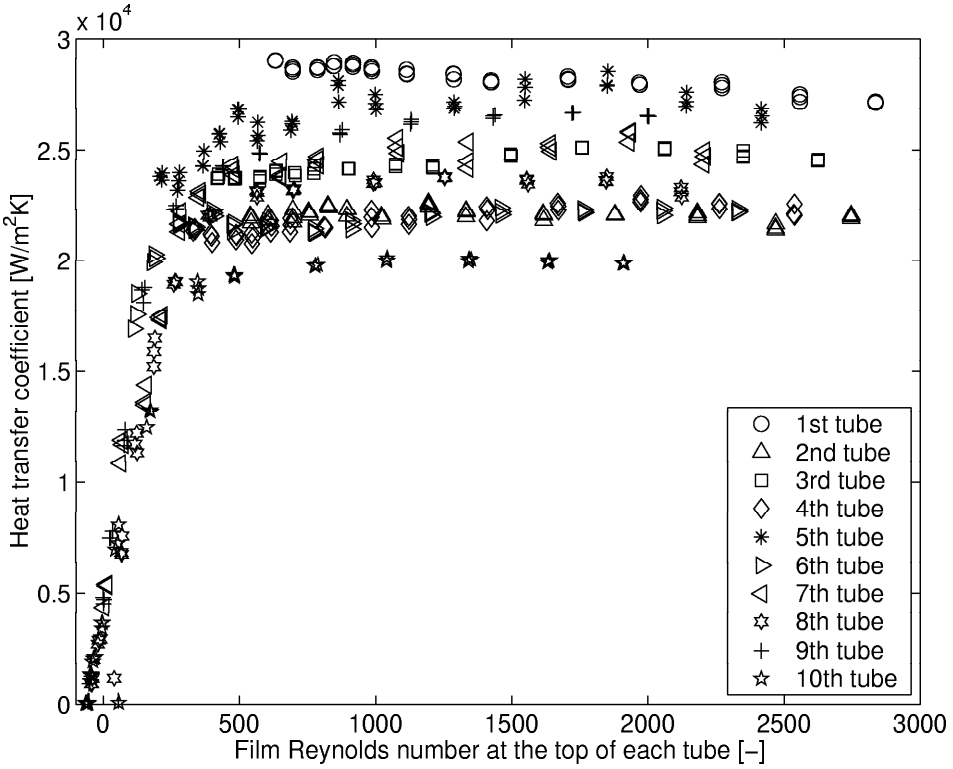

Figure 7.1: Heat transfer coefficient as a function of film Reynolds number for Turbo-BII HP (tube pitch=22.3mm and nominal heat flux=$40kW/m^2$)

This particular case is for the Turbo-BII HP at $q_o = 40kW/m^2$ with a tube pitch of $22.3mm$. The amount of liquid refrigerant flowing at the top of the tube array is changed from $200g/s$ to $45g/s$ (Re_{ref} from 2800

to 600) in 14 steps. For each step, three acquisitions are made explaining the array of three nearly identical points for every condition (demonstrates good reproducibility of the data points). In general and for one tube, the heat transfer coefficient presents a weak variation versus the liquid flow rate at the top of the tube when the Reynolds number is high enough (>500 here). This heat transfer coefficient is for example around $28kW/m^2K$ for the top tube and around $22kW/m^2K$ for the second and the fourth tubes. For lower Re_{ref}, the heat transfer coefficient decreases rapidly with the flow rate towards zero (complete dryout of the tube at which only natural convection to the vapor is present). It could be noted that there are points with a negative Reynolds number; this is due to accumulated error in the heat balance over the ten tubes to determine the flow rate of the remaining liquid. For the minimum liquid flow rate (Re_{ref}=600), an error on the heat flux of 4% gives an absolute error on the Reynolds number of 24, for example.

7.2 Falling film heat transfer coefficient with partial dryout

As seen above, there is a region in term of Reynolds number where the heat transfer coefficient decreases rapidly with the liquid overfeed. The evaporation process and/or the low liquid overfeed evoke a dryout or film breakdown phenomenon. It is clear that if there is not enough liquid to be evaporated, the heat transfer coefficient decreases as the measurements correspond to a mean heat transfer coefficient over the perimeter of the tube. For example, when the conditions for one tube are such that all the liquid is evaporated on the upper half of the tube and if the heat transfer coefficient in this half tube is supposed equal to the one in fully wet conditions (corresponding to horizontal part in figure 7.1), the resulting heat transfer coefficient for the entire perimeter of the tube will be one half of the nominal one. This explains why the heat transfer coefficient decreases with Reynolds number with partial dryout and also that the relation should be approximately linear in the region where all the liquid is evaporated on a fraction of the tube perimeter.

The parameter to be determined now is the threshold Reynolds number $Re_{ref,threshold}$ or the point where the heat transfer coefficient starts to sharply decrease. As mentioned above, it is linked to film breakdown and dryout treated in section 6.6. In this part, the film Reynolds number at which the film broke in the middle of the circumference of the tube has been correlated with the heat flux. The upper half of the tube was fully wet while the bottom half presented dry patches.

This dryout Reynolds number is a minimum limit for the threshold Reynolds number because at this value, there are permanent dry patches with poor heat transfer performance and the heat transfer coefficient for the

tube is thus already in the decreasing part.

On the other hand, at these dryout conditions ($Re_{ref} = Re_{ref,dryout}$) the maximum area occupied by the dry patches is one half of the tube surface because of the criteria adopted to define dryout. The percentage of dry surface is in fact less than 50% because there is all the time liquid at the bottom of the tube at dryout conditions as shown in figure 6.8. This liquid maintains wet areas on the bottom half of the tube. A linear relation between the percentage of the tube surface that is dry and the film Reynolds number for a given heat flux would lead to a completely wet surface if the film Reynolds number is equals to two times $Re_{ref,dryout}$. For all the falling film evaporation measurements, a good estimation of onset of dryout threshold Reynolds number was found to be this upper limit:

$$Re_{ref,threshold} = 2Re_{ref,dryout} \tag{7.1}$$

In this relation, all the Reynolds numbers correspond to the one at the top of the tubes like all the time in this study (i.e. the definition always used in this study specified otherwise). The threshold Reynolds numbers calculated with equation 7.1 for all the measurements are shown in appendix A.

7.3 Boiling influence

In the region of figure 7.1 where the heat transfer does not vary much with the Reynolds number (Re> 500), it can be seen that the heat transfer coefficient for the even numbered tubes is higher than for the odd tubes. As a two-passes water circuit is used and hot water goes first in the even tubes, the heat flux is higher for the even tubes than for the odd ones. For this Turbo-BII HP tube, the lower heat transfer coefficient at higher heat flux is also the behavior observed in pool boiling conditions. Similar trends between the heat transfer coefficients in falling film evaporation and in pool boiling conditions have been observed for all the tested tubes as illustrated in figure 7.2.

For each tube, the measured falling film heat transfer coefficients are plotted as a function of the measured heat flux. For these graphs, the points for the three different tube pitches are all plotted together. The points with a Reynolds number at the top lower than the threshold Reynolds number defined above are on the other hand not included because they correspond to conditions with dry patches. The solid lines correspond to the boiling curves given in section 6.5.

From these graphs, it can be seen first that the falling film heat transfer coefficient in falling film conditions usually larger than the corresponding pool boiling one. The trend of the boiling curve is followed well by the

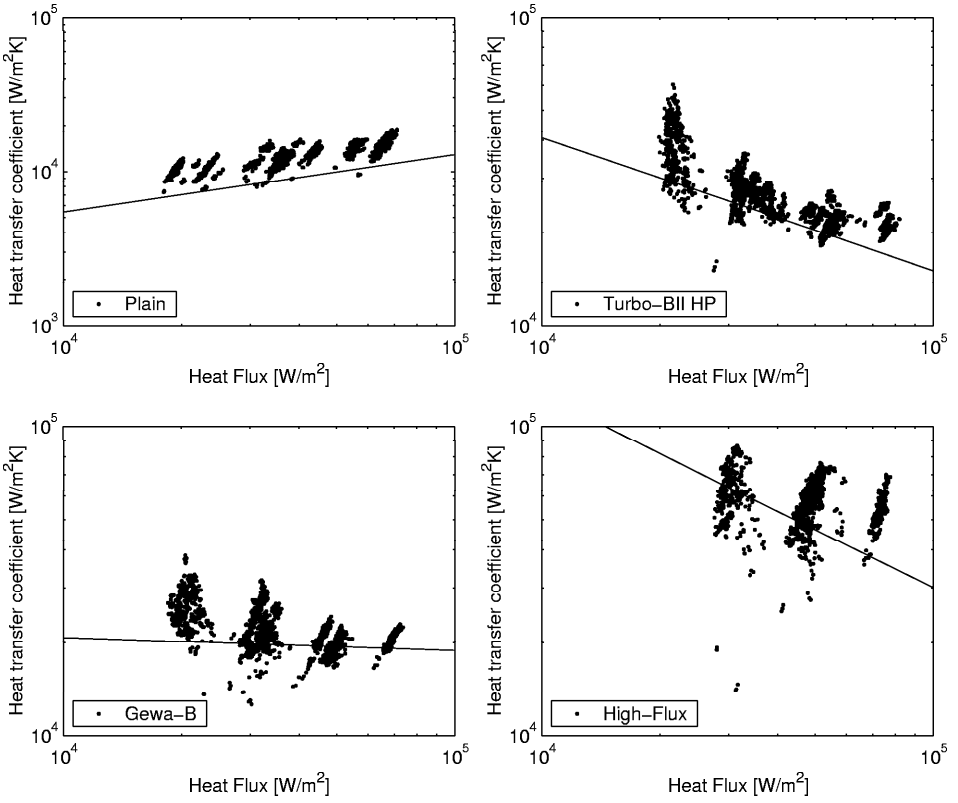

Figure 7.2: Falling film heat transfer coefficient as a function of the heat flux for each tube (general trend) with the nucleate boiling curve of each tube shown for reference.

measurements for the plain and the Turbo-BII HP tubes. For the Gewa-B, the data decreases faster with heat flux than the boiling curve while the opposite is observed with the High-Flux tube. These similarities between the heat transfer in pool boiling conditions and falling film conditions suggest that nucleate boiling is important in falling film evaporation in the tested heat flux range.

This boiling phenomenon was confirmed by the visual observations of the liquid film during falling film evaporation. Bubbles were present all the time in the film and make it much thicker compared to the conditions without heat transfer. The film was flowing like foam around the tube.

To verify that all the measurements have been made in conditions where there was nucleate boiling in the film, it is interesting to calculate the radius corresponding to the mechanical equilibrium at the liquid vapor interface of a spherical vapor nucleus (r_{nuc}) trapped inside the wall. This conditions is given by the equation of the necessary wall superheat to initiate boiling on

a plain surface:

$$T_o - T_{sat} = \frac{\Re T_{sat}^2}{h_{LV} M} \frac{2\sigma}{r_{nuc} P} \tag{7.2}$$

where T_o is the temperature of the external surface of the tube, $\Re$ is the universal gas constant ($8314.4 Nm/kmol \cdot K$) and M is the molecular weight equal to $102.3 kg/kmol$ for the refrigerant R-134a. Equation 7.2 can be rearranged to express r_{nuc} as a function of the other parameters known from measurements:

$$r_{nuc} = \frac{\Re T_{sat}^2 2\sigma}{(T_o - T_{sat}) h_{LV} M P} \tag{7.3}$$

Among the measurements of this study, the tubes with which the boiling is most likely to stop is the plain tube because the plain surface typically presents a smaller nucleation potential i.e. needs a higher superheat to initiate boiling than the enhanced ones. In terms of heat fluxes, if there is a the boiling limit, it should be for low heat flux. The minimum tested heat flux for the plain tube in falling film conditions was around $19 kW/m^2$ and the heat transfer coefficient was approximately $9500 W/m^2 K$, leading to a wall superheat of $2K$. Equation 7.3 gives for this case a nucleation radius of $1 \mu m$. A vapor bubble with a radius equal or larger than $1 \mu m$ will grow with these minimum heat flux conditions. If the contact angle β between the refrigerant and copper is 90°, that would mean that all the cavities in the surface with an open diameter of $1 \mu m$ remain activated at this heat flux. β is in fact lower than 90° because R-134a is a highly wetting fluid. An estimated value of 20° to 25° leads to a radius for the minimum activated sites of about 0.34 to 0.42 μm (r_{nuc} given by equation 7.3 is just multiplied by $\sin \beta$ due to the projection of the surface tension force). Cavities with diameters larger than the last calculated values are quite common for commercial copper plain surfaces (the mean surface roughness of the plain copper tubes was $Rp = 2 \mu m$).

The above analysis assumed a uniform system temperature while a thermal boundary layer exists in the liquid adjacent to the wall. Assuming that the thermal boundary layer is the the same as the natural convection case with a linear temperature profile, and that a nucleation site is activated when the temperature at the top of the corresponding vapor nucleus is larger than the one required for its equilibrium, the work of Han et Griffith [HAN65] leads to an equation linking the wall superheat and the heat flux at incipience of boiling. The interesting point is that no nucleation site radius is involved in this relation:

$$q_{incipience} = \frac{\lambda_L h_{LV}}{8 T_{sat} (1/\rho_V - 1/\rho_L) \sigma \times 1.5} (T_o - T_{sat})_{incipience} \tag{7.4}$$

This equation gives a heat flux of $16.7kW/m^2$ in the case of a superheat of $2K$. This value is smaller than the lowest tested one ($19kW/m^2$), indicating that all the measurements are expected to be in boiling conditions.

The approaches described above are normally used to determine the onset of boiling for increasing heat flux while they are used here as a verification that the boiling conditions are maintained. During the measurements, the heat flux is in fact decreased from a higher value (at the startup of the experiments) to the desired test conditions. Most of the nucleation sites are thus activated at the beginning and it is necessary to control if these sites remain activated.

From the three points evoked above: 1) the falling film heat transfer coefficients follow the same trend as the pool boiling ones, 2) bubbles were all the time visible in the film during experiments and 3) the test conditions remain all the time above the onset of nucleate boiling. Thus, it is clear that nucleate boiling is a major parameter in the process. For these reasons, a new falling film coefficient K_{ff} is defined by:

$$K_{ff} = \frac{\alpha_o}{\alpha_{pb}} \tag{7.5}$$

where α_o is the heat transfer coefficient in the falling film conditions and α_{pb} is the nucleate pool boiling heat transfer coefficient calculated at the current heat flux. In the present work, the pool boiling correlations of section 6.5 are used to determine values of α_{pb}. This falling film coefficient allows an easy comparison between the pool boiling performances and the falling film ones.

7.4 Film Reynolds number influence

Figure 7.1 can be transformed using equation 7.5 with the falling film factor to give figure 7.3 in which the spread in the points for Reynolds number above the threshold Reynolds number has decreased. This is due to the division by the pool boiling heat transfer coefficient which takes into account the heat flux influence on the nucleate boiling part of the falling film heat transfer process.

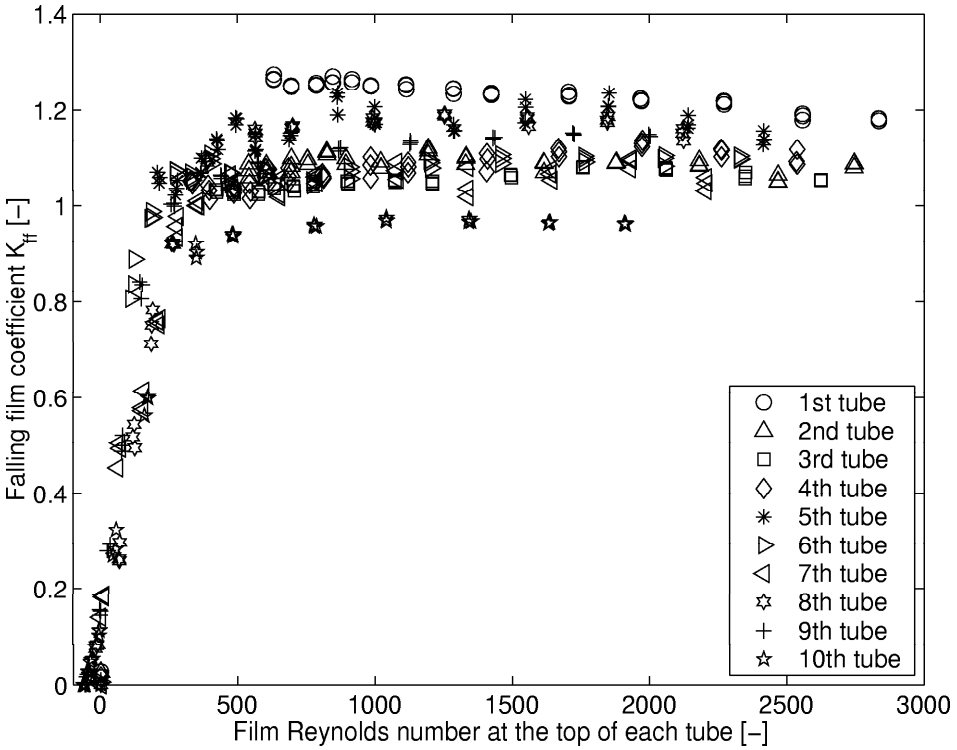

Figure 7.3: Falling film heat transfer coefficient as a function of film Reynolds number for Turbo-BII HP (tube pitch=22.3mm and nominal heat flux=$40kW/m^2$)

In these results, the heat flux range is quite important: approximately $37kW/m^2$ for the even tubes and $50kW/m^2$ for the odd tubes. To measure the film Reynolds number influence on the falling film coefficient K_{ff} at one heat flux, the results from figure 7.3 are split into two figures: one for the even and one for the odd tubes shown in figure 7.4.

On these graphs, the individual values of K_{ff} for a given tube are nearly constant when the Reynolds number changes from $Re_{ref,threshold}$ to 3000. An analysis of the heat flux shows that the heat flux is also nearly constant. The falling film heat transfer coefficient for one tube is thus nearly constant in this Reynolds number range. On the other hand, it can be seen on each figure that the the difference between the tubes is very small showing that the position in the bundle has no influence on the heat transfer. Two tubes perform the same if their thermal load and film Reynolds number at the top are similar independently of their position. For these reasons, the values of the falling film factor and heat flux from each measured point in this region have been averaged resulting in two constants: $K_{ff,plateau}$ for the mean falling film factor and $q_{o,plateau}$ for the mean heat flux. An iterative

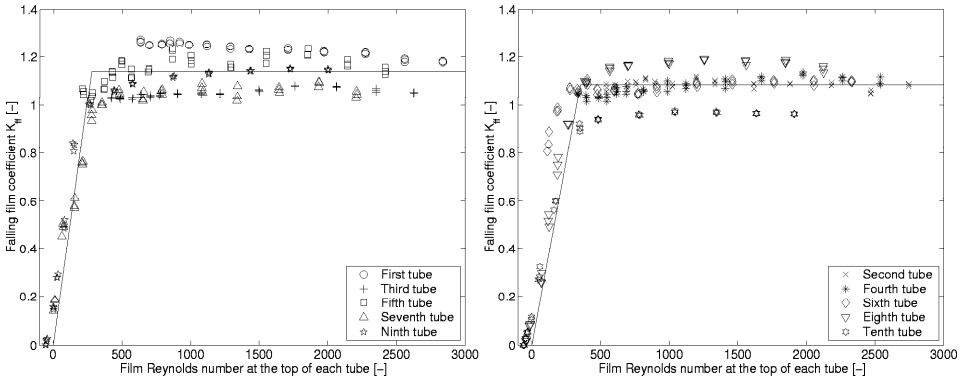

Figure 7.4: Falling film coefficient as a function of the film Reynolds number for even and odd tubes (Turbo-BII HP, tube pitch=22.3mm and nominal heat flux=$40kW/m^2$).

procedure has been used to find the $Re_{ref,threshold}$ because it is function of the heat flux $q_{o,plateau}$ (equations 6.15 and 7.1): a large value of the threshold Reynolds number is assumed, then all the values for the measurements with a larger Reynolds number are averaged, with this first mean heat flux, a new threshold is calculated and the procedure is repeated. After few iterations, all the values were stable. For the precedent measurements in figure 7.4, the results for the odd tubes are $Re_{ref,threshold} = 277$, $q_{o,plateau} = 37240kW/m^2$ and $K_{ff,plateau} = 1.1394$. Statistically, 90% of the measured falling film factors fall within $\pm 10\%$ of the mean value and 81% of the measured heat fluxes fall within $\pm 3\%$ of the mean value. The resulting constant and line toward zero are shown in figure 7.4 (right graph).

7.5 General trends in the data

The previous trends of the falling film coefficient have been observed for all the measurements. The procedure to calculate the mean falling film factor, the mean heat flux and the threshold Reynolds number has been repeated and all the results are shown in Annex A. To evaluate this heat transfer behavior for each type of tube, all the results are compiled in one graph. The falling film factor of each measured point is divided by the mean falling film factor of the corresponding measurement set and the film Reynolds number is divided by the threshold Reynolds number. Figures 7.5 and 7.6 show the results of this reduction.

On these graphs, it can be seen that the threshold value of the film Reynolds number is well correlated with the dryout Reynolds number except for the High Flux tube where the prediction seems to be a little too low. The visual detection of the dryout for this tube was more difficult due to

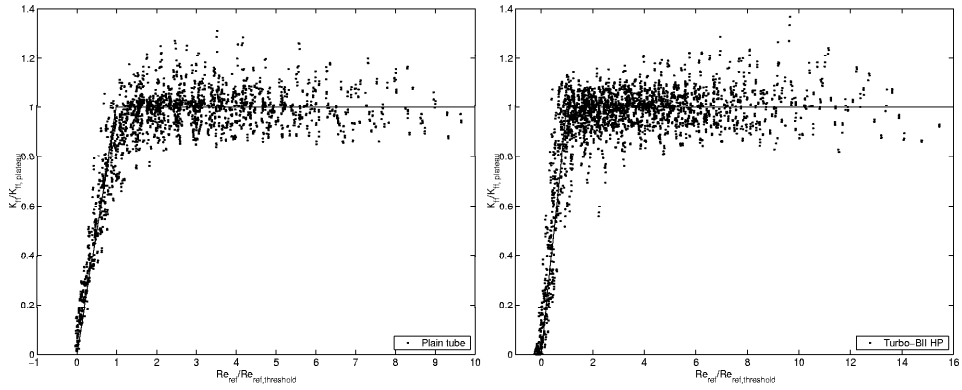

Figure 7.5: Distribution of the measured falling film coefficient for the plain and the Turbo-BII HP tubes.

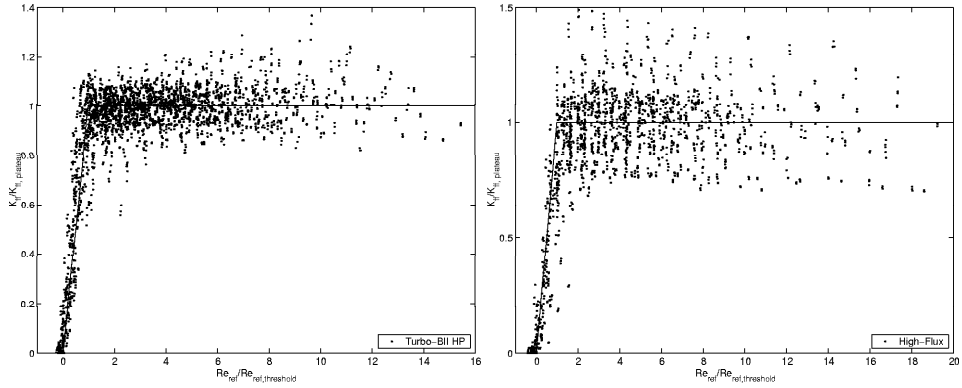

Figure 7.6: Distribution of the measured falling film coefficient for the Gewa-B and the High-Flux tubes.

the liquid flow inside the porous layer of the tube. Concerning the falling film coefficients for Reynolds number larger than the threshold Reynolds number, the distribution around the mean value is given in table 7.1. The distribution of the heat flux is also presented. The deviations in the falling film coefficients are comparable to the measurement errors. For the High-Flux tube, the deviation is larger than the others and is mainly due to larger experimental errors for measurements on this highly performing tube. The variation for a given tube when the film Reynolds number changes is very small.

The eventual dependance of the falling film coefficient versus the Reynolds number has been also examined. For each set of measurements, the slope was very small, sometimes increasing, sometimes decreasing. The result was

Percentage of points within	K_{ff} ±5%	K_{ff} ±10%	q_o ±2%	q_o ±4%
Plain Tube	52	80	68	95
Turbo-BII	53	87	78	98
Gewa-B	44	82	62	95
High-Flux	25	65	68	93

Table 7.1: Distribution of measured falling film coefficients (K_{ff}) around the mean falling film coefficient ($K_{ff,plateau}$).

a mean increase of 1.5% for the plain, the Gewa-B and the Turbo-BII HP tube over the complete Reynolds range, while for the High-Flux tube a decrease of 1.4 % was observed. These small slopes are not significant and hence this very small effect of Reynolds number has not been taken into account in development of the following model.

From the analysis above, it was deduced that the falling film coefficient K_{ff} for a given heat flux varied slightly versus the film Reynolds number in the region above the threshold Reynolds number. The following correlation is thus developed without an influence of Re_{ref} . The falling film coefficient and the threshold film Reynolds number are thus the only two parameters necessary to predict the heat transfer coefficient for a given heat flux.

7.6 Prediction of the falling film coefficient

From each set of measurements (one tube, one spacing, one nominal heat flux and all the film Reynolds numbers), one value of the falling film factor $K_{ff,plateau}$ has been calculated like described above. The result is a set of values for each tube. A correlation, in which the heat flux influence and the tube pitch influence are separated is proposed in equation 7.6:

$$K_{ff,plateau} = \left(1 + b_1 \frac{tp}{tp_o}\right)\left(b_2 + b_3\left(\frac{q_o}{q_{crit}}\right) + b_4\left(\frac{q_o}{q_{crit}}\right)^2\right) \tag{7.6}$$

In this equation, the tube pitch tp is nondimensionalized with the minimum tube pitch tested, $tp_o = 22.25mm$, the heat flux q_o is reduced with the critical heat flux q_{crit} from the Kutateladze [KUTA48] correlation:

$$q_{crit} = 0.131\rho_V^{0.5} h_{LV} \left(g\left(\rho_L - \rho_V\right)\sigma_L\right)^{0.25} \tag{7.7}$$

Since heat transfer shown to be so strongly dependent of nucleate boiling, it is logical to relate this effect to the heat flux relative to the critical value (which is the maximum). For R-134a at 278K ($5°C$) the critical heat flux is $361.3kW/m^2$, and the ratio q_o/q_{crit} varies from about 0.055 to 0.222 with the heat flux range of this study.

The empirical constants of this regression are presented in table 7.2 and the corresponding graphs are shown in figures 7.7 and 7.8.

	Plain tube	Turbo-BII HP	Gewa-B	High-Flux
b1	-0.335	-0.361	-0.303	-0.0104
b2	2.059	2.891	2.553	0.540
b3	2.370	-16.314	-14.170	5.723
b4	-7.793	59.906	47.706	-4.714

Table 7.2: Empirical constants for the falling film coefficient prediction.

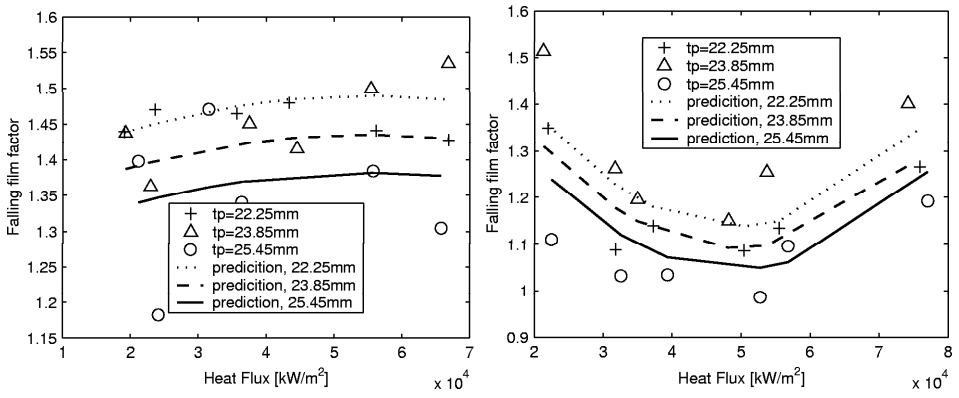

Figure 7.7: Measured falling film coefficients ($K_{ff,plateau}$) and corresponding correlations for the plain tube (top) and for the Turbo-BII (bottom)

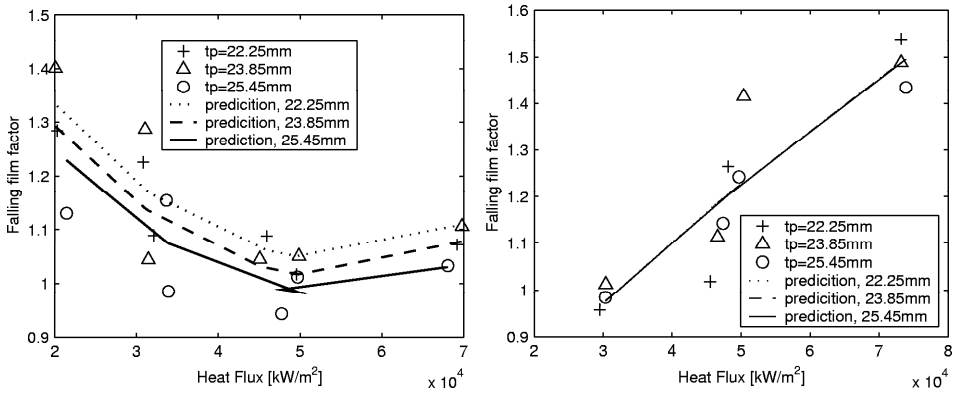

Figure 7.8: Measured falling film coefficients ($K_{ff,plateau}$) and corresponding correlations for the Gewa-B tube and the High-Flux tube.

7.6.1 Tube pitch influence

The constant b1 for the tube pitch influence is nearly the same for the plain tube, the Turbo-BII HP and the Gewa-B. This value is negative indicating that the value of the falling film coefficient decreases when the tube pitch increases. The variation is approximately -8% between the largest and the smallest tube pitch. The velocity of the liquid falling on the top of each tube increases with the tube pitch and has a negative impact on heat transfer. Danilova et al. [DANI76] found that in developed boiling range, the tube pitch had no effect on the heat transfer in their study. For the High-Flux tube, this influence is only 1% from the minimum tube pitch to the maximum one. For the other three tubes, the impinging liquid jet may have a local adverse effect on the nucleate boiling process.

7.6.2 Heat flux influence

The heat flux has a weak influence on the falling film coefficient of the plain tube which has a mean value of 1.4. The performance in falling film evaporation conditions is thus 40% higher than in pool boiling. Zeng et al. [ZENG97] found for their bundle with ammonia a falling film coefficient of about 1.5 to 2 for a plain tube while Danilova et al. [DANI76] found respectively 1.5, 1.4 and 1.33 for R-22 at a heat flux of $16kW$ and saturation temperatures of 273, 253 and 233K. For the Turbo-BII HP and the Gewa-B, the falling film coefficient presents similarities. The variation is from 1.3 at 20 kW/m^2 to respectively 1.15 and 1.05 at 50 kW/m^2. For those tubes with reentrant cavities, the liquid flow enters in the channels and refills them more rapidly for heat fluxes around $20kW/m^2$. When the heat flux increases to $50kW/m^2$, this circulation is limited by the bubbles leaving the holes and the behavior becomes similar than in pool boiling conditions. For even higher heat fluxes, the falling film coefficient increases slightly for the Gewa-B while it increases slightly faster for the Turbo-BII HP (higher maximum heat flux of $80kW/m^2$). The regression coefficients are similar for the two last tubes. For the High Flux tube, the falling film coefficient varies nearly linearly with the heat flux. This trend is the opposite of its boiling curve that decrease by a factor of 1.4 in this heat flux range. The resulting falling film heat transfer coefficient increases slightly with the heat flux.

7.6.3 Prediction method above onset of dryout threshold

The calculation of the heat transfer coefficient with the method presented above is described. For given conditions of heat flux and film Reynolds number, the first step is to determine whether the process is below or above the onset of dryout threshold. This can be done by using equation 7.1 and 6.15 with the current heat flux. If the calculated Reynolds number is larger than the current one, the conditions correspond to a point above the onset of

dryout threshold, the falling film factor can be calculated with equation 7.6 and then the falling film heat transfer coefficient is obtained by multiplying this falling film factor by the pool boiling heat transfer coefficient.

7.7 Accuracy of the predictions

To compare the measured heat transfer coefficients and the predicted ones, three statistical factors are calculated, based on the following definitions:

The relative error of each data point defined by:

$$\varepsilon_i = \frac{\alpha_{calc} - \alpha_{exp}}{\alpha_{exp}} \tag{7.8}$$

The mean error defined by:

$$\bar{\varepsilon} = \frac{1}{n} \sum \varepsilon_i \tag{7.9}$$

The standard deviation defined by:

$$\sigma = \sqrt{\frac{1}{n} \left(\sum \epsilon_i^2 \right) - (\bar{\varepsilon})^2} \tag{7.10}$$

The percentage of measured points that present a relative error in a given interval is also given. Comparisons between the predicted heat transfer coefficients and the measured ones are given in the table 7.3.

Tube	Plain	Turbo-BII HP	Gewa-B	High-Flux
standard deviation (%)	9.3	11.8	12.0	25.0
mean error (%)	1.3	1.9	1.7	5.0
% within $\pm$10%	77	70	65	50
% within $\pm$ 15%	89	83	81	65

Table 7.3: Accuracy of the prediction method (Re> $Re_{ref,threshold}$)

The predictions for the plain tube, the Turbo-BII HP tube and the Gewa-B tube present similar deviations while for the High-Flux tube, the deviation is larger. For this latter tube, the measurements presented larger deviations due to the very high heat transfer coefficients. Figure 7.9 shows a comparison of the predictions to the measurements. For the first three tubes, 81% of the data (or more) fall within $\pm$15% of the prediction.

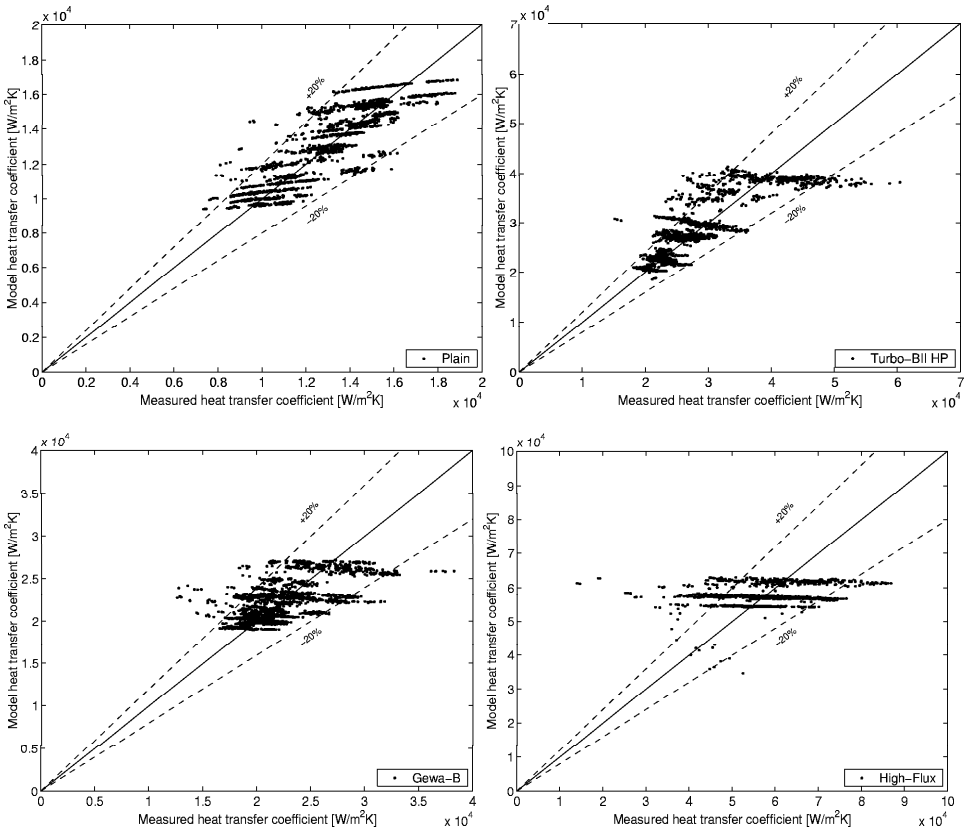

Figure 7.9: Calculated heat transfer coefficients versus measured heat transfer coefficients (Reynolds number larger than threshold Reynolds number)

In figure 7.10, a comparison is presented for each tube between the measured heat transfer coefficients and the ones calculated with the prediction method described above. The results are presented as a function of the heat flux. For more representative graphs, measured heat transfer coefficients over a range of Reynolds number are utilized while the prediction is made for an intermediate value. All the film Reynolds numbers correspond to conditions above the onset of dryout.

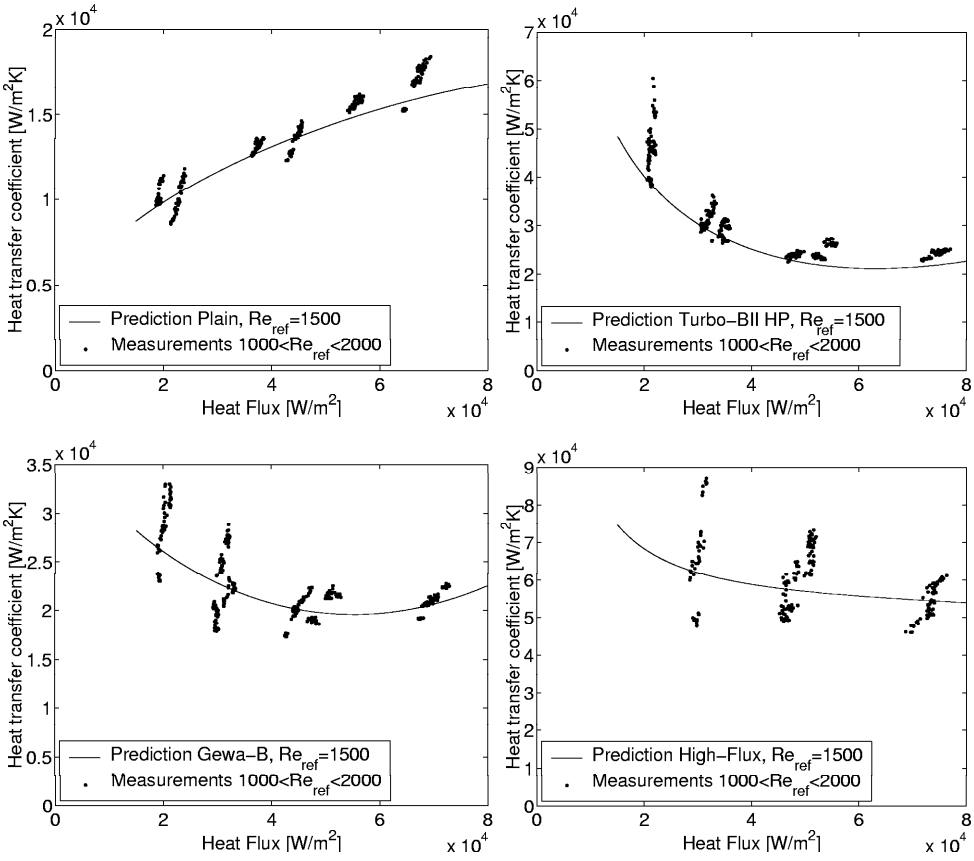

Figure 7.10: Calculated and measured heat transfer coefficients versus heat flux (tube pitch=23.9mm).

7.8 Prediction below the onset of dryout threshold Reynolds number

The correlation described above predicts the heat transfer coefficient when the conditions (heat flux and film Reynolds number) correspond to a situation above the threshold Reynolds number. Below this limit, the heat

transfer coefficient decreases rapidly with the flow rate due to the formation of dry patches formation. During the measurements of this study, the minimum tested liquid flow rates corresponded to those with dry patches on the bottom tube row of the array. As the liquid flow rate onto a tube with dry patches is determined by an energy balance on the tubes above, the uncertainty on the total heat flux is passed on as an uncertainty on the amount of liquid impinging the bottom tube. Even if the uncertainty in the heat flux is small, the impact at low liquid flow rates at the bottom becomes important. For example, the amount of liquid evaporated during high heat flux measurements corresponds to a Reynolds number of around 1000. An error of 3% in the heat flux leads to an absolute error of 30 on the Reynolds number at the bottom tube. If this last number on the bottom tube row is around 150, its relative error is thus 20%, which leads to an additional error on the falling film coefficient of 15 to 20 % depending on the type of tube. This region corresponds also to the limit of utilization of this type of evaporator (i.e. normally an evaporator should not be designed to function in this regime with partial dryout). A prediction method is presented to calculate the heat transfer coefficient in this region. As seen before, the falling film coefficient varies linearly with the Reynolds number in this region from zero to $K_{ff,plateau}$ when the Reynolds number changes from zero to $Re_{ref,threshold}$. On this line, the heat flux is also changing from zero to $q_{plateau}$. To predict points on this line, it is thus necessary to find the coordinates of the upper limit of this line to predict the falling film factor. The following equation shows the type of searched relationship:

$$\left(\frac{q_o}{q_{plateau}}\right) = f\left(\frac{Re_{ref}}{Re_{ref,threshold}}\right) \tag{7.11}$$

Where the heat flux and the Reynolds number have been divided by the corresponding ones at the beginning of the plateau. These $q_{plateau}$ and $Re_{ref,threshold}$ are linked by equation 7.1, which is specific for each type of tube. They thus contain information about the specific tube and the form of relation 7.11 can thus be identical for the four tubes. Figure 7.11 presents the variation of these parameters for all the measurements.

It can be seen that for the enhanced tubes, the film Reynolds number can be slightly negative (due to the energy balance effect on the upper tubes as noted previously). Despite that, the searched relation is forced to start at the origin. The resulting error is important for low Reynolds numbers and this prediction is applicable only when the Reynolds number ratio is larger than 0.6 (only range of interest in applications) . The points measured points below this limit have also a slightly higher measurement error because, during measurements, the parameters were optimized for the nominal heat flux, the points corresponding to an advanced dryout (low heat flux) were far from the nominal conditions.

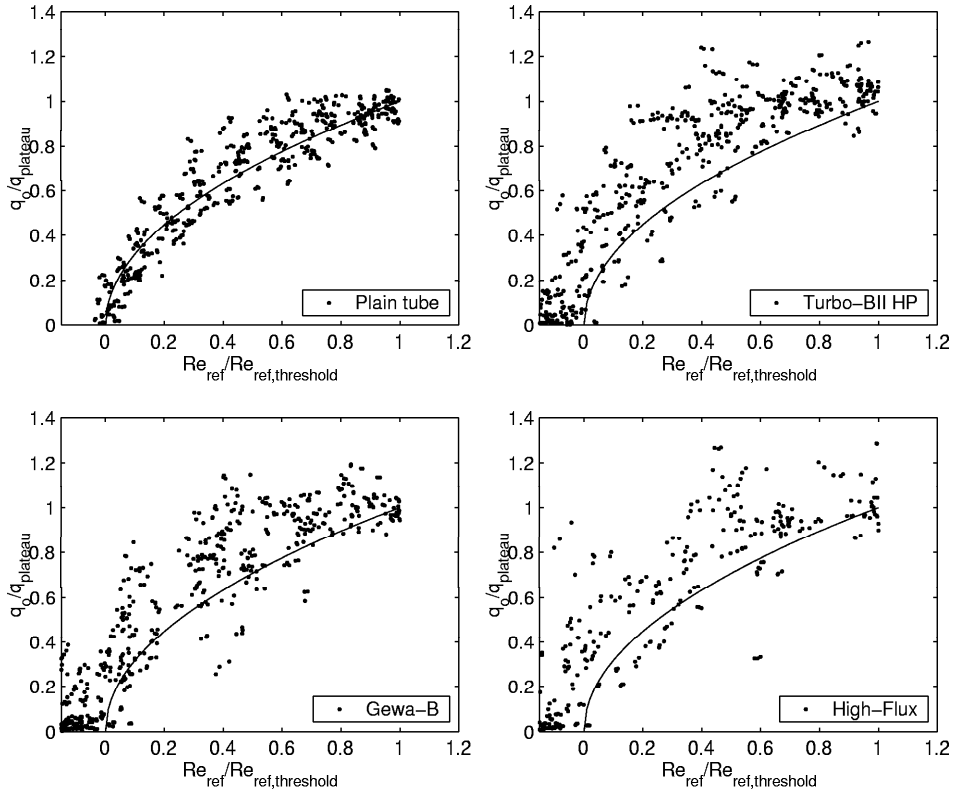

Figure 7.11: Heat flux ratio versus film Reynolds number ratio for all the measurements below the threshold limit.

A quadratic relation shown also in the figure was found satisfying to relate the behavior of these two parameters:

$$\left(\frac{Re_{ref}}{Re_{ref,threshold}}\right) = \left(\frac{q_o}{q_{plateau}}\right)^2 \tag{7.12}$$

In the above equation, $Re_{ref,threshold}$ and $q_{plateau}$ are linked with equation 7.1 and the dryout relation from section 6.6. The result is a linear variation between these two parameters:

$$Re_{ref,threshold} = 2\,(c \cdot q_{plateau} + d) \tag{7.13}$$

where c and d are the dryout parameters specific to each tube and measured in section 6.6. Combining equations 7.12 and 7.13 leads to the equation:

$$q_{plateau}^2 - 2c\left(\frac{q_o}{Re_{ref}} q_{plateau}\right) - 2d\frac{q_o^2}{Re_{ref}} = 0 \tag{7.14}$$

Knowing q_o and Re_{ref}, it is thus possible to find $q_{plateau}$. The parameter d which corresponds (by extrapolation) to the film breakdown Reynolds number without heat transfer is positive for the plain, the Turbo-BII tube and the Gewa-B tubes. The quadratic equation 7.14 gives in this case a positive and a negative value for $q_{plateau}$ and the solution is obviously the positive one. For the High-Flux tube, the parameter d is negative. Equation 7.14 gives either two positive values for $q_{plateau}$ or no solution. Based on the measurements, there were two solutions for $q_{plateau}$ and the the largest one was the correct one. As said in section 6.6, the film breakdown detection was difficult to observe on this tube and this negative value of d seems to be too low.

Using $q_{plateau}$ in equation 7.13 gives $Re_{ref,threshold}$. It is then possible to calculate $K_{ff,plateau}$ with the method described in section 7.6. The current falling film factor K_{ff} is then calculated assuming a linear function of the Reynolds number (this essentially means the dry fraction of the tube changes linearly with Re_{ref} as evident from the heat transfer data):

$$K_{ff} = \left(\frac{K_{ff,plateau}}{Re_{threshold}} \right) Re_{ref} \tag{7.15}$$

Multiplying this K_{ff} by the pool boiling heat transfer coefficient gives the predicted heat transfer coefficient for partially wetted tubes.

This method has been applied to the measurements below the threshold and for which $0.6 < K_{ff}/K_{ff,plateau} < 1$. The statistics of those predictions are presented in table 7.4.

Tube	Plain	Turbo-BII HP	Gewa-B	High-Flux
standard deviation (%)	24.9	24.2	41.3	74.2
mean error (%)	7.8	-11	4.9	22.2
% within ±40%	92	96.5	86.9	80

Table 7.4: Accuracy of the prediction method below the threshold

The errors are large but in this region, reliable measurements were difficult to obtain. Referring to figure 7.4, it is easily noted that this region has a prediction curve with a very high slope and hence small errors in Re_{ref} are magnified on the vertical axis. The mean error for the High-Flux tube is positive indicating that the dryout curve is under estimated. The standard deviations are large but few points were outside a range of ±40%.

7.9 Comparison with other data

Several correlations have been presented in chapter 2, all of which and they have each been developed specifically for a particular fluid: Zeng et al. [ZENG97] for ammonia and Parken [PARK90] for water. An extrapolation

of them to R-134a gives for the plain tubes heat transfer coefficients smaller by a factor of two than those measured in the current study. The plain tube utilized in the present work has also a relatively high roughness (Rp=2μm) and R-134a has significantly different physical properties than ammonia and water.

Moeykens [MOEY94] made falling film evaporation tests with R-134a and an experimental comparison is thus possible. Figure 2.1 shows his results for a single plain tube and also his pool boiling data which have been correlated to obtain the pool boiling curve of his tube. This relation is used in the correlation of the precedent section, equation 7.5, to calculate the heat transfer coefficient. Data were measured at very low liquid flow rate compared to the measurements of the current study. All his data thus fall below the onset of dryout threshold Reynolds number defined above (an intermediate tube pitch value of 23.85mm was used) and thus are predicted to be in the dry patch regime. The comparison is shown in the figure 7.12.

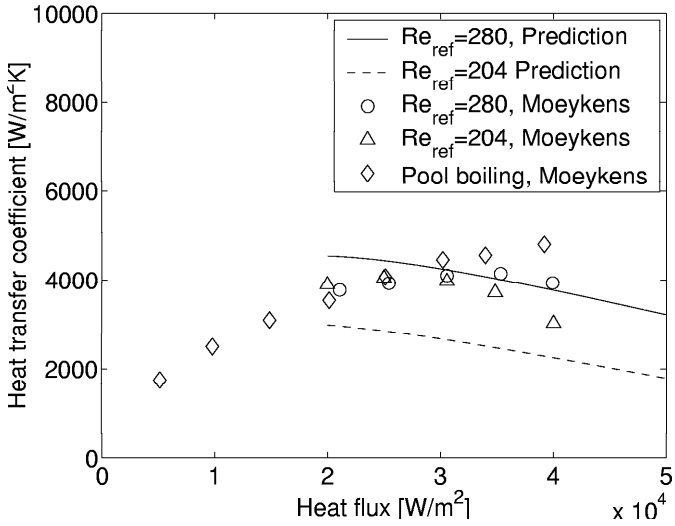

Figure 7.12: Comparison of the correlation and data from Moeykens (Plain tube 19.05mm, R-134a at Tsat=275K).

The prediction for the larger Reynolds number agrees quite well in magnitude but not in trend (solid curve) while the one for the lower Reynolds number (dashed curve) is 25% below their measurements. His measurements correspond to falling film spray evaporation (his tube was subjected to a spray nozzle) while the correlation developed here corresponds to conditions where the liquid is flowing from tube to tube. Thus, his result are not directly comparable to the present method but are the closest ones available.

7.10 Conclusions

New empirical approaches were developed based upon the test results and flow visualizations. First of all, a new criterion for predicting the heat transfer coefficient fall off (onset of dryout) during falling film evaporation was presented. Next, a new heat transfer prediction method was proposed that predicts the current measurements of falling film heat transfer coefficients to within $\pm 20\%$ for conditions without any dry patch formation. Below the onset of dryout threshold Reynolds number (at conditions with dry patches), the current measurements are predicted to within $\pm 40\%$. In a falling film evaporator, these last conditions should be avoided due to the poor heat transfer and the method is only proposed to allow simulations that go in this situation. This new approach for predicting falling film coefficients allows a direct comparison to be made with the nucleate pool boiling performance. The new method can be applied when conditions are similar to those here and can be extrapolated to other fluid/tube combinations as a first approximation when the boiling performance is known. The falling film coefficient behavior was found for example comparable for the Turbo-BII HP and the Gewa-B despite different nucleate boiling performances.

Chapter 8

Conclusions

A new test facility has been constructed especially for falling film evaporation measurements with R-134a as the working fluid. The overfeed liquid refrigerant is distributed on a vertical array of horizontal tubes. Similar to real evaporators, water was used as the thermal source. The heat flux was determined locally at mid tube with a temperature profile approach for each tube in the array while the heat transfer coefficient was determined with a modified Wilson plot technique. Four types of tubes were tested: a plain tube, two tubes with mechanically enhanced boiling surfaces and a porous coated tube. Tube arrays with three different tube pitches were tested. Measurements were performed at three different nominal heat fluxes over a wide range of liquid overfeed rates. For comparison, heat transfer coefficients in pool boiling conditions were also measured.

A very large experimental heat transfer database was obtained in this study that covers a wide range of test conditions with about 15000 data points. This data base is unique in that local heat transfer coefficients were measured as opposed to tube averaged values in previous studies and flow visualizations were made concurrently at all test conditions.

For a given heat flux and at high film Reynolds numbers, the heat transfer coefficient was found to be constant (not a function of the film Reynolds number). Below a film Reynolds number threshold, the heat transfer coefficients fell off drastically due to formation of dry patches. The threshold values of the film Reynolds number where the heat transfer coefficient starts to decrease were systematically determined (correlated to the film breakdown measurements). For falling film design purposes, it is better to remain above this limit.

It was found that the falling film heat transfer coefficients at film Reynolds numbers above the threshold can be correlated relative to the ones in pool boiling conditions and present a weak variation versus the film Reynolds number. The heat transfer coefficient during falling film evaporation was found to be from approximately 1 to 1.5 times larger than the heat trans-

fer coefficients during pool boiling. A prediction method was proposed to determine this enhancement factor, for the four types of tubes tested as a function of heat flux and tube pitch. This proposed correlation fits the measured data within $\pm 20\%$. This prediction method could eventually be extrapolated as a first approximation to other fluid/tube combinations.

In addition to the heat transfer measurements, visual observations of the liquid flow on the tubes were made. However, these observations were not included in the current heat transfer model as no first order effect of intertube flow mode on heat transfer was found (contrary to expectations).

In order to extend the application of this new heat transfer method, measurements and comparisons should be performed using different working fluids. Also, the test facility has the capability to operate with upward or downward vapor flow. This capability should be used in further studies to investigate the effect of vapor shear on falling film evaporation.

Bibliography

[ALHU97]
Alhusseini, A.A., Tuzla, K. and Chen, J.C. Heat transfer across evaporating falling films of single component liquids, *Convective Flow and Pool Boiling Conference*, , vol. , pp. 371–377, 1997.

[BAN78]
Bankoff, S.G. and Chung, J. Dryout of a thin heated liquid film, *International Heat and Mass Transfer Seminar*, , vol. 1 1978.

[BART00]
Barthau, G. and Hahne, E. Nucleation site density and heat transfer in nucleate pool boiling of refrigerant R-134a in a wide pressure range, *3rd European Thermal Sciences Conference*, , vol. 2, pp. 731–736, Sept. 2000.

[BUTTW90] Butterworth, D. *Film Condensation of Pure Vapor*, chapter 2.6.2. Hemisphere, New York, (1990).

[CHEN94]
Chen, J.C., Tuzla, K. and Wang, Q. Falling film evaporation of refrigerants, *10th International Heat Transfer Conference, Brighton*, , vol. 6, pp. 169–173, 1994.

[CHIO97]
Chiou, C.B. and Lu, D.C. Pool boiling of R-22, R-124, R-134a on a plain tube, *International Journal of Heat and Mass Transfer*, vol. 40, no. 7, pp. 1657–1666, 197.

[CHUN71]
Chun, K.R. and Seban, R.A. Heat transfer to evaporating liquid films, *Journal of Heat Transfer*, vol. 93, no. 4, pp. 391–396, 1971.

[CHYU82]
Chyu, M.C., Bergles, A.E. and Mayinger, F. Enhancement of horizontal tube spray evaporators, *Seventh International Heat Transfer Conference*, , vol. 6, pp. 275–280, 1982.

[CHYU85a]
Chyu, M.C. and Bergles, A.E. Falling film evaporation on a horizontal tube, *Multiphase Flow and Heat Transfer, ASME HTD*, , vol. 47, pp. 39–48, 1985.

[CHYU85b]
Chyu, M.C. and Bergles, A.E. Enhancement of horizontal tube spray film evaporators by structured surfaces, *Advanced in Enhanced Heat Transfer*, , vol. 43, pp. 39–47, 1985.

[CHYU87]
Chyu, M.C. and Bergles, A.E. An analytical and experimental study of falling-film evaporation on a horizontal tube, *Journal of Heat Transfer*, , vol. 109, pp. 983–990, 1987.

[CHYU89]
Chyu, M.C. and Bergles, A.E. Horizontal-tube falling-film evaporation with structured surfaces, *Journal of Heat Transfer*, , vol. 111, pp. 518–524, 1989.

[COOPER84] Cooper, M.G. *Advances in Heat Transfer*, volume 16, chapter Heat flow rates in saturated nucleate pool boiling - A wide range examination using reduced properties, pp. 157–239. Hartnett and Irvine, Princeton, Academic Press edition.

[DANGER01]
Danger, E., Chandra, U., Gorenflo, D. and Beutler, A. Basic modifications of the heated surface for enhancement of pool boiling heat transfer, *Thermophysical Properties and Transfer Process of New Refrigerants*, , vol. Oct. 2001.

[DANI76]
Danilova, G.N., Burkin, V.G. and V.A., Dyundin Heat transfer in spray-type refrigerator evaporators, *Heat Transfer Soviet Research*, vol. 8, no. 6, pp. 105–113, 1976.

[DONI91]
Doniec, A. Laminar flow of a liquid rivulet down a vertical surface, *Canadian Journal of Chemical Engineering*, , vol. 69, pp. 198–202, 1991.

[ELGE01]
El-Genk, A.S. and Saber, H.H. Minimun thickness of a flowing down liquid film on a vertical surface, *International Journal of Heat and Mass Transfer*, , vol. 44, pp. 2809–2825, 2001.

[FUJI78]
Fujita, T. and Ueda, T. Heat transfer to falling liquid films and film breakdown–ii saturated liquid films with nucleate boiling, *International Journal of Heat and Mass Transfer*, , vol. 21, pp. 109–118, 1978.

[FUJI94]
Fujita, Y. and Tsutsui, M. Experimental and analytical study of evaporation heat transfer in falling films on horizontal tubes, *10th International Heat Transfer Conference, Brighton*, , vol. 6, pp. 175–180, 1994.

[FUJI95]
Fujita, Y. and Tsutsui, M. Evaporation heat transfer of falling films on horizontal tube -part 1- analytical study, *Heat Transfer Japanese Research*, vol. 24, no. 1, pp. 1–16, 1995.

[FUJI98]
Fujita, Y. and Tsutsui, M. Experimental investigation of falling film evaporation on horizontal tubes, *Heat Transfer Japanese Research*, vol. 27, no. 8, pp. 609–618, 1998.

[GANI80]
Ganic, E.N. and Roppo, M.N. An experimental study of falling liquid film breakdown on a horizontal cylinder during heat transfer, *Journal of Heat Transfer*, , vol. 102 1980.

[GANI86]
Ganic, E.N. and Getachew, D. Effects of surface condition and working fluid on liquid film breakdown during heat transfer, *8th International Heat Transfer Conference*, , vol. 4, pp. 1931–1936, 1986.

[GNIE76]
Gnielinski, V. New equations for heat and mass transfer in turbulent pipe and channel flow, *International Chemical Engineering*, vol. 16, no. 2, pp. 359–368, 1976.

[GOREN00]
Gorenflo, D., Fust, W., Luke, A., Danger, E. and Chandra, U. Pool boiling heat transfer from tubes with basic surface modifications for enhancement, *3rd European Thermal Sciences Conference*, , vol. , pp. 743–747, Sept. 2000.

[GOREN93] Gorenflo, D. *VDI-Heat Atlas*, chapter Pool Boiling. VDI-Verlag, Düsseldorf, english version edition, (1993).

[GROS94]
Gross, U. Falling film evaporation inside a closed thermosyphon, *10th International Heat Transfer Conference, Brighton*, , vol. 7, pp. 443–448, 1994.

[GSTO04] Gstöehl, D. Heat transfer an flow visualization of falling film condensation on tube arrays with plain and enhanced surfaces, *Swiss Federal Institute of Technology*, Lausanne, 2004.

[HAN65]
Han, C.Y. and Griffith, P. The mechanism of heat transfer in nucleate pool boiling part i, *International Journal of Heat and Mass Transfer*, , vol. 8, pp. 887–904, 1965.

[HART64]
Hartely, D.E. and Murgatroyd, W. Criteria for the break-up of thin liquid layers flowing isothermally over solid surface, *International Journal of Heat and Mass Transfer*, , vol. 7, pp. 1003–1015, 1964.

[HOBL64]
Hobler, T Minimum surface wetting, *Chemia Stosow*, , vol. 2B, pp. 145–159, 1964.

[HOND87]
Honda, H., Nozu, S. and Takeda, Y. Flow characteristics of condensation on a vertical column of horizontal tubes, *Proc. 1987 ASME-JSME*

Thermal Engineering Joint Conference, Honolulu, , vol. 1, pp. 517–524, 1987.

[HSIE94]
HSIEH, S.S. AND HSU, P.T. Nucleate boiling characteristics of R-114, distilled water H2O and R-134a on plain and rib-roughned tube geometries, *International Journal of Heat and Mass Transfer*, vol. 37, no. 10, pp. 1423–1432, 1994.

[HSU65]
HSU, Y.Y., SIMON, F.F. AND LAD, J.F. Destruction of a thin liquid film flowing over a heating surface, *Chemical Engineering Progress Symposium Series*, vol. 61, no. 57, pp. 139–152, 1965.

[HU96a]
HU, X. AND JACOBI, A.M. The intertube falling film part 1-flow characteristics, mode transitions and hysteresis, *ASME J. Heat Transfer*, , vol. 118, pp. pp. 616–625, 1996.

[HU98]
HU, X. AND JACOBI, A.M. Departure-site spacing for liquid droplets and jets falling between horizontal circular tubes, *Exp. Therm. Fluid Sci.*, , vol. 16, pp. 322–331, 1998.

[KRAM97]
KRAMER, W., AURACHER, H. AND MARVILLET, C. Cross flow and pool boiling of ethanol-water mixtures on the outside of horizontal enhanced tubes, *Convective Flow and Pool Boiling, 3rd Conference of the International Engineering Foundation*, , vol. 1, pp. 419–426, 1997.

[KUTA48]
KUTATELADZE, S.S. On the transition to film boiling under natural convection, *Kotloturbostroenie*, vol. 3, no. 10 1948.

[LORE78]
LORENZ, J.J. AND YUNG, D. Combined boiling and evaporation of liquid films on horizontal tubes, *fifth OTEC Conference*, , vol. 3, pp. 46–70, 1978.

[LORE79]
Lorenz, J.J. and Yung, D. A note on boiling and evaporation of liquid films on horizontal tubes, *Journal of Heat Transfer*, , vol. 101, pp. 178–180, 1979.

[MCNE02]
McNeil, D.A., Burnside, B.M., Miller, K.M. and Tarrad, A.H A comparison between high flux and plain tubes, boiling pentane in a horizontal kettle reboiler, *Applied Thermal Engineering*, , vol. 22, pp. 803–814, 2002.

[MEMO95a]
Memory S.B., D.C. and Marto, P.J. Nucleate pool boiling of R-114 and R-114-oil mixtures from smooth and enhanced surfaces-1. single tubes, *International Journal of Heat and Mass Transfer*, vol. 8, no. 8, pp. 1347–1361, 1995.

[MITR86]
Mitrovic, J. Influence of tube spacing and flow rate on heat transfer from a horizontal tube to a falling liquid film, *Proc. 8th International Heat Transfer Conf., San Francisco*, , vol. 4, pp. 1949–1956, 1986.

[MITR95]
Mitrovic, J. and Ricoeur, A. Fluid dynamics and condensation heating of capillary liquid jets, *Int. J. Heat Mass Transf.*, , vol. 38, pp. 1483–1494, 1995.

[MOEY94]
Moeykens, S.A. and Pate, M.B. Spray evaporation heat transfer of R-134a on plain tubes, *ASHRAE Transactions*, vol. 100, no. 2, pp. 173–184, 1994.

[MOEY95a]
Moyekens, S.A., Huebsch, W.W. and Pate, M.B. Heat transfer of R-134a in single-tube spray evaporation including lubricant effects and enhanced surface results, *ASHRAE Transactions*, vol. 101, no. 1, pp. 111–123, 1995.

[MOEY95b]
Moeykens, S.A., B.J., Newton and Pate, M.B. Effects of surface

enhancement, film-feed supply rate, and bundle geometry on spray evaporation heat transfer performance, *ASHRAE Transactions*, vol. 101, no. 2, pp. 408, 419 1995.

[MOEY95c]
MOEYKENS, S.A. AND PATE, M.B. The effects of nozzle height and orifice size on spray evaporation heat transfer performance for a low-finned, triangular pitch tube bundle with R-134a, *ASHRAE Transactions*, vol. 101, no. 2, pp. 420–433, 1995.

[MOEY96a]
MOYEKENS, S.A. AND PATE, M.B. Effect of lubricant on spray evaporation heat transfer performance of R-134a and R-22 in tube bundles, *ASHRAE Transactions*, vol. 102, no. 1, pp. 410–426, 1996.

[MOEY96b]
MOYEKENS, S.A., KELLY, J.E. AND PATE, M.B. Spray evaporation heat transfer performance of R-123 in tube bundles, *ASHRAE Transactions*, vol. 102, no. 2, pp. 259–272, 1996.

[PARK90]
PARKEN, W.H., FLETCHER, L.S., SERNAS, V. AND HAN, J.C. Heat transfer evaporation through falling film evaporation, *Journal of Heat Transfer*, , vol. 112, pp. 744–750, 1990.

[PETUKHOV96] INCROPERA, F.P. AND DEWITT, D.P. *Fundamentals of Heat and Mass Transfer*, chapter 8, pp. 424. John Willey & Sons, 4th edition, (1996).

[PRZU91]
PRZULJ, V. AND GANIC, E.N. Breakdown of subcooled falling liquid film on horizontal tube, *2nd World Conference in Experimental Heat Transfer, Fluids Mechanics and Thermodynamics*, , vol. , pp. 792–799, 1991.

[ROHS62]
ROHSENOW, W.M A method of correlating heat transfer data for surface boiling of liquids, *Journal Heat Transfer*, , vol. 74, pp. 969–975, 1962.

[ROQU01]
J.-F., Roques and J.R., Thome Flow patterns and phenomena for falling films on plain and enhanced tube arrays, *Proc. Third International Conference on Compact Heat Exchangers and Enhancement Technology for the Process Industries, Davos, Switzerland, 1-6 July*, , vol. , pp. 391–398, 2001.

[ROQU02A]
J.-F., Roques, V., Dupont and J.R., Thome Falling film transitions on plain and enhanced tubes, *J. Heat Transfer*, , vol. 124, pp. 491–499, 2002.

[ROQU02B]
J.-F., Roques and J.R., Thome Falling film transitions between droplets, column and sheet flow modes on a vertical array of horizontal 19 fpi and 40 fpi low finned tubes, *Proc. 1st International Conference on Heat Transfer, Fluid Mechanics and Thermodynamics, HEFAT2002, 8-10 April, Kruger Park, South Africa*, vol. 1, no. 1, pp. 523–528, 2002.

[ROQU03]
J.-F., Roques and J.R., Thome Falling film transitions between droplet, column and sheet modes on a vertical array of horizontal 19 fpi and 40 fpi low finned tubes, *Heat Transfer Engineering*, , vol. 24, pp. 40–45, 2003.

[SMIR00]
Smirnov, H.F. Heat and mass transfer when boiling on coated surfaces in porous structures, *3rd European Thermal Sciences Conference*, , vol. 2, pp. 803–808, 2000.

[STEP80]
Stephan, D. and Abdelsalam, M. Heat transfer correlations for natural convection boiling, *International Journal of Heat and Mass Transfer*, , vol. 23, pp. 73–87, 1980.

[TAGH80]
Taghavi, K. and Dhir, V.K. Taylor instability in boiling, melting, condensation or evaporation, *Int. J. Heat Mass Transfer*, , vol. 23, pp. 1433–1445, 1980.

[TANG91]
Tang, Z. and Lu, B.Y.C Droplet spacing of falling film flow on horizontal tube bundles, *Proc. 18th International Congress of Refrigeration, Montreal*, , vol. 2, pp. 474–478, 1991.

[TATA00]
Tatara, R.A. and Payvar, P. Pool boiling of pure R-134a from a single Turbo-BII HP tube, *International Journal of Heat and Mass Transfer*, , vol. 43, pp. 2233–2236, 2000.

[THOM03] Thome, J.R. and Robinson, D. Flooded evaporation heat transfer performance investigation for tube bundles including the effect of oil using R-410a and R-507a. Research project RP-1089, Final Report, ASHRAE, (2003).

[THOM99]
Thome, J.R. Falling film evaporation: state of the art review of recent work, *Enhanced Heat Transfer*, , vol. 6, pp. 263–277, 1999.

[WEBB92]
Webb, R.L. and Pais, C. Nucleate pool boiling data for five refrigerants on plain, integral-fin and enhanced tube geometries, *International Journal of Heat and Mass Transfer*, vol. 35, no. 8, pp. 1893–1904, 1992.

[ZENG94]
Zeng, X., Chyu, M.C. and Ayub, Z.H. Characteristic study of sprayed fluid flow in a tube bundle, *ASHRAE Transactions*, vol. 100, no. 1, pp. 63–72, 1994.

[ZENG95]
Zeng, X., Chyu, M.C. and Ayub, Z.H. Evaporation heat transfer performance of nozzle-sprayed ammonia on a horizontal tube, *ASHRAE Transactions*, vol. 101, no. 1, pp. 136–149, 1995.

[ZENG97]
Zeng, X., Chyu, M.C. and Ayub, Z.H. Performance of nozzle-sprayed ammonia evaporator with a square-pitch tube bundle, *ASHRAE Transactions*, vol. 103, no. 2, pp. 68–81, 1997.

[ZURC00] Zürcher, O. Contribution to the heat transfer analysis of natural and substitute refrigerants evaporated in a smooth horizontal tube, *Swiss Federal Institute of Technology*, Lausanne, 2000.

Appendix A

Falling film evaporation results

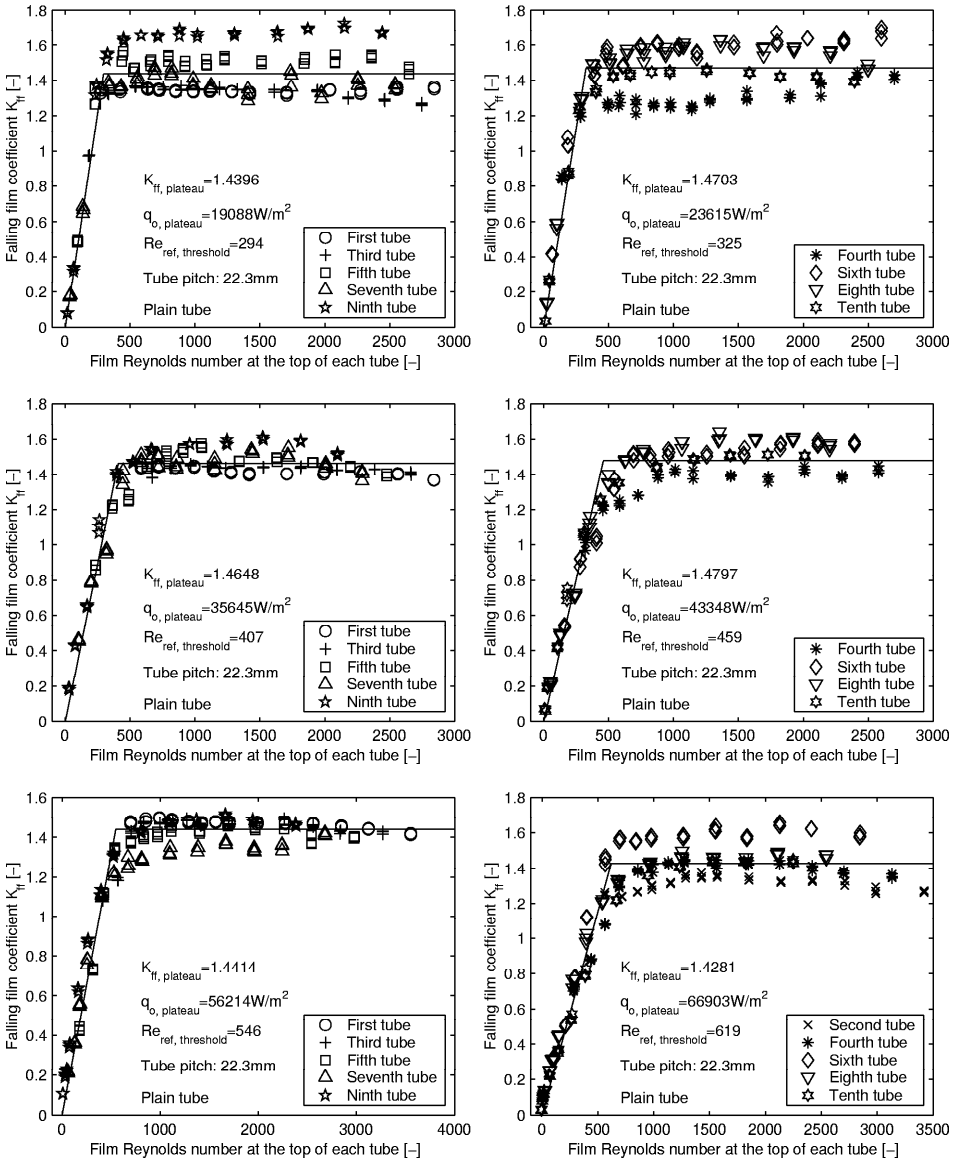

Figure A.1: Falling film heat transfer coefficient ratio K_{ff}, (measured/boiling) for plain tube with a tube pitch of 22.3mm, nominal heat flux of 20, 40 and 60kW/m^2 in the top, the middle and the bottom plots, respectively.

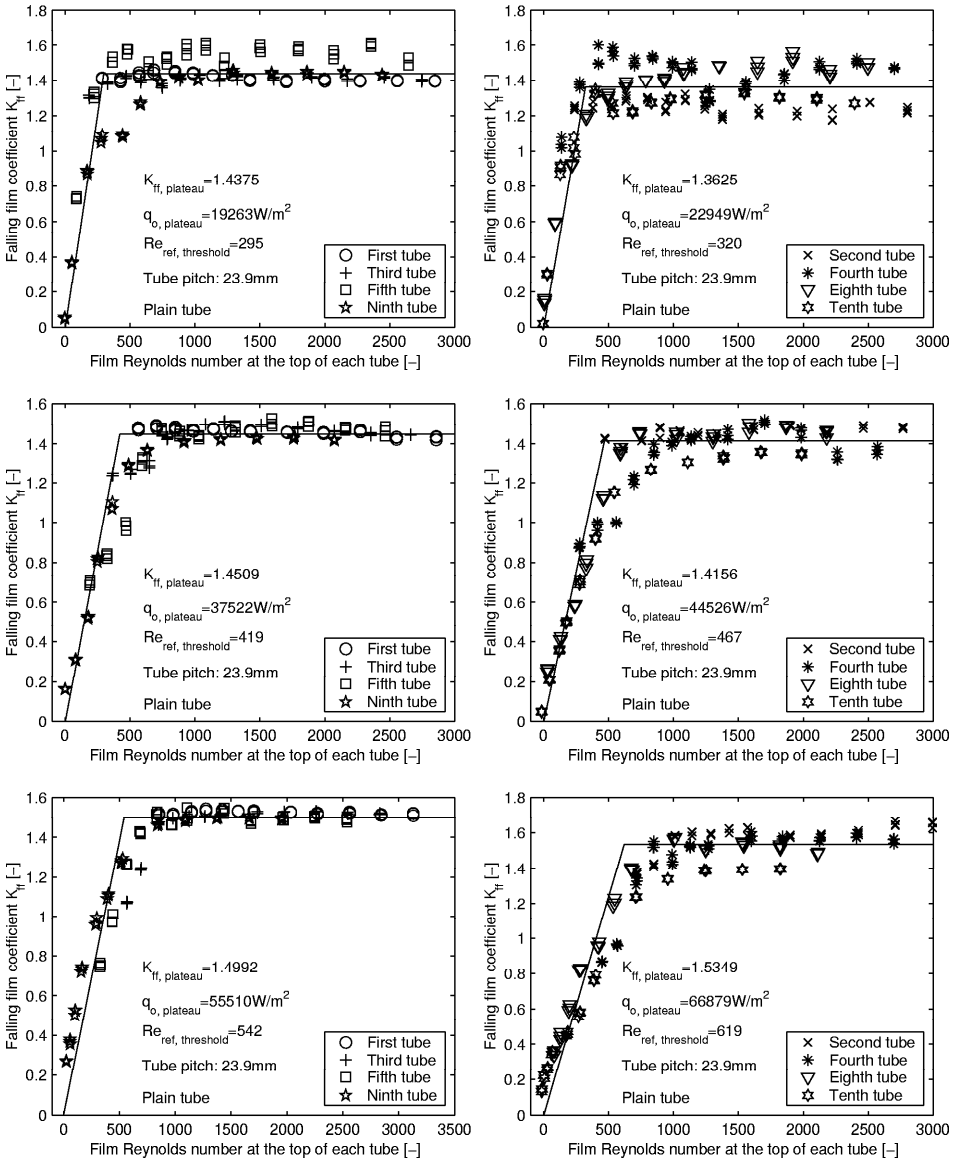

Figure A.2: Falling film heat transfer coefficient ratio K_{ff}, (measured/boiling) for plain tube with a tube pitch of $23.9mm$, nominal heat flux of 20, 40 and $60kW/m^2$ in the top, the middle and the bottom plots, respectively.

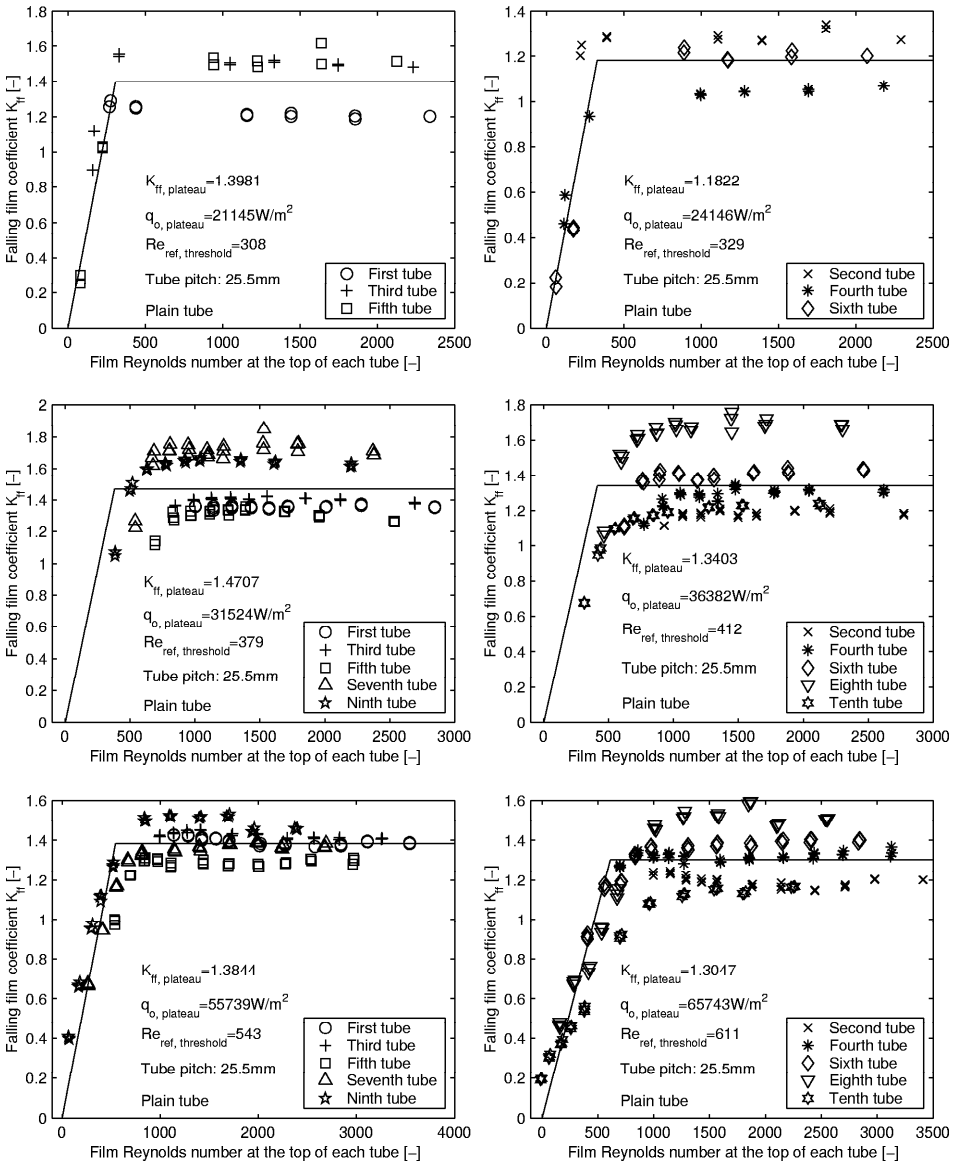

Figure A.3: Falling film heat transfer coefficient ratio K_{ff}, (measured/boiling) for plain tube with a tube pitch of $25.5mm$, nominal heat flux of 20, 35 and $60kW/m^2$ in the top, the middle and the bottom plots, respectively.

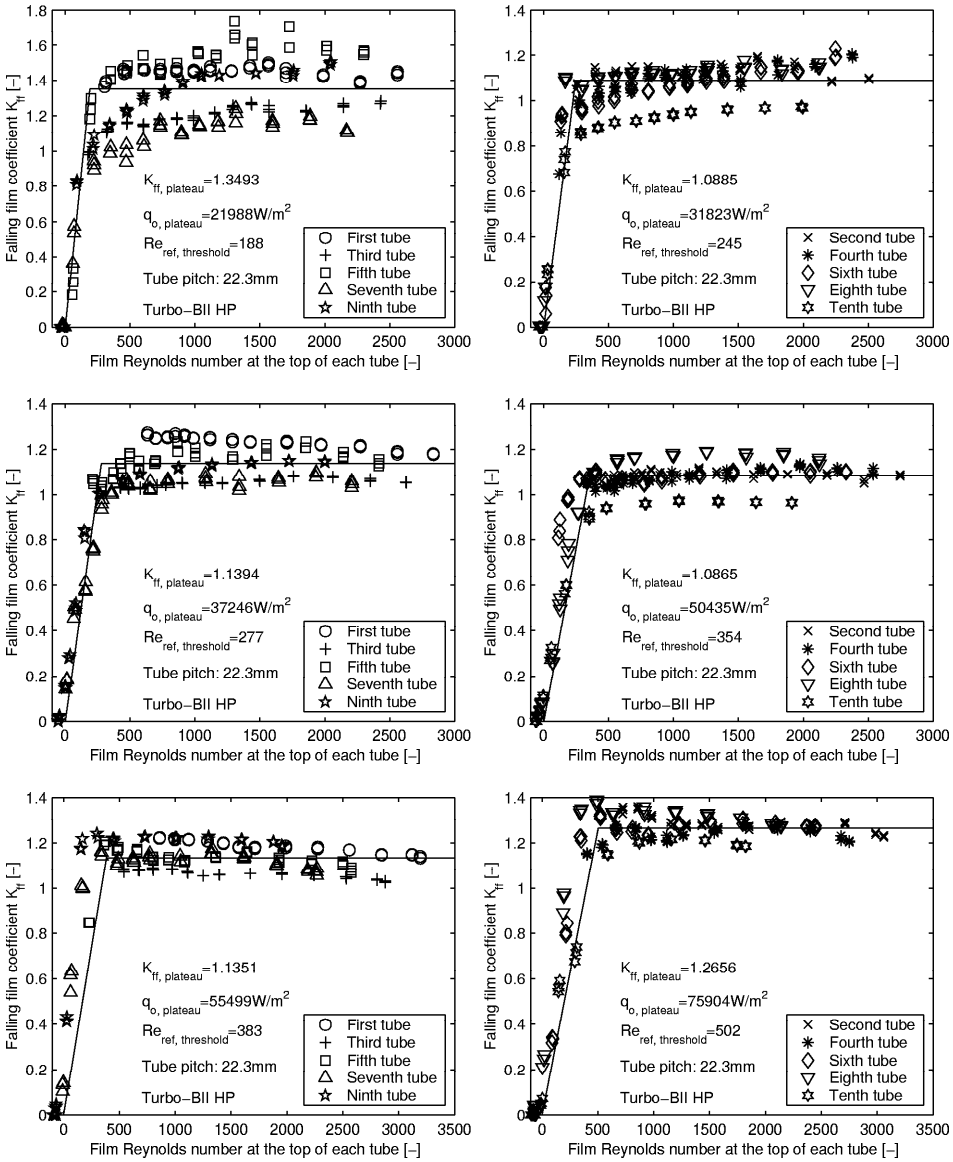

Figure A.4: Falling film heat transfer coefficient ratio K_{ff}, (measured/boiling) for Turbo-BII HP tube with a tube pitch of 22.3mm, nominal heat flux of 25, 45 and 65kW/m^2 in the top, the middle and the bottom plots, respectively.

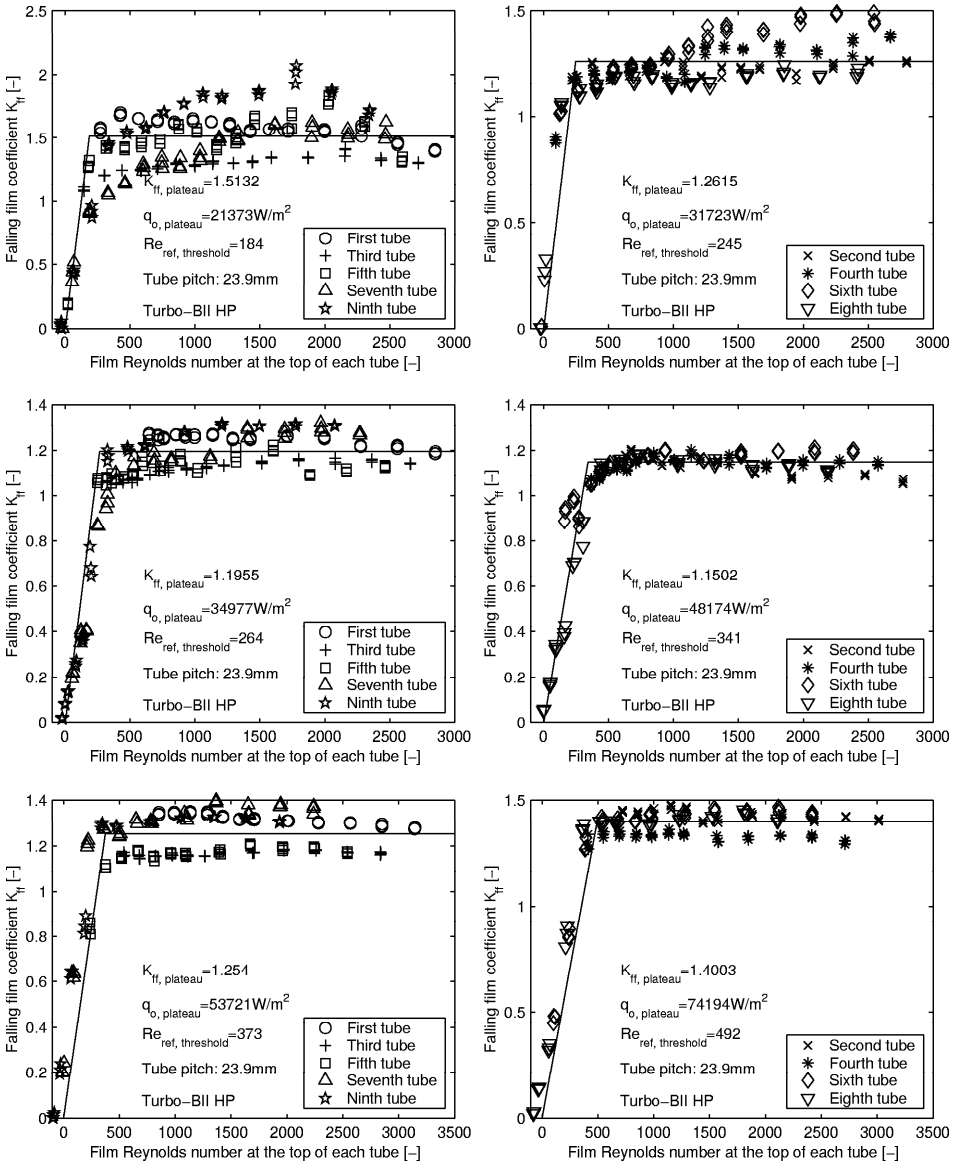

Figure A.5: Falling film heat transfer coefficient ratio K_{ff}, (measured/boiling) for Turbo-BII HP tube with a tube pitch of $23.9mm$, nominal heat flux of 25, 45 and $65kW/m^2$ in the top, the middle and the bottom plots, respectively.

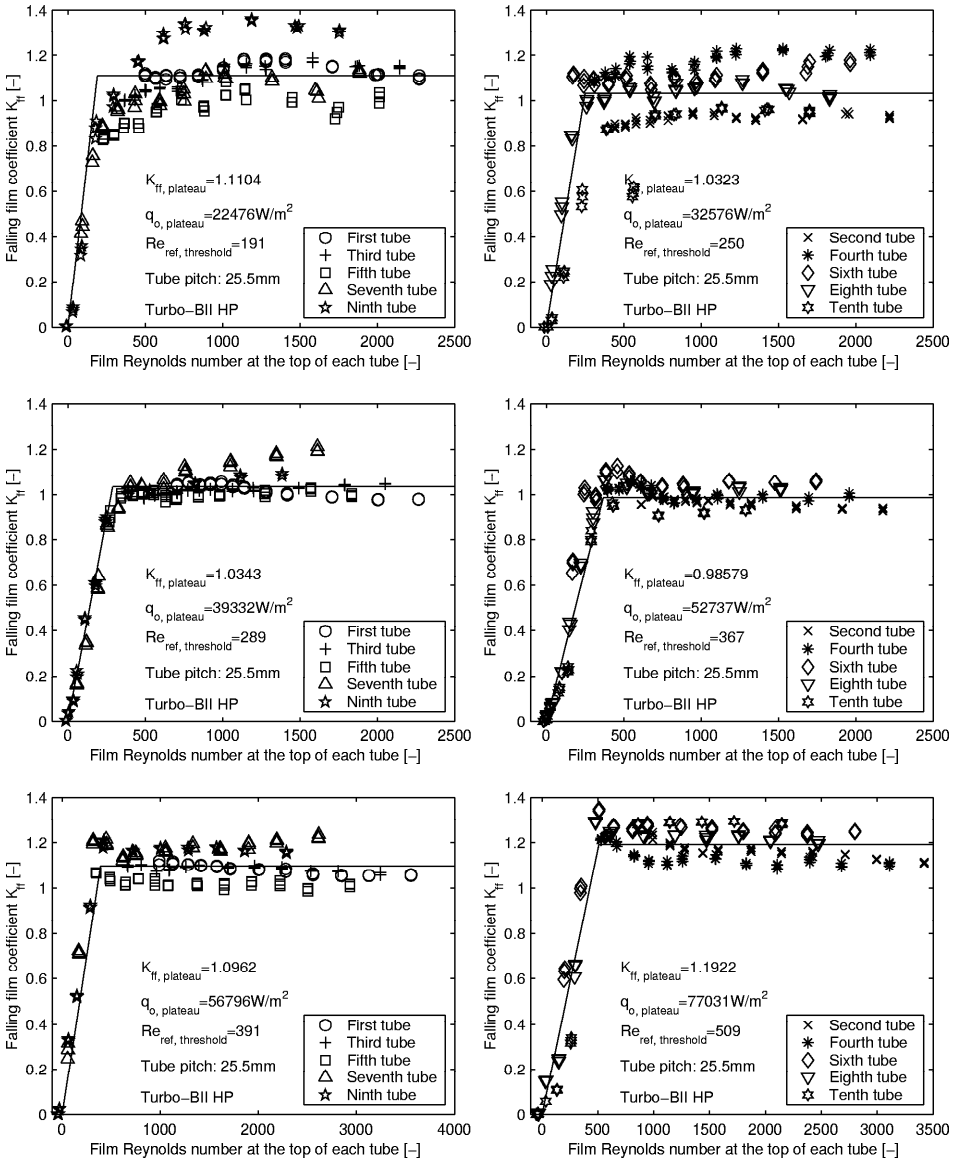

Figure A.6: Falling film heat transfer coefficient ratio K_{ff}, (measured/boiling) for Turbo-BII HP tube with a tube pitch of 25.5mm, nominal heat flux of 20, 45 and 60kW/m^2 in the top, the middle and the bottom plots, respectively.

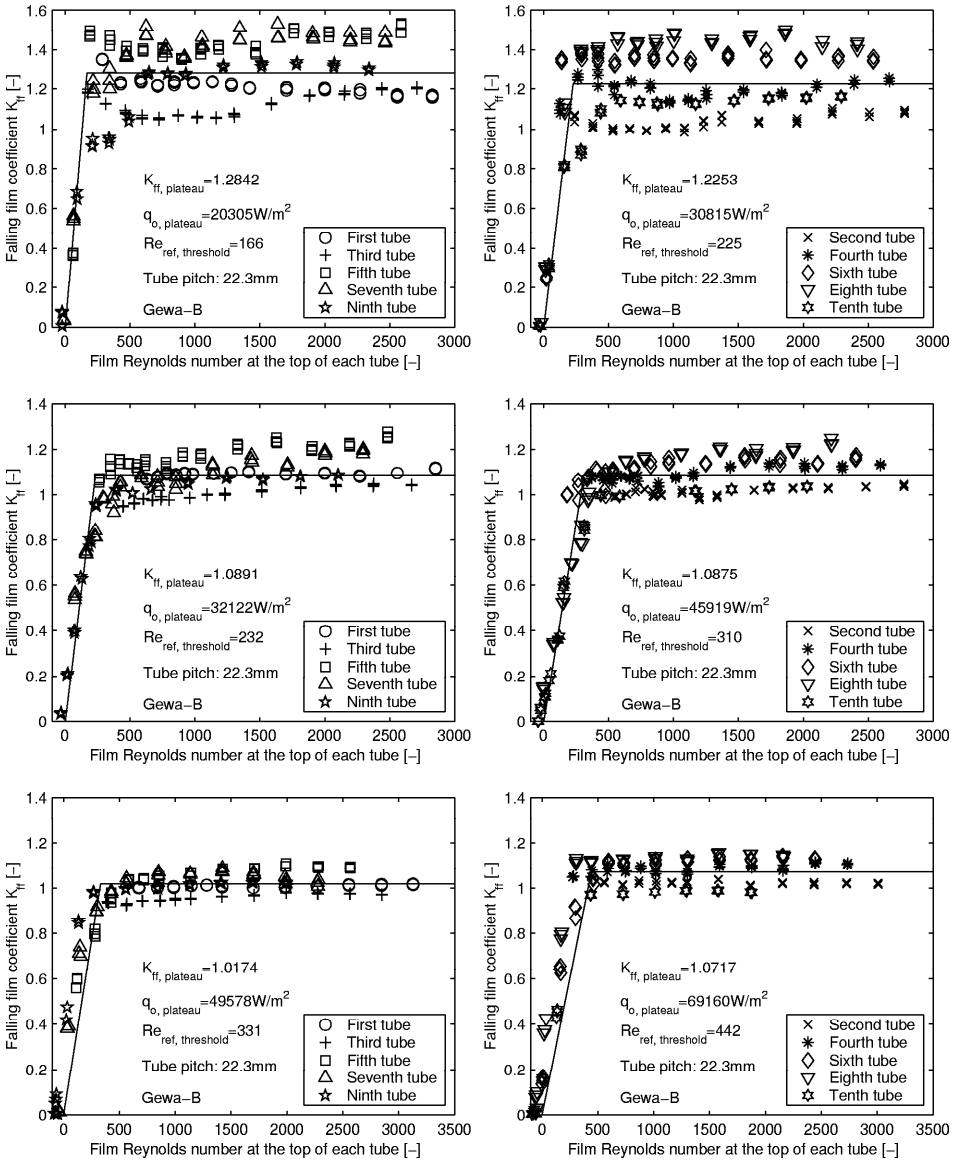

Figure A.7: Falling film heat transfer coefficient ratio K_{ff}, (measured/boiling) for Gewa-B tube with a tube pitch of $22.3mm$, nominal heat flux of 20, 40 and $60kW/m^2$ in the top, the middle and the bottom plots, respectively.

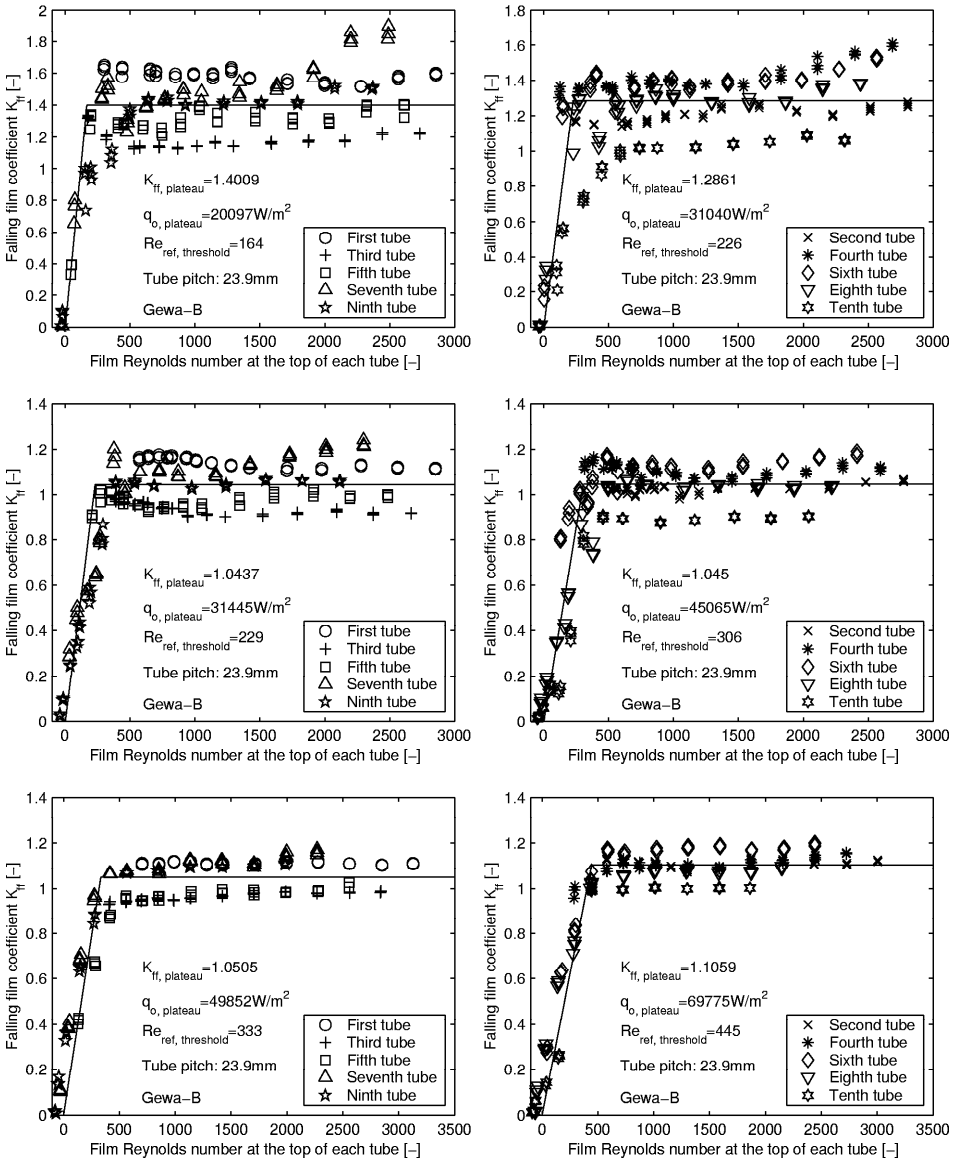

Figure A.8: Falling film heat transfer coefficient ratio K_{ff}, (measured/boiling) for Gewa-B tube with a tube pitch of $23.9mm$, nominal heat flux of 20, 35 and $60kW/m^2$ in the top, the middle and the bottom plots, respectively.

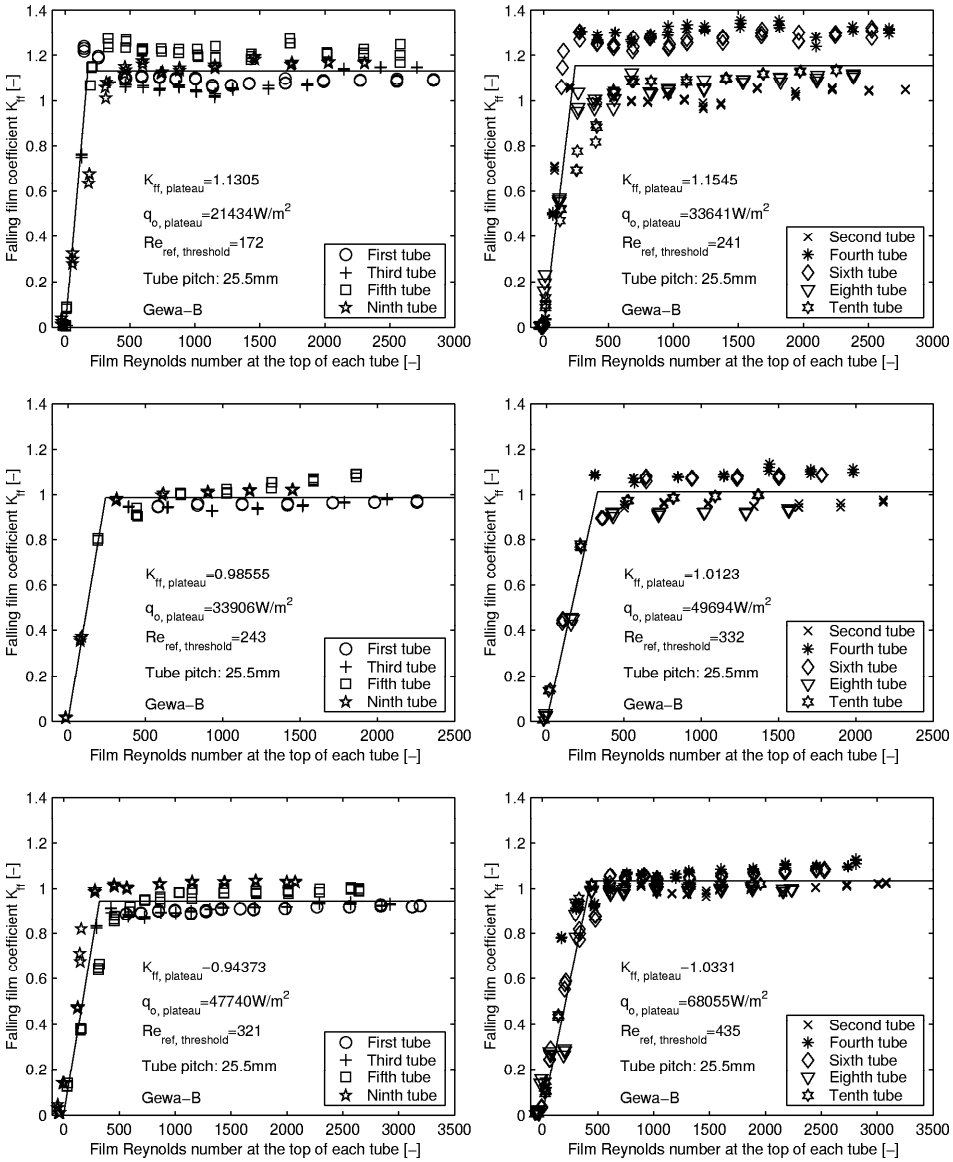

Figure A.9: Falling film heat transfer coefficient ratio K_{ff}, (measured/boiling) for Gewa-B tube with a tube pitch of $25.5mm$, nominal heat flux of 20, 40 and $60kW/m^2$ in the top, the middle and the bottom plots, respectively.

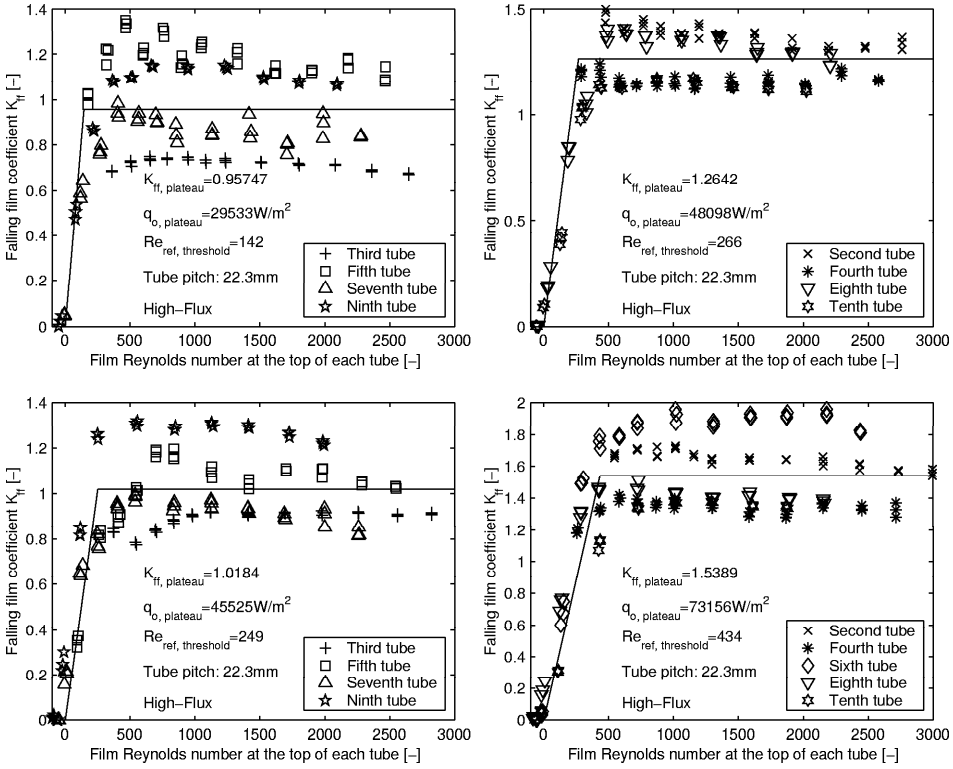

Figure A.10: Falling film heat transfer coefficient ratio K_{ff}, (measured/boiling) for High-Flux tube with a tube pitch of $22.3mm$, nominal heat flux of 40, and $60kW/m^2$ in the top and the bottom plots, respectively.

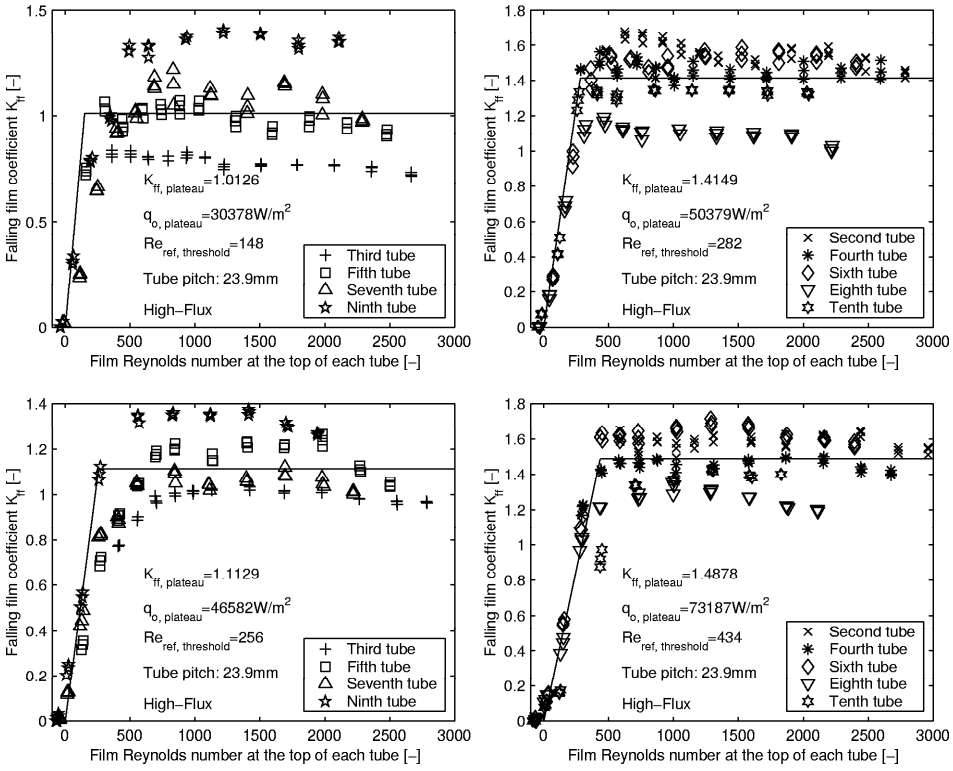

Figure A.11: Falling film heat transfer coefficient ratio K_{ff}, (measured/boiling) for High-Flux tube with a tube pitch of $23.9mm$, nominal heat flux of 40 and $60kW/m^2$ in the top and the bottom plots, respectively.

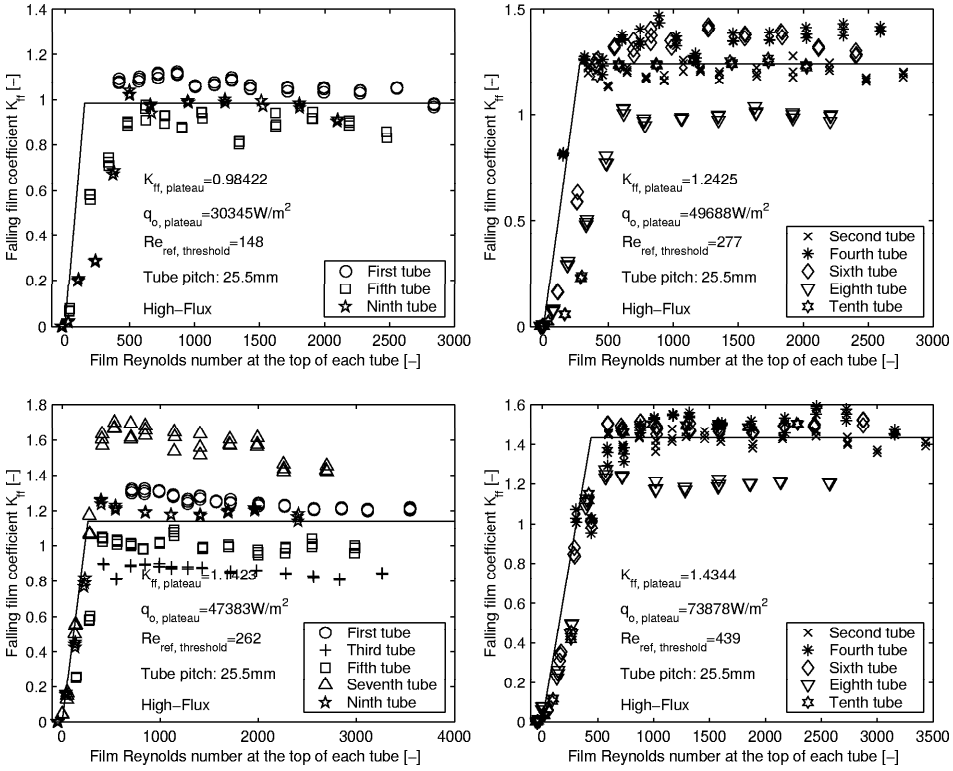

Figure A.12: Falling film heat transfer coefficient ratio K_{ff}, (measured/boiling) for High-Flux tube with a tube pitch of $25.5mm$, nominal heat flux of 40 and $60kW/m^2$ in the top and the bottom plots, respectively.

Appendix B

Wilson plots

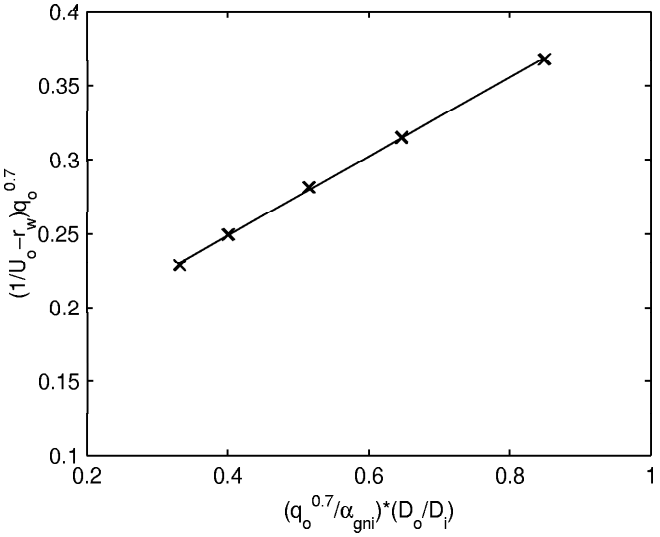

Figure B.1: A modified Wilson plot for the Turbo-BII HP tube, heat flux of $80kW/m^2K$ and water Reynolds numbers from 6000 to 16000, $C_i = 3.83$.

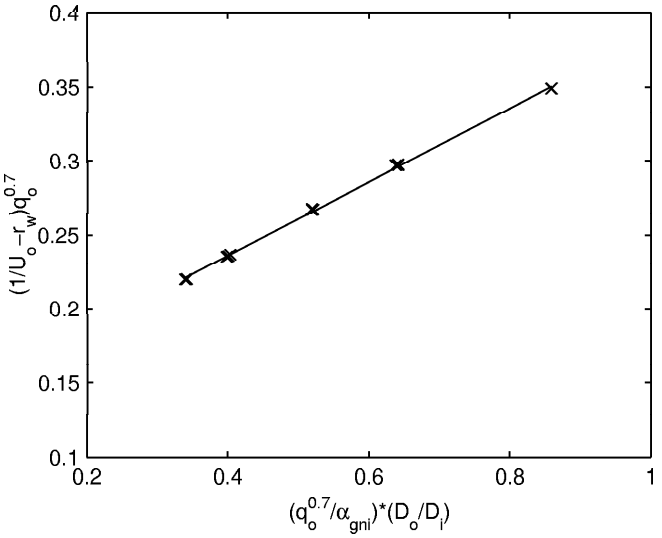

Figure B.2: A modified Wilson plot for the Gewa-B tube, heat flux of $80kW/m^2K$ and water Reynolds numbers from 6000 to 16000, $C_i = 4.16$.

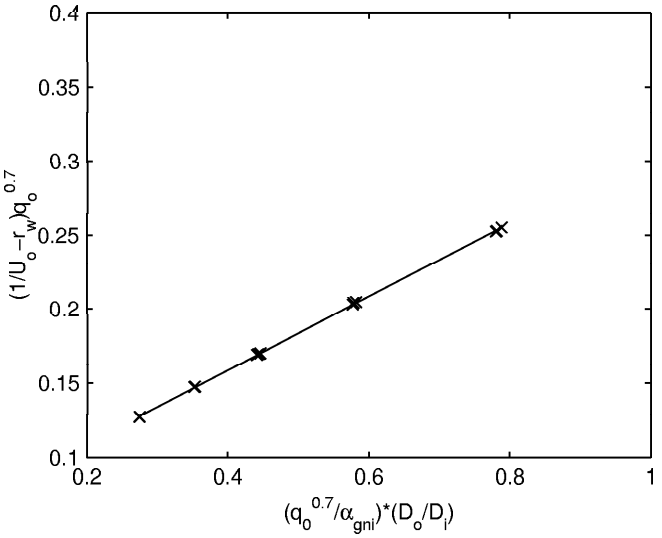

Figure B.3: A modified Wilson plot for the High-Flux tube, heat flux of $60kW/m^2K$ and water Reynolds numbers from 6000 to 18000, $C_i = 4.09$.

List of publications from thesis

- Roques J.-F. and Thome J.R., Flow Patterns and Phenomena for Falling Films on Plain and Enhanced Tube Arrays, *Proc. Third International Conference on Compact Heat Exchangers and Enhancement Technology for the Process Industries*, Davos, Switzerland, 1-6 July, 2001, pp. 391-398.

- Roques J.-F. and Dupont V. and Thome J.R., Falling Film Transitions on Plain and Enhanced Tubes, *J. Heat Transfer*, 2002, vol. 124, pp. 491-499.

- Roques J.-F. and Thome J.R., Falling Film Transitions Between Droplets, Column and Sheet Flow Modes on a Vertical Array of Horizontal 19 fpi and 40 fpi Low Finned Tubes, *Proc. 1st International Conference on Heat Transfer, Fluid Mechanics and Thermodynamics, HEFAT 2002*, 8-10 April, Kruger Park, South Africa, 2002, vol. 1, pp.523-528.

- Roques J.-F. and Thome J.R., Falling Film Transitions between Droplet, Column and Sheet Modes on a Vertical Array of Horizontal 19 fpi and 40 fpi Low Finned Tubes, *Heat Transfer Engineering*, 2003, vol. 24, pp.40-45.

CV

Jean-Franois ROQUES, french citizen, was born on February 3rd 1973 in Port-Harcourt (NIGERIA). He is married to Anne-Cécile.

In 1998, he obtained a "Maîtrise de Mécanique" at the University of Aix-Marseille II in France.

In 1999, he obtained the diploma of Mechanical Engineering at the Swiss Federal Institute of Technology (EPFL) in Lausanne (Switzerland) in Applied Thermodynamics and Turbomachines.

Following his diploma, he worked as an assistant for the Laboratory of Heat and Mass Transfer (LTCM) under the direction of Professor John R. Thome, starting the conception of the Falling Film Test Facility.

His activities in the LTCM also included supervision of student laboratory work, semester and diploma projects.